Numerical techniques for finding the shape of droplets and bubbles

Marginean, A.

Award date:
2013

Master's Thesis

Numerical techniques for finding the shape of droplets and bubbles

Alexandra Mărginean

Eindhoven University of Technology
Department of Mathematics and Computer Science

Eindhoven, November 2013

Supervisor:
dr. ir. B.J. van der Linden

Advisors:
dr.ir. M.J.H. Anthonissen
dr.habil. A.Muntean

Abstract

This thesis is focused on finding the shape of droplets and bubbles, by using different numerical techniques. Another objective is to treat free surface flows that involve surface tension. Our approach in dealing with these free surfaces is to separate the flow simulations from the surface tracking algorithm. Two methods for finding the shape of bubbles have been used: the shooting method and an optimization method. Our interest is to introduce surface tension in SPH (Smoothed Particle Hydrodynamics). We chose the an easy approach, the Tartakovsky's approach, in order to see the effects of surface tension over the fluid flow.

Acknowledgements

Looking back upon this year I realize that this thesis was a big challenge, and through this period I had a lot of support and guidance, so I would like to thank some people who contributed to this.

First of all, I am particularly indebted and grateful to my supervisor dr.ir. B.J. van der Linden for his support and guidance to finish up this work, for all the interesting and stimulating discussions. The subject that he proposed was completely new for me, very challenging and totally different from what I've done before. I have learned a lot from him and I appreciate his patience and encouragement during this period.

I am especially grateful to Iason Zisis for all his support and for all discussions from SPH up to everyday life problems, and most of it for being a friend. Also, I want to thank to all my friends from CASA department, for making days at University nicer.

I am thankful to dr.ir. M.J.H. Anthonissen and dr.habil. A.Muntean for reading my thesis and being part of the committee.

I want to thank to all the people that gave me the opportunity to make this final project for a double-degree master.

Finally, I would like to thank my parents and Daniel, for their unconditional love and continuously support, encourage and motivation, and to all my friends from Romania and Netherlands.

Alexandra Mărginean

Contents

1 Introduction

Why can some insects walk on the water? Why are soap bubbles round? Why does the water climb up a thin tube? To answer this we have to introduce the concept of *surface tension*. Surface tension is most apparent on the interface between a liquid and a gas, but it exists on any interface between two different media or phases. Originating from an energy imbalance on the molecular level, the surface tension is apparent as a tensile force on the surface. This tensile force depends linearly on the local curvature and a material property, the surface tension coefficient. The dependence on the local curvature means that surface tension is most important on small length scales.

The surface tension is thus something that is apparent as a tension on an surface embedded in a higher dimensional space. This makes its treatment in numerical simulations quite difficult. Most numerical approaches would discretize space, dealing with an interface with thermodynamically consistent properties in the middle of it; this requires a lot of implementation detail.

Industrial advances in semi-conductor and related industries make length scales in production processes evermore smaller. Since free surface flows, droplets, and bubbles appear in many stages of production, a reduction in length scales means that proper treatment of surface tension becomes more and more important.

1.1 Goal

In this thesis, we aim to make an overview of a wide range of available analytical and numerical techniques for the treatment of free surfaces that experience surface tension. Our specific interest is in finding a coherent treatment of free surfaces in Smoothed Particle Hydrodynamics (SPH), a meshless method, so we can later include droplet forming in the debris cloud of hyper-velocity impacts.

1.2 Outline

We start in Chapter 2 by defining surface tension and exploring the underlying physics with some sample problems. In Chapter 3, we start to look at numerical techniques to find the shape of droplets if we know the pressure inside and outside the droplet, for example from flow computations. Chapter 4 is devoted to Smoothed Particle Hydrodynamics, a meshless method. We add in Chapter 5 our conclusions.

2 Surface tension

2.1 Background

The interface between two materials that are in contact with one another is called a surface. The force between these two materials which keeps this surface in shape is called *surface tension*. It depends on the attractive forces between the particles within the given liquid and also on the gas, vacuum, solid, or liquid in contact with it. Attraction forces between particles of the same type are represented in Figure 2.1.1. Two cases are presented.

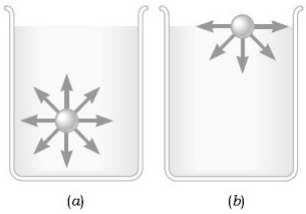

Figure 2.1.1: (a) A molecule within the liquid (b) A molecule at the surface [11]

In the first container a molecule is represented within the bulk liquid. This molecule has neighboring molecules on all sides. The surrounding molecules attract the central molecule equally in all directions, which leads to a zero net force. Contrary, the second container has a molecule on the surface. Because this molecule does not have other liquid molecules above the surface, on this molecule a net force is acting, pulling the molecule in the interior direction. This attractive force makes the liquid surface to contract. This contraction stops when the surface area is minimum, as repulsive collisional forces act as well. Without external forces, the liquid gets a rounded form, which is the minimal surface area. In 3D the minimal surface area is a sphere.

The surface tension, notated by the Greek letter gamma γ or sigma σ, is a property of the two materials.

The phenomenon called surface tension can be defined as the magnitude F of the force exerted parallel with the surface of the liquid per unit length over which it acts. It can be formulated as

$$\gamma = \frac{F}{L}, \tag{2.1.1}$$

where γ is the surface tension, F is the force (N) and L is the unit length (m).

Surface tension leads to a pressure difference across the surface, according to Young-Laplace law [18]:

$$\Delta p = \gamma \left(\frac{1}{R_1} + \frac{1}{R_2} \right), \tag{2.1.2}$$

where R_1 and R_2 are the principal radii of curvature, Δp is the pressure difference and γ the surface tension.

In the case of a sphere with $R_1 = R_2 = R$, (2.1.2) becomes

$$\Delta p = \frac{2\gamma}{R}.$$

An important constant in fluid mechanics is the capillary length (L_c) which is a scale for an interface between two fluids. The capillary constant is defined in the book of Lautrup [18] as

$$L_c = \sqrt{\frac{\gamma}{\rho g}}. \tag{2.1.3}$$

The measurements in SI units for surface tension is N/m (Newton per meter), considering the force per unit length. Another equivalent is J/m^2 for surface energy, which is energy per unit area.

- $1\,N/m = 1\,J/m^2$.

Liquid	**Temperature**	**Surface tension** N/m	Density kg/m^3
Acetone	20°C	0.023	791.00
Glycerol	20°C	0.063	1.261
Mercury	20°C	0.476	13.546
Water	20°C	0.073	998.2071
Water	100°C	0.059	958.4

Table 2.1.1: Values of surface tension for different materials at specific temperatures, against air.

In nature, water, at 20°C, has a high surface tension. A few examples of surface tension values, for different materials, can be seen in Table 2.1.1. If the surface tension is high, like in the case of mercury, the attractive force of the particle is higher than other liquids with lower surface tension.

Considering the surface tension and density from Table 2.1.1, then the L_c in (2.1.3) gives the typical length scale of the diameter.

Surface tension is temperature dependent. The surface tension of water in contact with air decreases significantly with temperature as shown in the graph represented

in Figure 2.1.2. More values of surface tension of water as function of temperature are mentioned in [33].

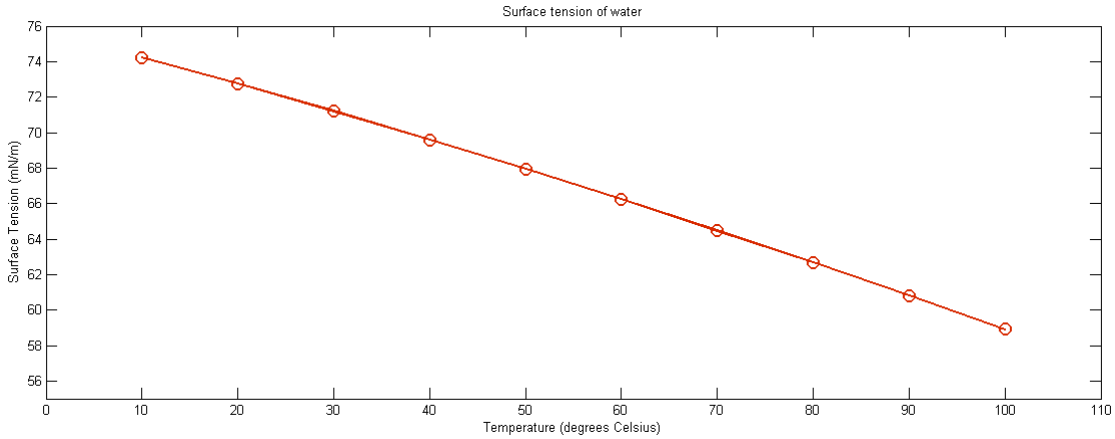

Figure 2.1.2: The surface tension of water decreases significantly with temperature. Values are taken from [33]

Another way to alter the surface tension is by using surfactants, which prefer to stay in the surface, attracting the surface water molecules in competition to the bulk water hydrogen bonding and so reducing the net forces away from the surface.

A few examples where surface tension is an important factor are described further in this section and in Section 2.2.

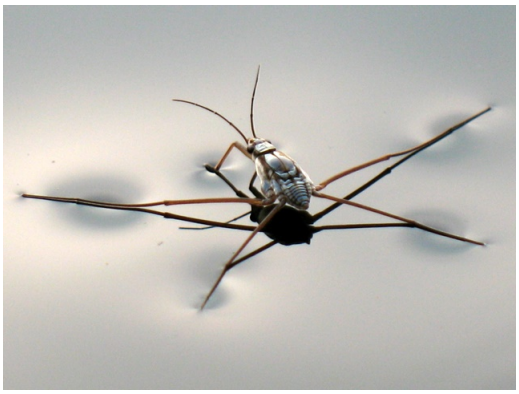

Figure 2.1.3: Water strider; source [24]

A common example is given by the small insects that walk on water (eg. water strider, see Figure 2.1.3). This is possible because the weight of the insect is supported by the high surface tension of the water.

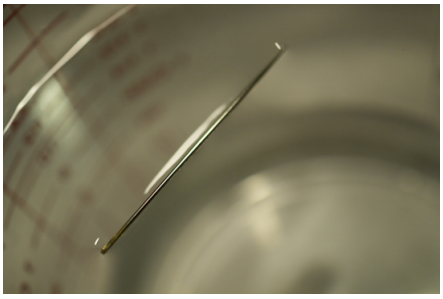

Figure 2.1.4: Needle floating on top of water(credit: Cory Zanker)

A nice example and easy to do as an experiment at home is to make a needle (or a paper clip, see Figure 2.1.4) float. If you carefully place one of these objects onto the surface of water, it can float, even though the object is several times more dense than the water. If you want to sink the needle, just agitate a bit the water so that the surface tension breaks.

Figure 2.1.5 is a cross section of a needle floating on the surface of water. The force of the weight of the needle is balanced by the surface tension. Thus, the mass of the needle is supported by the surface of the water. As we can see from the figure, the forces of surface tension are symmetrical.

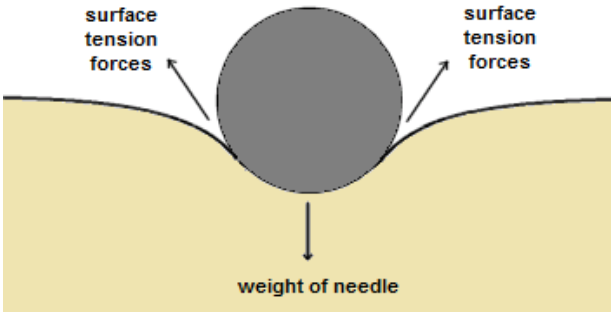

Figure 2.1.5: Forces enabling a needle to float on water

Some examples from our everyday life are: washing with hot water lowers the surface tension and the clothes gets wetter, using soap and detergents also lowers the surface tension, because it lowers the force of attraction between particles.

Droplets are another result of surface tension. Water from a tap, does not flow in a continuous stream, but rather in a series of drops. The shape of drops is caused by the surface tension of the water. The shape is not completely spherical because of the force of gravity pulling down on it. In the absence of gravity, the drop would minimize the surface area in order to minimize tension, which would result in a perfectly spherical

shape. Also for stationary droplets, the surface tension tries to minimize its surface by making it as spherical as possible.

In the paper of Grubelnik and Marhl [10], the process of drop formation of a falling liquid stream is described. It is presented how surface tension influence the drop formation. A falling stream is getting narrowed as it falls because of gravity, then swells are formed until the diameter of the stream goes to zero and drops are formed. Representative photographs are shown in their paper, with these undulations, as in Figure 2.1.6, which we cannot observe, because the amplitude is small. For a better understanding they discuss also about the pressure in the stream, which is larger where the stream has a smaller radius.

Figure 2.1.6: Perturbations of the water stream [10]

Beard, Bringi and Thurai [4] presented in their paper a study case of the raindrop shapes, where they show that the shape of a very small raindrop is spherical and for bigger raindrops the shape is more like a hamburger. Also, Brian Lim [21] changed the popular image of a raindrop, the teardrop, with his study. He plotted the shape of raindrops at different diameters. Examining his results in Figure 2.1.7, we state that raindrop shape is either spherical or more like a hamburger, but not even close to a teardrop shape.

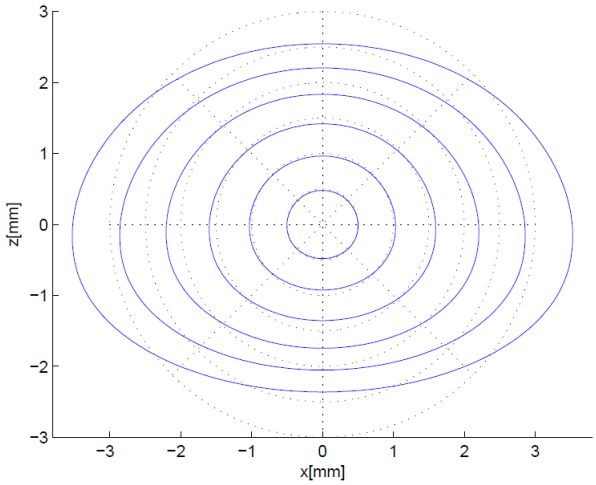

Figure 2.1.7: Shape of rain droplet computed by Brian Lim [21], for d =1,2,3,4,5 and 6 mm with the origin at center of volume

The problem of droplets will be discussed in more details in the next chapter.

2.2 Examples of surface tension

In order to understand the concept of surface tension, we look at three different examples where the surface tension is an important property: stationary droplets, water coming from a tap and rain drops.

2.2.1 Stationary droplet

A droplet of water placed on a solid surface is called a stationary water droplet. These droplets have different shapes and this is a consequence of surface tension, the contact angle that the droplet makes, gravity and the dimension of the water droplet.

Surface tension is a property of the interface between two materials. In the case of a stationary droplet, there are three different interfaces upon which surface tension act: solid-air, solid-liquid and liquid-air (see Figure 2.2.1).

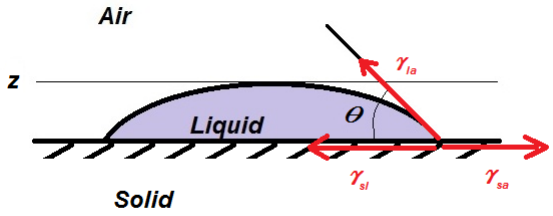

Figure 2.2.1: Drop sitting on a horizontal solid surface with contact angle θ and center height z

The angle measured between the tangent to the surface and the solid surface, is the contact angle (θ angle in Figure 2.2.1).

The contact angle indicates the case of *wettability*: a big contact angle is associated with a poor wetting surface, mostly non-wet surface, in contrast with a small contact angle which represents a surface mostly wet. If the angle is zero, the surface is complete wet, see Figure 2.2.2.

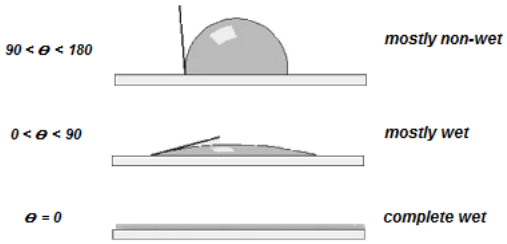

Figure 2.2.2: Drops sitting on a horizontal solid surface with different contact angles

As we mentioned, gravity is another factor that contributes to the flattened droplets. The influence of the gravity depends on the capillary length (L_c, see equation (2.1.3)). Thus, if the L_c is small, we can neglect gravity, but for a bigger L_c gravity will act over the droplet.

To see how all these factors influence the shape of droplets, we consider three water droplets, having different diameters: 1 mm, 5 mm and 2 cm and the contact angle to be an acute angle of $\theta = 45^o$.

The capillary length for the interface air-water at 25 °C is 2.7 mm [18].

The book by Lautrup [18] presents two formulations to approximate the central height of the droplet. Since

$$z \approx R\frac{1-\cos\theta}{\sin\theta} \quad \text{for} \quad R \ll L_c, \tag{2.2.1}$$

we get

$$z \approx 2L_c \sin\frac{\theta}{2} \quad \text{for } R \gg L_c, \tag{2.2.2}$$

where z is the central height of the droplet, R is the radius of the droplet, L_c is the capillary length and θ is the contact angle.

Case 1 : To estimate the height of the droplet with the radius 0.5 mm, which is much smaller than water's capillary length, we will use equation (2.2.1), which leads to

$$z \approx R\frac{1-\cos\theta}{\sin\theta} = 0.207\,\text{mm}. \tag{2.2.3}$$

Case 2 : For the second droplet, with the radius 2.5 mm not much smaller than the capillary length, we use (2.2.1) to approximate the central height

$$z \approx R\frac{1-\cos\theta}{\sin\theta} = 1.035\,\text{mm}. \tag{2.2.4}$$

In these two cases droplets have spherical shape, because we neglect gravity and their radii are much smaller than the capillary length.

Case 3: For the third case, the radius is 1 cm, which means that $R_3 \gg L_c$, so we will use a different formula, equation (2.2.2), where gravity will influence the shape of the water droplet

$$z \approx 2L_c \sin\frac{\theta}{2} = 0.76L_c \approx 2.06\,\text{mm}. \tag{2.2.5}$$

Gravity flattens larger drops. No matter how big the radius will be, the height will be approximately 2 mm for contact angle of $\theta = 45^o$.

The shape of a stationary water droplet has to satisfy the Young-Laplace equation, which describes the capillary pressure difference between two fluids separated by an interface

$$\gamma(\frac{1}{R_1} + \frac{1}{R_2}) = \Delta p, \tag{2.2.6}$$

where γ is the surface tension, R_1 and R_2 are the radii of curvature and $\Delta p = p_i - p_e$ is the pressure difference across the interface.

The curvature is evaluated using a tangent angle coordinate system. We consider the equations of the tangent angle derived by Brian Lim [21] and by Beard and Chuang [3], with the variables s arc length and θ angle between the tangent at the surface and the horizontal line:

$$\frac{dx}{ds} = \cos(\theta),$$

$$\frac{dz}{ds} = \sin(\theta).$$

As Lim demonstrated in [21], after assuming the external pressure to be zero and internal pressure $p_i = \frac{2\gamma}{R_0} + \Delta\rho g z$, equation (2.2.6) can be written as

$$\gamma(\frac{1}{R_1} + \frac{1}{R_2}) = \frac{2\gamma}{R_0} + \Delta\rho g z. \tag{2.2.7}$$

Using the tangent coordinate system, as Liu shown in [21], Appendix A2, we can write (2.2.7) as

$$\gamma(\frac{d\theta}{ds} + \frac{sin\theta}{x}) = \frac{2\gamma}{R_0} + \Delta\rho g z. \tag{2.2.8}$$

As Rio and Neumann in [27], we will consider two more equations

$$\frac{dV}{ds} = \pi x^2 \sin\theta,$$

$$\frac{dA}{ds} = 2\pi x,$$

where V is the volume and A is the surface area.

The system of ordinary differential equations as function of arc length s, for determining the shape of the stationary water droplet is:

$$\begin{aligned}
\frac{dx}{ds} &= \cos(\theta), \\
\frac{dz}{ds} &= \sin(\theta), \\
\frac{d\theta}{ds} &= \frac{2}{R} + \frac{\Delta\rho g z}{\gamma} - \frac{\sin\theta}{x}, \\
\frac{dV}{ds} &= \pi x^2 \sin\theta, \\
\frac{dA}{ds} &= 2\pi x,
\end{aligned} \tag{2.2.9}$$

with the conditions:

$$x(0) = z(0) = \theta(0) = V(0) = A(0) = 0.$$

Equation (2.2.9) was derived by rearranging (2.2.8).

Assume γ = 0.072 N/m, a contact angle of θ =45 °C and three different radii 0.05 mm, 0.25 mm, 1 cm for water droplets. The liquid is considered to be water while the other fluid is air. The system was solved in Mathematica, with the function NDSolve

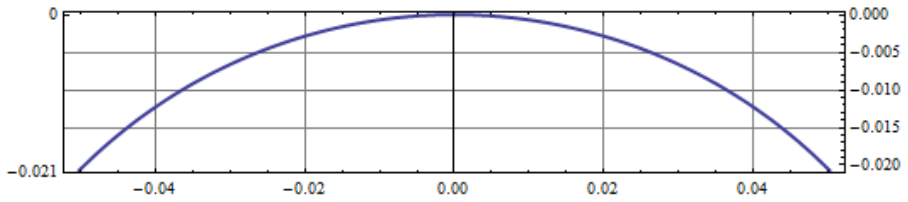

Figure 2.2.3: Drop shape for radius 0.05 cm, where we have the value for height = 0.020 67 cm

The shape of the droplet with the radius 0.05 cm is spherical, as we expected, because the droplet is minimizing its contact surface and here gravity is negligible. In Figure 2.2.3 we can see that the central height is 0.2067 mm. This result is approximately the same with what we obtain in (2.2.3).

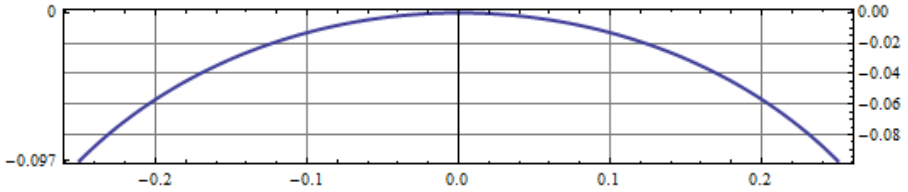

Figure 2.2.4: Drop shape for radius 0.25 cm, where we have the value for height = 0.0971 cm

In Figure 2.2.4 the radius of droplet is 0.25 cm and the central height obtained is 0.971 mm. Again the result is approximately the same with what we calculated before in (2.2.4). The shape is spherical, because the effect of gravity over droplet is very low.

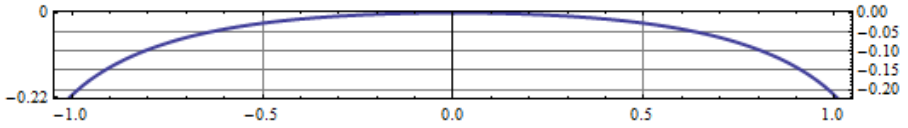

Figure 2.2.5: Drop shape for radius 1 cm, where we have the value for height = 0.220 cm

In Figure 2.2.5 the radius of droplet is 1 cm and the central height is 2.20 mm. The result is appropriate to the one from (2.2.5). In this situation the shape is not spherical anymore. It is flattened compared with the previous two. If we increase the radius of the drop, the height will not be bigger, because around 2 mm is the maximum.

2.2.2 Water from tap

Surface tension is an important factor in the spontaneous breaking of the jet of water coming from a pipe. A water jet that is falling vertically under gravity, at the beginning it has constant radius, and after a critical point, where it changes its shape, it gets into a flux of droplets. This phenomenon occurs as a result of surface tension.

In order to explain how surface tension influences the water jet, we will consider the following experiment: a glass of 0.2 l fills with water in 2 min, with the measurements from Table 2.2.1 (measurements come from a picture taken to a water jet). In the measurements the length of the laminar water jet is 0.10 m, after which we observed it break in droplets.

Quantity	Unit	Value	Meaning
$D_{tap-screen}$	cm	3.3	Size of tap on screen
D_{tap}	m	0.019	Physical diameter of tap
$Scale$	-	0.019/3.3	Screen-reality scale
$D_{jet-screen}$	cm	0.25	Diameter of jet on screen (before perturbations)
D_{jet}	m	0.0014	Physical diameter of jet (before perturbations)

Table 2.2.1: Measurements experiment

The volume flow rate written in terms of volume of fluid V and time t is

$$Q = \frac{V}{\Delta t}. \tag{2.2.10}$$

Replacing it with data from experiment, this yields to

$$Q = \frac{0.2 \times 10^{-3}\,\mathrm{m}^3}{120\,\mathrm{s}} = 1.67 \times 10^{-6}\,\mathrm{m}^3/\mathrm{s}. \tag{2.2.11}$$

Another formula for the volumetric flow is

$$Q = vA,$$

which can be written as

$$Q = v\frac{\pi}{4}D^2, \tag{2.2.12}$$

where D is diameter, v is the velocity field of the water flowing and A is the cross-sectional area.

Forward, we will approximate the length of the jet, from the moment it leaves the pipe, until it presents perturbations, undulations of the water jet, in order to compare it with the measurement from the picture.

The fluid flow through a pipe with diameter D_{tap}, is laminar if the Reynolds number is smaller than 2000. If the Reynolds number is bigger than 3000, the flow is turbulent, and when it is between $2000 \lesssim Re \lesssim 3000$ the flow is unstable. The Reynolds number [29] is

$$Re = \frac{vD\rho}{\mu}, \tag{2.2.13}$$

where v is the velocity of the fluid, ρ is the density of the fluid, and μ is the dynamic viscosity of the fluid.

In free falling under gravity, the velocity of the fluid at distance h from the pipe is :

$$v = \sqrt{v_0^2 + 2gh}, \tag{2.2.14}$$

which is Galilei's formula, where v_0 is the velocity when the water leaves the pipe and g is the gravity.

We know the volume flow rate from (2.2.12), so we can calculate the velocity when the water leaves the tap:

$$v_0 = \frac{4Q}{\pi D_{tap}^2} = 5.89 \times 10^{-3}\,\mathrm{m/s}.$$

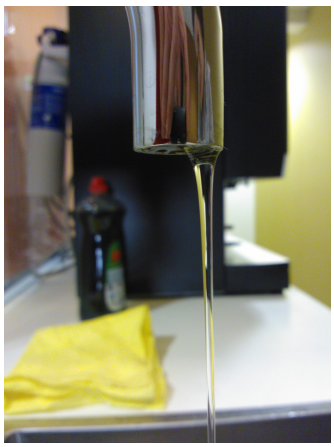

Figure 2.2.6: Our own experiment with an every day realization of surface tension: we photograph running tap water to measure the diameter at different heights and collect the water to measure the average flow rate.

Equation (2.2.12) can be written as a formula for the diameter of the flow with velocity v.

$$D = \sqrt{\frac{4Q}{\pi v}}. \tag{2.2.15}$$

From equation (2.2.13), we have

$$vD = \frac{\mu Re}{\rho}. \tag{2.2.16}$$

Replacing D from equation (2.2.15), in equation (2.2.16), will lead to another formulation for the velocity

$$v\sqrt{\frac{4Q}{\pi v}} = \frac{\mu Re}{\rho} \implies \sqrt{\frac{4Qv}{\pi}} = \frac{\mu Re}{\rho} \implies \frac{4Qv}{\pi} = \frac{\mu^2 Re^2}{\rho^2},$$

$$v = \frac{\mu^2 Re^2 \pi}{4Q\rho^2}. \tag{2.2.17}$$

Putting together equation (2.2.14) and equation (2.2.17), we will get the formula for the length of the laminar water jet, starting from the tap:

$$\sqrt{v_0^2 + 2gh} = \frac{\mu^2 Re^2 \pi}{4Q\rho^2},$$

$$v_0^2 + 2gh = \frac{\mu^4 Re^4 \pi^2}{16Q^2\rho^4},$$

$$h = \frac{1}{2g}\left(\frac{\mu^4 Re^4 \pi^2}{16Q^2\rho^4} - v_0^2\right). \tag{2.2.18}$$

All variables are known, so we replace gravity with $g = 9.8\,\mathrm{m/s^2}$, viscosity with $\mu = 8.9 \times 10^{-4}\,\mathrm{Pa\,s}$, Reynolds number with $Re = 2000$, volume flow rate with $Q = 1.67 \times 10^{-6}\,\mathrm{m^3/s}$ and density with $\rho = 10^3\,\mathrm{Kg/m^3}$, we will get that the laminar water jet has the length $h = 0.11\,\mathrm{m}$. This result is approximately the same with the measurement from the Figure 2.2.6.

Further we analyze more the water jet. What we can notice in Figure 2.1.6 are the perturbations in the flow, which cause waves of very small amplitude, that sometimes we cannot observe. The perturbations became bigger in time and cause formation of drops at the bottom. This process is due to the surface tension, because the water tends to reduce its surface area.

From [18], we know that the jet is chopped into pieces of size $\lambda = \pi\sqrt{2}D_{jet}$, which represents the wavelength. So, for our experiment the wavelength has a diameter of $\lambda = 0.006\mathrm{m}$. Then the radius of the wavelength is $r \approx 0.003\mathrm{m}$. In this case, the approximately volume of a droplet that is formed at the bottom is $V_{droplet} \approx 0.1127 \times 10^{-6}\mathrm{m}^3$.

2.2.3 Rain droplet

The shape of the falling rain droplets is a subject treated by many researchers, in the form of experimental and theoretical investigations. The understanding of the rain drop shape started with the experimental work of P. Lenard (1904) [20], who observed that the surface tension is a factor in drop deformation. High-speed photographs reveal the shape of different diameters rain droplets, as in [4], Figure 2.2.7.

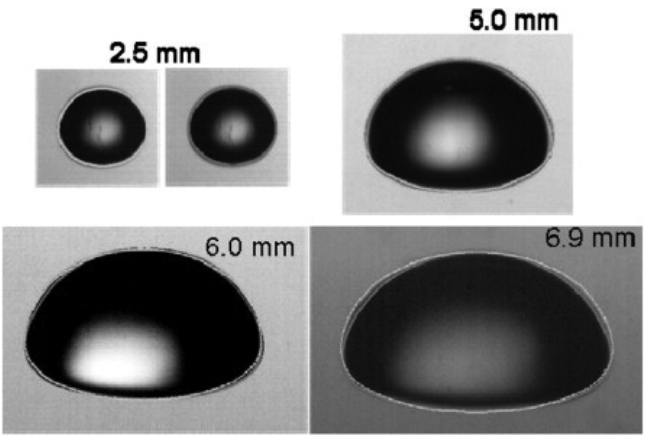

Figure 2.2.7: Rain drop shape [4]

Since initial particles have different sizes and rates of coalescence, rain drops have different sizes, . They have the ranging sizes of the diameter from 1 to 5 millimeters. Rarely can they reach 9 mm, but above this they tend to break up.

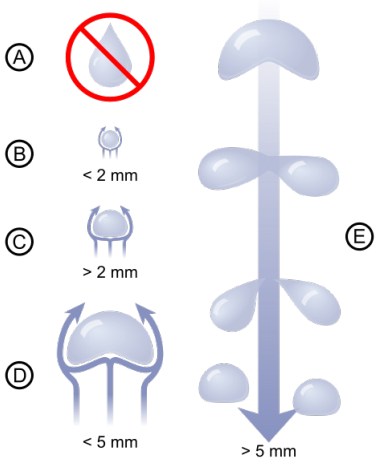

Figure 2.2.8: Shape of rain drops[figure source P. Broks]

The shape of droplets is spherical. Increasing the size of the rain drop, the shape will change and the drop will become flatter. This is contrary to popular image of the rain droplet being tear drop. The rain drop larger than 5 mm, usually splits into two separate drops (see Figure 2.2.8, E).

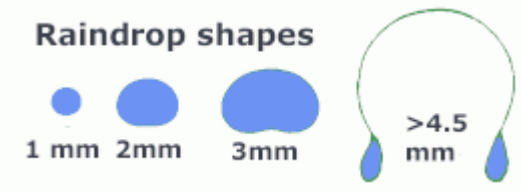

Figure 2.2.9: Shape of rain drops[source figure: USGS science for a changing world]

Small raindrops with radius less than 1 mm are spherical due to the surface tension of the water. This surface tension is making the molecules stick together, as it acts like a “skin" of the water. As they became larger they tend to look like a hamburger and when they increase their size, the shape looks more like a parachute (see Figure 2.2.9); after that they break. The hamburger shape is given by the increasing of the fall velocity and the pressure on the bottom. At the top small air circulation disturbances creates less air pressure, such that surface tension keeps the round shape. When the size of the drop goes over 4.5 mm then a depression is developing, forming the shape of a parachute. When the rain drop splits it is because of the lower surface tension and air the flows around the drop.

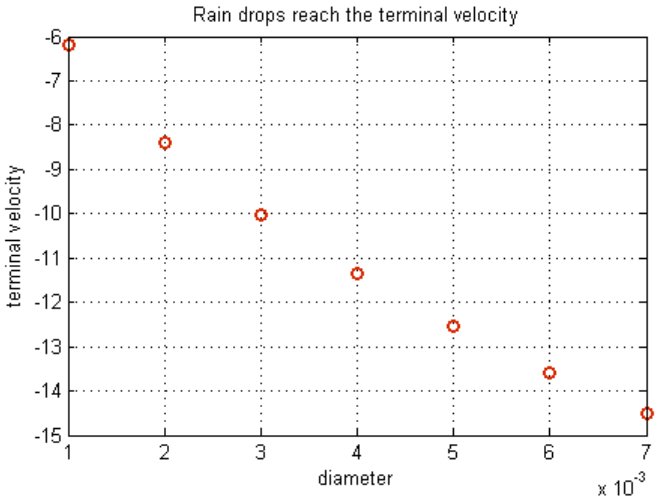

Figure 2.2.10: Rain drops reach the terminal velocity

There are some factors that can affect the size of the rain drop. The velocity of the falling droplet is directly proportional to its diameter. Thus, larger droplets falls with

bigger velocity, see Figure 2.2.10. Falling droplets have to deal with air resistance or frictional force. The size of the droplet bottom or the surface area resisting the fall, influence the magnitude of the force. Frictional drag increases as the droplets accelerates, or speeds up.

As a rain drop falls, it has constant velocity and no acceleration. This is called terminal velocity, when the frictional and gravitational forces balance and the droplet falls at a constant speed. This again depends on size; smaller droplets reach faster the terminal velocity than larger droplets, see Figure 2.2.10. Another factor that influence the size of the droplet is the fact that the falling droplet eats up more droplets, increasing its volume.

When the droplet is falling, the acceleration takes place only for a few seconds and then it falls with terminal velocity. Figure 2.2.11 shows that for a droplet with a diameter of 1 mm the acceleration is about 1 s, compared with a bigger droplet with a diameter of 7 mm, which accelerates around 3 s and only then reaches the terminal velocity.

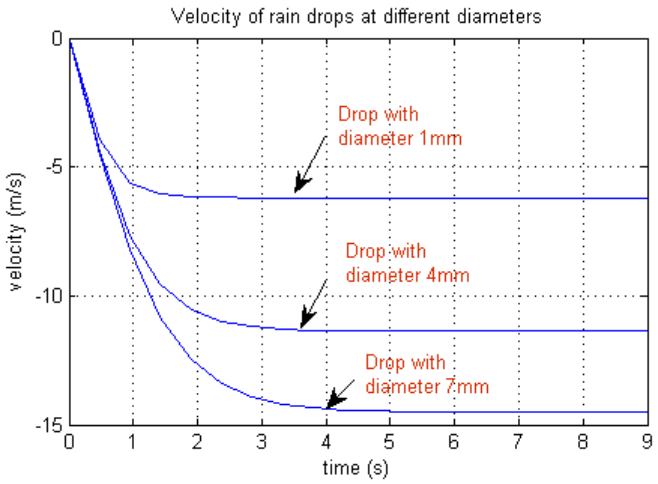

Figure 2.2.11: Velocity of rain drops at different diameters

In the case of smaller drops, they are not falling, they are remaining in clouds.

In fluid mechanics, the Reynolds number (Re) is mentioned many times, because it gives a measure of the ratio of inertial forces to viscous forces. It is a dimensionless number which characterize the flow of a fluid, in different regimes, such as laminar or turbulent flow. The flow is turbulent when the inertial forces dominate over the viscous forces, which means that we have a fluid that flows fast and a large Re. The laminar flow is encounter when the viscous forces are dominant, which means that we have a fluid that flows slowly and a low Re.

The Reynolds number is defined as

$$Re = \frac{\rho v L}{\mu},$$

where v is the velocity of the drop, ρ is the density of the fluid (for water, at 20 °C is 0.998 21 g/cm^3), L is the traveled length of the fluid, μ is the viscosity of the fluid. So, the Re is dependent on the velocity of the drop.

For a small Re ($Re \ll 1$) the drag coefficient[1] is inverse proportional to the Re. The drag coefficient continues to decrease with the increasing of Re, until it gets constant, at bigger Re ($10^3 < Re < 2 \cdot 10^5$).

In order to obtain a formulation for the terminal velocity we will use Newton's Second Law $F = ma$, where F is the sum of all forces, m is the mass of the object and a is its acceleration. This law implies that the acceleration of the drop is directly proportional to the net force acting on it, and inversely proportional to its mass. By definition, terminal velocity has no acceleration, which means that the net force acting on drop is zero. Thus, a drop that is falling through the air will hit the terminal velocity when the drag force is equal to its weight

$$F = mg - \frac{1}{2} C_d \rho A v^2 = 0,$$

where

$$F_g = mg, \tag{2.2.19}$$

is the gravitational force and

$$F_d = \frac{1}{2} C_d \rho A v^2, \tag{2.2.20}$$

is the drag force.

So, the formula for velocity can be written as

$$v = \sqrt{\frac{2mg}{\rho A C_d}},$$

where v is the velocity, m is the mass, g is the standard gravity, C_d is the total drag coefficient, ρ is the air density, and A is the cross sectional area; the last three terms are constants.

Sometimes we need to calculate the velocity depending on time. In order to get this formulation, we will start again from Newton's Second Law, but this time in terms of the rate of change of velocity over time. For constant mass it writes:

$$F = m\frac{dv}{dt}. \tag{2.2.21}$$

[1] Drag coefficient is a dimensionless quantity, which quantifies the drag of an object in a fluid medium, like water or air. It is defined as $C_d = \frac{2F_d}{\rho v^2 A}$

Knowing that $F = F_d - F_g$ and replacing gravitational force (2.2.19) and the drag force (2.2.20), equation (2.2.21) can be written as

$$m\frac{dv}{dt} = \frac{1}{2}C_d\rho A v^2 - mg.$$

This leads to a formulation for the derivative of velocity over time, with C_d, ρ and A constants

$$\frac{dv}{dt} = \frac{C_d\rho A v^2}{2m} - g.$$

After integrating, we find the formula for the velocity of a rain drop, depending on time

$$v(t) = \frac{\sqrt{\frac{mg}{\frac{1}{2}C_d\rho A}}\left(e^{-2t\sqrt{\frac{g\frac{1}{2}C_d\rho A}{m}}} - 1\right)}{1 + e^{-2t\sqrt{\frac{g\frac{1}{2}C_d\rho A}{m}}}}.$$

The results from Figure 2.2.11, are obtain using this formula. As we can see on the graph, we can conclude that smaller droplets reach terminal velocity faster than bigger droplets.

Further we want to compute the pressure distribution of a potential flow around a droplet, to see if the pressure is the same around the droplet. In order to do that we make the following assumptions: the droplet is spherical, it is not deformable, incompressible and isothermal. Another assumption is about the medium in which the droplet is considered, also isothermal, we have no viscosity, which means zero friction, such that we have an ideal medium.

The surface pressure distribution is calculated from Bernoulli's equation at points a and b (for a flow coming from left to right, a is left to the droplet and b is right to the droplet), where ρ_a and ρ_b are densities, v_a and v_b are velocities, p_a and p_b are pressures at those points. Summing the static pressure and the dynamic pressure leads to

$$\frac{1}{2}\rho_a v_a^2 + p_a = \frac{1}{2}\rho_b v_b^2 + p_b.$$

We can rewrite the previous formulation in terms of pressure difference, by

$$p_b - p_a = \frac{1}{2}\rho_a v_a^2 - \frac{1}{2}\rho_b v_b^2.$$

We assumed that the fluid is incompressible so we do not have changes in density which means $\rho_a = \rho_b = \rho$.

$$p_b - p_a = \frac{\rho}{2}\left(v_a^2 - v_b^2\right).$$

We denote the free stream velocity and pressure [2] as U_∞ and p_∞. Then we substitute the velocity at point b as a function of b point's radial coordinate $v_b = v_b(\theta) = -2U_\infty \sin\theta$. Finally, we obtain a formulation for the pressure distribution

$$p_b - p_a = \frac{\rho}{2}\left(U_\infty^2 - (-2U_\infty \sin\theta)^2\right),$$

$$p_b = p_\theta = p_a + \frac{\rho}{2}U_\infty^2\left(1 - 4\sin^2\theta\right).$$

Assume that p_a is zero, we get

$$p_\theta = \frac{\rho}{2}U_\infty^2\left(1 - 4\sin^2\theta\right).$$

In order to find the drag force, we will integrate the pressure at the angle θ over all circle

$$D = \int_0^{2\pi} p_\theta d\theta = \int_0^{2\pi} \frac{\rho}{2}U_\infty^2\left(1 - 4\sin^2\theta\right) d\theta.$$

We can write the pressure in terms of pressure coefficient

$$C_p = 1 - \left(\frac{v_b}{U_\infty}\right)^2,$$

so, in our case it is

$$C_p = 1 - 4sin^2\theta. \tag{2.2.22}$$

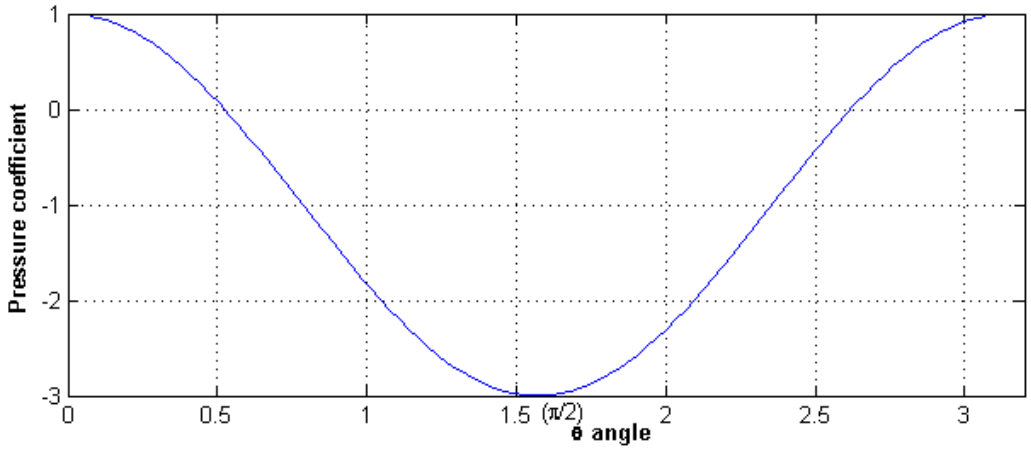

Figure 2.2.12: Pressure coefficient distribution for flow past a sphere

[2] Free-stream velocity and pressure is the velocity and the pressure far away from any object or boundaries in the part of the flow that is not disturbed by any object or boundaries.

Figure 2.2.12 shows the graph of the pressure coefficient as a function of θ. We can consider this as ideal pressure distribution. When the C_p is at zero, it means that the pressure is the same as the free stream pressure, at C_p equal to one means that the pressure is at a stagnation point which is the biggest pressure, and as the C_p goes below zero the pressure decreases.

For a better understanding of the pressure distribution around the droplet we analyze a few COMSOL simulations.

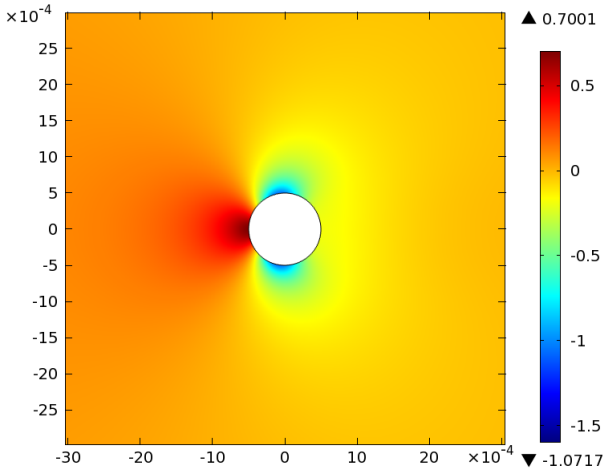

a) velocity = 1 m/s ; radius = 0.5 mm

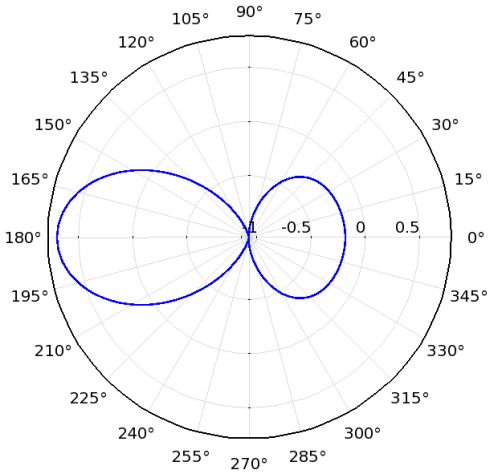

2a) velocity = 1 m/s ; radius = 0.5 mm

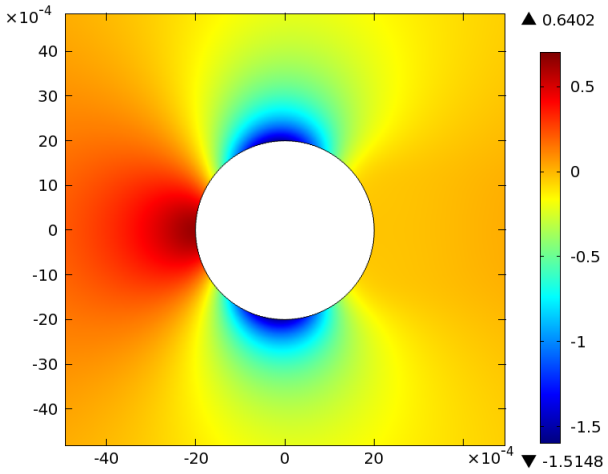

b) velocity = 1 m/s ; radius = 2 mm

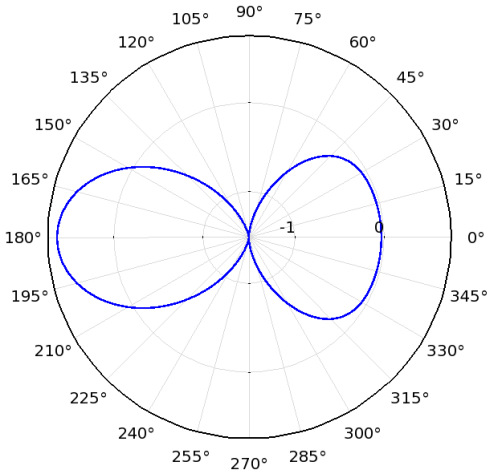

2b) velocity = 1 m/s ; radius = 2 mm

Figure 2.2.13: Pressure distribution around a droplet (1)

We chose to use COMSOL because it is a nice and simple way to couple mechanisms, in order to understand their combined effect. Figure 2.2.13 and 2.2.14 contains two

simulations each, where the velocity of the droplet is 1 m/s or 10 m/s. The radius of the sphere was computed for two values 0.5 mm and 2 mm. The material in which the droplet is placed is air. The air flow is considered to be laminar with the direction of the flow from left to right. In our simulation the flow is symmetrical with respects to the x-axis. Another condition that was taken in consideration is the fact that at the boundary of the circle we have positive velocity relative to the boundary (slip condition).

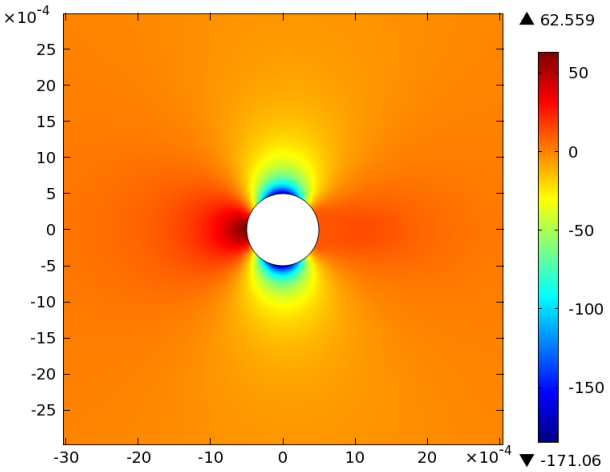

c) velocity = 10 m/s ; radius = 0.5 mm

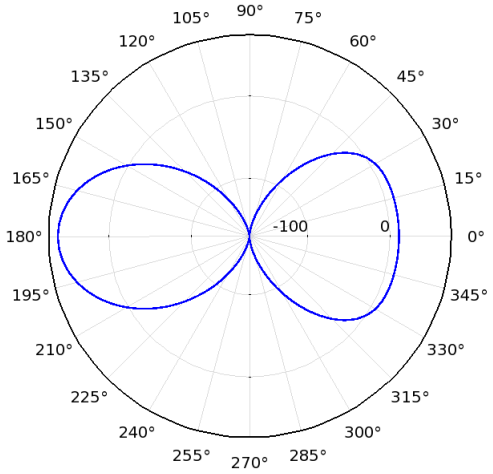

2c) velocity = 10 m/s ; radius = 0.5 mm

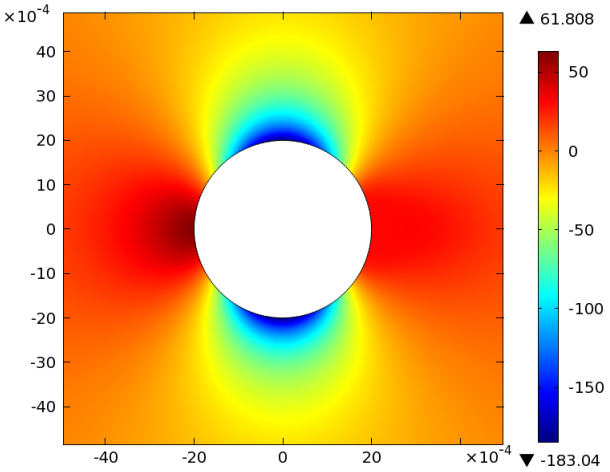

d) velocity = 10 m/s ; radius = 2 mm

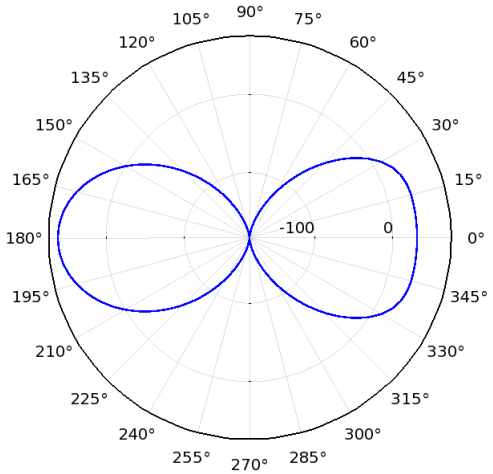

2d) velocity = 10 m/s ; radius = 2 mm

Figure 2.2.14: Pressure distribution around a droplet (2)

Figure 2.2.13 and 2.2.14 represents the pressure distribution over a droplet. First columns are plots of the magnitude of pressure using a color scale. Polar plots with

the theta angle from 0 °C to 360 °C are represented in second columns. In all cases the pressure reaches the highest values when the flow encounters the droplet in the way (the left part of the droplet). Following the theta angle from 180 °C to 90 °C, we see a decreasing in pressure, from the highest value to the lowest. Looking at the first quadrant, and considering the theta angle from 90 °C to 0 °C, we can observe an increase in pressure. Note that the pressure is distributed symmetrical on the x axis but not on the y axis. The pressure is much bigger for theta at 180 °C compared to the one at theta 0 °C.

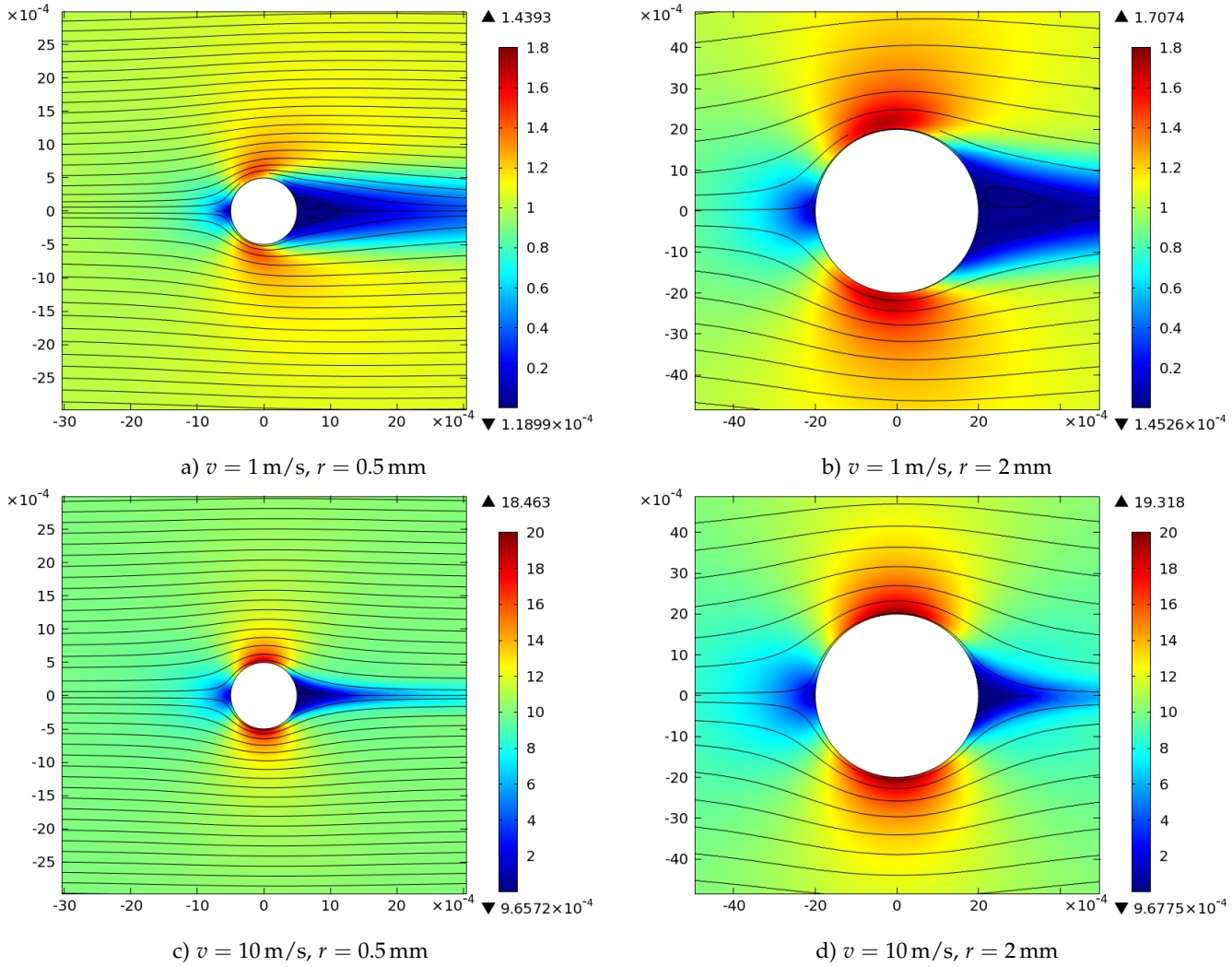

a) $v = 1\,\mathrm{m/s}$, $r = 0.5\,\mathrm{mm}$

b) $v = 1\,\mathrm{m/s}$, $r = 2\,\mathrm{mm}$

c) $v = 10\,\mathrm{m/s}$, $r = 0.5\,\mathrm{mm}$

d) $v = 10\,\mathrm{m/s}$, $r = 2\,\mathrm{mm}$

Figure 2.2.15: Velocity streamlines over droplet, where v[m/s] is the velocity magnitude and r[m/s] the droplet radius

Comparing plots from Figure 2.2.13 where the velocity is the same but the radius is different, we can conclude that the magnitude of the pressure depends on the radius

of the droplet. The lowest pressure over droplet is reached when the radius is bigger and the highest for a droplet with a smaller radius.

The velocity is another influence factor. Taking in consideration 2.2.13 (a) and 2.2.14 (c), where the radius of the droplet is 0.5 mm, the difference is the magnitude of the velocity. Increasing the velocity, the magnitude of the pressure will be also increased. This means that a droplet that is falling with a big velocity will be much flatter, due to the pressure, than droplets falling with smaller velocity.

Moreover, analyzing Figure 2.2.13 with Figure 2.2.15, we can observe how the pressure is getting higher when the flow is slowing down. The velocity of the flow is decreasing until it reaches a speed of zero. It has the minimum value at the point at which the flow hits the droplet. The maximum velocity is reached, where the pressure is very low, which is on top (90 °C) and on bottom of the droplet (270 °C).

Further, we want to obtain the graphical illustrations for the shape of droplets. In the first step, we will consider the curvature to be constant, then we will introduce pressure into curvature, to see how this will influence the shape. Later on, we will introduce pressure data taken from COMSOL simulations (cases presented in Figure 2.2.13 and 2.2.14) into curvature in order to find the shape of droplets and bubbles.

3 Finding bubble shapes from curvature or pressure

One approach to deal with a free surface simulation is to separate the flow simulation from the surface tracking algorithm. This is a common approach in fluid-structure interaction methods, which could be employed to free surface problems. As we have seen previously the local curvature and the pressure jump over an interface are related by the Young-Laplace equation (2.1.2). It gives the coupling between the two problems.

In this chapter we introduce and analyze two different methods to find the shape of bubbles, given the curvature. We also show how this curvature is obtained from flow computations. In the first method, the shooting method, we rewrite the problem as a (non-linear) ordinary differential equation with periodic boundary conditions and look for the numerical solution. In the second method we consider the problem as a curve-fitting problem, or more generically as an optimization problem, since we add an additional constraint to preserve mass/area/volume.

3.1 Shooting method

Curvature is defined in [16, 15], as the amount by which a geometric object deviates from being flat or straight in the case of a line. The curvature of a circle can be defined as the reciprocal of the radius

$$\kappa = \frac{1}{R}. \tag{3.1.1}$$

Thus, a circle with a large radius will have a small curvature and vice-versa.

The curvature of a curve that is given in polar coordinates as $r(\vartheta)$ is defined in [19] as

$$\kappa(\vartheta) = \frac{r^2 + 2(r')^2 - rr''}{(r^2 + (r')^2)^{3/2}}, \tag{3.1.2}$$

where r' and r'' are the first and second derivatives of r, both with respect to ϑ.

Rearranging (3.1.2) we will get a second order non-linear ordinary differential equation (ODE)

$$rr'' - 2(r')^2 + \kappa(\vartheta)(r^2 + (r')^2)^{3/2} = r^2. \tag{3.1.3}$$

Introducing $u = r'$, we can write (3.1.3) as a system of first order ODEs

$$\begin{cases} r' = u \\ u' = r + 2\frac{u^2}{r} - \frac{\kappa(\vartheta)}{r}(r^2+u^2)^{3/2} \end{cases}',$$

where ϑ is from 0 to 2π. This is a boundary value problem (BVP), with boundary conditions $r(0) = r(2\pi)$ and $r'(0) = 0$. We take the derivative of radius to be zero in order to have symmetry over the x-axis.

In order to solve the system we use the shooting method [31]. This is a method used for BVP, which reduces the problem to the solution of an initial value problem (IVP). Thus, our BVP of first order ODE will be reduced to solving the IVP

$$\begin{cases} r' = u \\ u' = r + 2\frac{u^2}{r} - \frac{\kappa(\vartheta)}{r}(r^2+u^2)^{3/2} \end{cases}', \tag{3.1.4}$$

with $r(0) = r_0$ and $u(0) = 0$, being the initial conditions.

To solve the BVP, r_0 has to be determined such that it satisfies the boundary value conditions. We chose to solve a IVP instead of BVP because of the periodicity, which means that we do not know the starting condition.

The shooting method will be based on the secant method [1]. This method is a root-finding algorithm which uses a succession of roots of secant lines in order to give a better approximation to the root of a function.

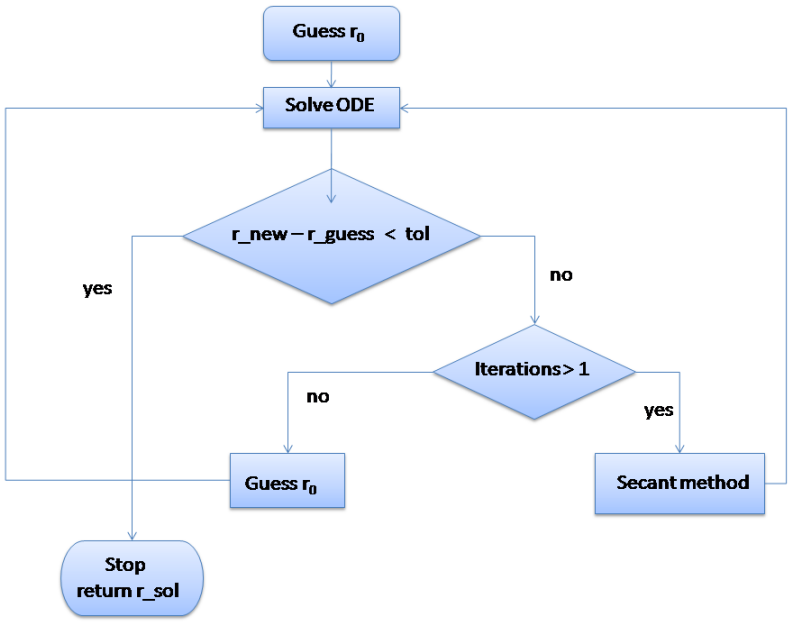

Figure 3.1.1: Flow chart of the algorithm

Using an iterative process based on the secant method, we can estimate a value for r_0, solving (3.1.4). Note that we need two initial choices (guesses) to be able to compute the third and continue the iterations. Thus, for given $r_{0,1}$ and $r_{0,2}$, the secant method computes $r_{0,k}$ for $k > 2$.

The process is described in the flowchart in Figure 3.1.1. It starts with a guess for r_0, then solves system (3.1.4) to obtain an estimation for r_0. After that, a check is made for the difference between the result from the integration and our guess

$$m = r_{new} - r_{guess}, \tag{3.1.5}$$

is made, to see if it is less than the tolerance.

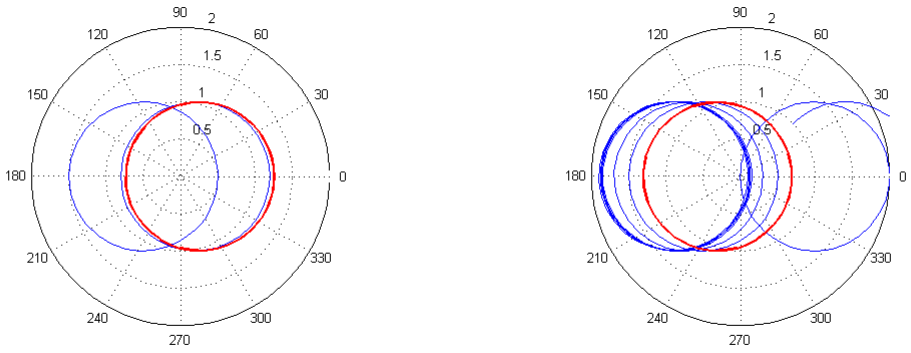

Figure 3.1.2: Graphical illustration of the shooting process . Left picture when initial guesses for r_0 are 0.5 and 1.2. Right picture guesses for r_0 are 0.5 and 2.

Unless the absolute value of m is less than the tolerance, the algorithm continues with the second guess for r_0 and repeat the process from the beginning. If the error is not within an acceptable tolerance, will continue updating r_0 according to the secant rule (3.1.6). The secant rule updates the radius considering the previous two radii and the error between them, m from (3.1.5), using the following formulation

$$r_{0,i} = r_{0,i-1} - \frac{r_{0,i-1} - r_{0,i-2}}{m_{i-1} - m_{i-2}} m_{i-1}. \tag{3.1.6}$$

It will iterate, to adjust the guess, until the stop criterion is satisfied, which means m is less than the tolerance.

Further we will make some simulations to see how the method behaves.

Some graphical representations of the shooting process are presented in Figure 3.1.2. The “shoots", attempts of the shooting method that were not good, are represented in polar coordinates with blue, while the solution of the shooting method is marked with red.

The ODE solver used is ode45, which is based on Runge-Kutta method and it has a medium order of accuracy. We assume the tolerance to be 10^{-5} and a constant curvature $\kappa = 1$. The solution of the shooting process for r_0 is 1 for both of the figures and within the specified tolerance. The solution is correct considering formula (3.1.1). Note that for Figure 3.1.2(right) the blue circles have radius approximately between 1.0001 - 1.0010, but they are not solutions because they do not satisfy the tolerance.

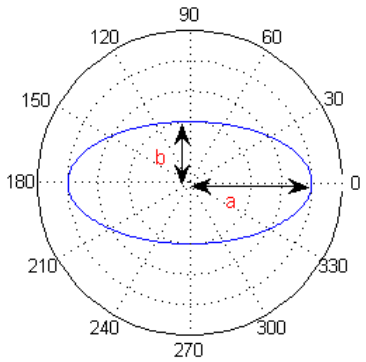

Figure 3.1.3: Eccentricity in the case of an ellipse

In order to point out how much the shape deviates from being circular, eccentricity is calculated

$$e = \sqrt{1 - \left(\frac{b}{a}\right)^2}, \tag{3.1.7}$$

because it is considered a flattening factor [14].

Here, a and b are the half major and half minor axes (see Figure 3.1.3). In the case of a circle, the eccentricity is zero, as for an ellipse it is $0 < e < 1$. In Figure 3.1.2(left), the eccentricity of the solution is 0.0642, which means that is very close to a circle, while in the other graph (right) the eccentricity of the solution is even better 0.0349.

Until now we have seen that the method works for a constant curvature. In order to check if the shooting method works properly, we need more complicated cases. Thus, we will replace the curvature κ which was constant, with different curvatures which depend on angle ϑ, like the curve of an ellipse or of a pear.

3.1.1 Example: the curvature of an ellipse

In order to test if the shooting method is working properly, we compute a curvature for a given radius. Then we use this computed curvature to find back that radius with the shooting method. We then compare this result with the original curve.

First, we check the method with the curvature of an ellipse, which we compute with formula (3.1.2), where we use the radius of an ellipse. The ellipse's equation, in polar coordinates, as a function of angle ϑ is

$$r(\vartheta) = \frac{ab}{\sqrt{(b\cos(\vartheta))^2 + (a\sin(\vartheta))^2}}. \tag{3.1.8}$$

In this formula a and b are the half of the major and minor radii. Note that if a and b are equal, we deal with a circle not with an ellipse. This formulation is relative to the ellipse's center.

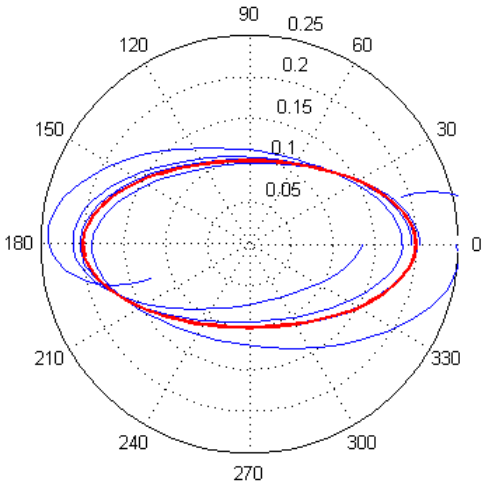

Figure 3.1.4: Shooting process considering the curve of an ellipse, with the major axis horizontal

Figure 3.1.4 is the graphical representation of the shooting process, with the curvature depending on ϑ for the curve of an ellipse. In this figure the absolute error between the desired shape and the computed one is really small. Here, the major axis is horizontal, while in Figure 3.1.5, the axes are switched and the method still works.

Another formulation for the radius of an ellipse, in polar coordinates with the origin at one of its foci, which depends on the eccentricity, is

$$r(\vartheta) = \frac{a}{1 - e\cos(\vartheta)}. \tag{3.1.9}$$

Here, a is the distance between the focus of the ellipse and the ellipse itself, measured by a perpendicular to the major axis, and e is the eccentricity.

Note that if eccentricity e is zero, the shape is of a circle rather than an ellipse.

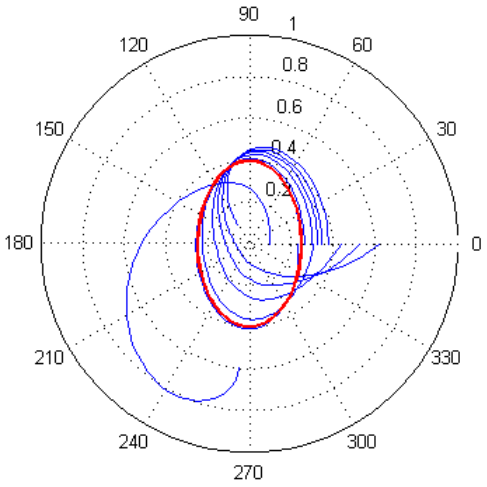

Figure 3.1.5: Shooting process considering the curve of an ellipse, with the major axis vertical

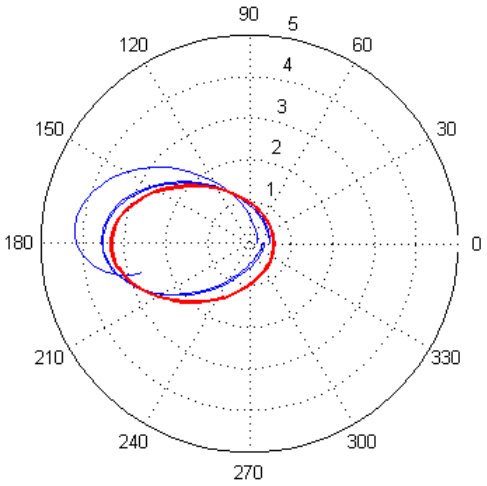

Figure 3.1.6: Shooting process for the curve of an ellipse

The graphical illustration of the shooting process in Figure 3.1.6, shows that the method works also in this case.

The shape is very accurate. The absolute error between the desired shape and the computed one is very small, around $error = 0.006$ for a tolerance of $tol = 10^{-5}$.

3.1.2 Example: the curvature of a pear shape

Another curve that we will compute, in order to test the shooting method, is a pear curve.

Again the curvature is computed with formula (3.1.2), for a given radius which corresponds to a pear curve. We want to obtain the same radius after we compute the curvature with the shooting method.

Assume the following formulation for a pear curve

$$r(\vartheta) = 1 + a\cos(\vartheta) + b\cos(3\vartheta), \tag{3.1.10}$$

where a and b are two coefficients. Note that if the coefficients are zero, we will obtain a circle.

We considered the function cosine, to have a symmetry over the x-axis.

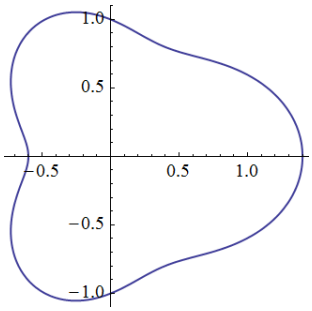

Figure 3.1.7: Pear curve

In Figure 3.1.7 we have the representation of formula (3.1.10) where both coefficients are $a = b = 0.2$.

Using formula (3.1.10) for the radius, we compute the curvature and we test the shooting method with it. For the first case, let's assume that the coefficients are both $a = b = 0.1$, so the expected shape should be between a circle and the shape shown in Figure (3.1.7),which is actually obtained in Figure 3.1.8.

Further we will increase a bit the value of the coefficients, to $a = b = 0.2$. The shape obtained in Figure 3.1.9 looks similar to Figure (3.1.10), so it works also for this curvature.

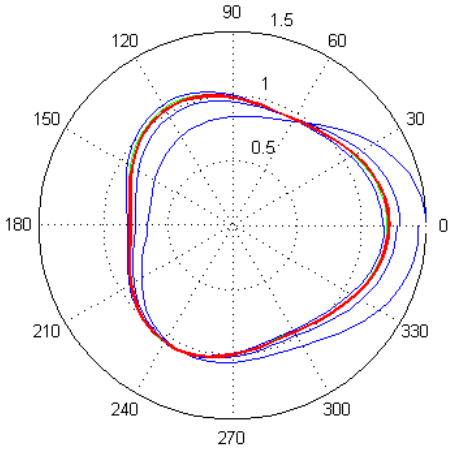

Figure 3.1.8: Shooting process, with the curvature of a pear

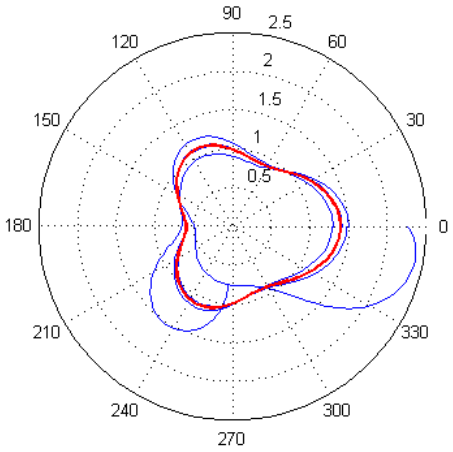

Figure 3.1.9: Shooting process, with the curvature of a pear

The shooting method worked successfully for all tests with different curves. Now, knowing that the method works, we look add pressure to computations.

3.1.3 Curvature from pressure computations

First step is to add pressure to system (3.1.4). For that we can consider the Young-Laplace equation [18]

$$\Delta p = \gamma \left(\frac{1}{R_1} + \frac{1}{R_2} \right), \tag{3.1.11}$$

where Δp is the pressure difference, γ is the surface tension, R_1 and R_2 are the principal radii of curvature.

Small droplets have spherical shape, so the principal radii of curvature are the same $R_1 = R_2 = R$ and (3.1.11) can be written as

$$\Delta p = \frac{2\gamma}{R}, \tag{3.1.12}$$

which can be redefined if we consider (3.1.1) for a 2D case, as

$$\Delta p = \gamma \kappa. \tag{3.1.13}$$

Moreover, the pressure difference can be written as the difference between the inside pressure and the outside pressure [18]

$$\Delta p = p_i - p_o.$$

In general pressure difference is written in terms of gauge pressure [9] (difference between absolute and atmospheric pressure is approximately - 10^5Pa) as

$$\Delta p = p_i - p_o = (p_i - p_\infty) - (p_o - p_\infty),$$

$$\Delta p = \hat{p}_i - \hat{p}_o. \tag{3.1.14}$$

The outside gauge pressure in terms of pressure coefficient (Cp) [29] is

$$\hat{p}_o = \frac{1}{2} \rho U_\infty^2 Cp, \tag{3.1.15}$$

where Cp depends on theta, as in (2.2.22) and U_∞ is the terminal velocity

$$U_\infty = \sqrt{\frac{\rho V g}{\frac{1}{2} C_D \rho A}}, \tag{3.1.16}$$

where $\rho = 1.225\,\mathrm{kg/m^3}$ is density, $g = 9.81\,\mathrm{m/s^2}$ is gravity, C_D is the object's drag coefficient,V its volume and A its area.

This formula is obtained by equaling drag force with gravity force, $F_d = F_g$, where F_g is defined in (2.2.19) and F_d in (2.2.20). Note that the drag coefficient depends on the hitting area. Choosing a long cylinder of volume V as the falling object, the hitting area A is a circle. The drag coefficient [29] for a long cylinder is $C_D = 0.82$. After all simplifications formula (3.1.16) leads to

$$U_\infty = \sqrt{\frac{\pi R g}{C_D}}.$$

Considering the symmetry of a droplet around its major axis, we refer to a 2D case; at rest the inside gauge pressure is defined by

$$\hat{p}_i = p_i - p_\infty = \frac{\gamma}{R_0}. \tag{3.1.17}$$

Having all necessary data, we can replace curvature κ in ODE (3.1.4) with equation (3.1.14):

$$\kappa = \frac{1}{\gamma}\left(\frac{\gamma}{R} - \frac{1}{2}\rho U_\infty^2\left(1 - 4sin^2\vartheta\right)\right), \tag{3.1.18}$$

where $\hat{p}_i$ and $\hat{p}_o$ are taken from (3.1.17) and (3.1.15) respectively. Here the surface tension for water-air axis at 25 °C is γ =0.072 N/m, the density of air at 15 °C is ρ =1.225 kg/m^3 (standard atmosphere), the ϑ angle is considered between 0 and 2π and the terminal velocity U_∞, defined in (3.1.16).

Plugging curvature (3.1.18) into the shooting method, closes the ODE system. In the obtained results, we found that pressure influences the shape of the droplet. The radius of the droplet is important on how much pressure will act over the shape. This influence can be seen in the next example.

In specific, a small droplet, like the one in Figure 3.1.11, with radius of $r = 0.002$, will not be influenced too much by the pressure. As for bigger droplets, like the one in Figure 3.1.12, we calculate p_i for a radius of $r = 0.02$ and the resulting radius is $r = 0.0173$. Therefore, pressure is a factor that affects the deformation of large droplets. An aspect that we will compare is the area of the deformed droplet with the area of the droplet at rest.

Considering a segment of a circle, where r is the radius and ϑ is the angle, the arc length (see Figure 3.1.10) is

$$ds = rd\vartheta.$$

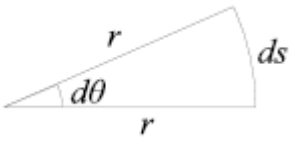

Figure 3.1.10: Arc length

The triangle that can be formed for every segment of circle has an area of

$$A = l\frac{h}{2} = ds\frac{h}{2} = rd\vartheta\frac{h}{2},$$

$$A = \frac{r^2}{2}d\vartheta.$$

So, the area of the deformed droplet will be

$$A_{droplet} = \int\int r(\vartheta)drd\vartheta = \int_{2\pi}^{0} A(h)dh = \int_{2\pi}^{0} \frac{r^2}{2}d\vartheta$$

and we compare it with the area of the circle

$$A_{rest} = \pi R^2.$$

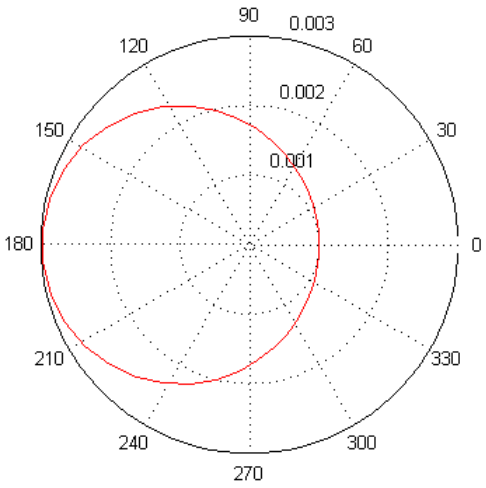

Figure 3.1.11: Shape unaffected by the pressure

In both cases (Figure 3.1.11 and 3.1.12), the difference between the area of the deformed droplet and the droplet at rest is negligible, because it is around 10^{-6} or smaller.

A remarkable fact is the flattening factor of the second droplet, which increased to $e = 0.5035$.

Note that even though pressure's influence can change the shape of larger droplets their surface is preserved.

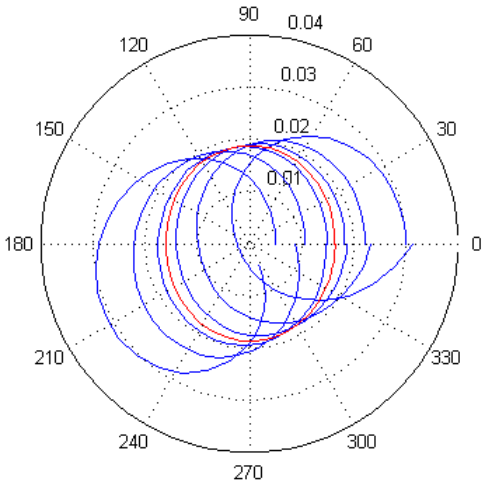

Figure 3.1.12: Shape affected by the pressure

3.1.4 Pressure jump from numerical simulations

In the last approach, we start by taking pressure data from COMSOL. They are computed for a circular rigid bubble in a flow field described by Navier-Stokes equations. Afterwards, we translate these pressure data into curvature through the inside pressure p_i and according to

$$\kappa = \frac{p_i + p_{dif}}{\gamma}.$$

The surface tension of water-air is γ =0.072 N/m and $p_{dif}(\vartheta) = p_{com}(\vartheta) - \overline{p_{com}(\vartheta)}$ is the pressure information from COMSOL after subtracting the pressure average. Finally, we compute the radius of the deformed droplet with the root finding method.

Test cases include droplets with radius $r = 0.5$ mm and the velocity of $v = 1$ m/s and $v = 10$ m/s.

In Figures 3.1.13 and 3.1.14, droplets have the same size, but the velocity is different. The second droplet deviates from being circular because the velocity influences the shape of the droplet. This happens because with a higher velocity comes also higher force applied over the droplet, which means higher pressure. This can be seen also from Figure 2.2.14 c where the highest pressure is 62.559Pa, while in Figure 2.2.13 for a smaller droplet the highest pressure is 0.7001Pa.

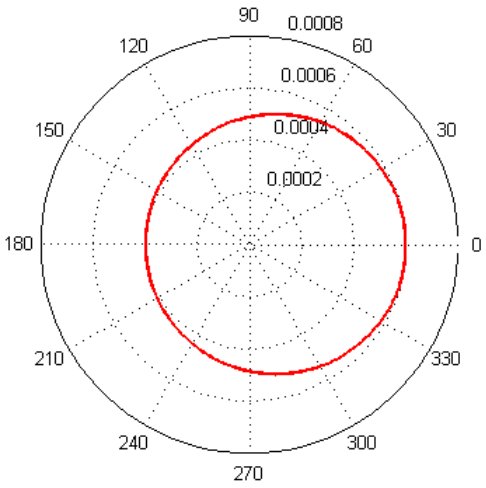

Figure 3.1.13: Shape unaffected by the pressure

In Figure 3.1.14, the deformed droplet is represented with red and with green the droplet at rest is shown. The flattening factor of the deformed droplet is $e = 0.7542$. Note that the area of the droplet has not changed during the deformation. The difference in area between the flat one and the circular one is around 10^{-10}.

From the simulations we observe that droplets have different shapes, from circular to more flattened shapes. What influences the shape is the dimension of droplet and the velocity of its fall.

We have seen that bigger droplets tend to deform their shape, while smaller droplets remain the same, with a circular shape. Assuming droplets of the same size, which fall with different velocity, they will have different shapes. Those which fall faster will get a deformed shape.

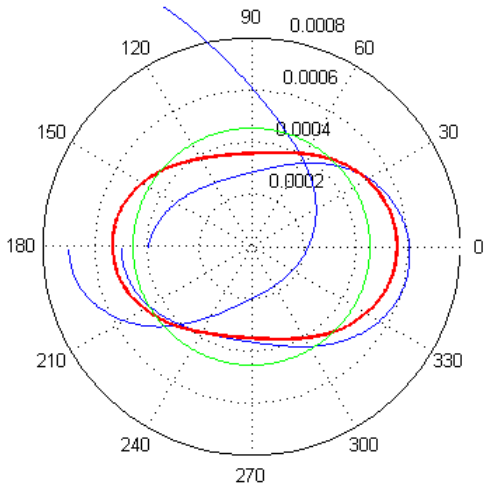

Figure 3.1.14: Shape affected by the pressure

3.1.5 Stiffness

A precise mathematical definition of stiffness cannot be found in literature. Stiffness is a difficult concept in the numerical solution of ODE.

Stiff differential equations are usually considered these differential equations which numerical methods that are used to solve them end up being numerically unstable.

The idea of stiffness appears when the solution being sought is varying slowly, but there are nearby solutions that vary rapidly.

Runge-Kutta methods, explicit methods, cannot handle stiff systems in an economical way, if they can handle them at all. An explicit method solves a stiff system by reducing the step size in order that the stability is retained. This needs to compute a large number of steps. The way out of this problem is to use implicit methods.

Consider the linear differential system

$$y' = Ay + b(x),$$

where $y, b \in \mathbb{R}^n$ and A is a constant $n \times n$ Jacobian matrix, with eigenvalues $\lambda_i \in \mathbb{C}$, $i = 1, 2...n$.

The Jacobian matrix is the matrix of all first-order partial derivatives of a vector function. So, matrix A is defined by

$$A = \begin{bmatrix} \frac{\partial f1}{\partial x_1} & \cdots & \frac{\partial f_1}{\partial x_n} \\ \vdots & \ddots & \vdots \\ \frac{\partial f_n}{\partial x_1} & \cdots & \frac{\partial f_n}{\partial x_n} \end{bmatrix},$$

where

$$\begin{cases} y_1 = f_1(x_1, ..., x_n) \\ \vdots \\ y_n = f_n(x_1, ..., x_n) \end{cases},$$

for a given set $\mathbf{y} = \mathbf{f}(\mathbf{x})$ of n equations in n variables $x_1, ..., x_n$.

For an ODE with λ_i the eigenvalues of the constant matrix, stiffness arises when $|Re(\lambda_{max})|$ is very large and $|Re(\lambda_{min})|$ is very small. This leads to the ratio

$$r = \frac{|Re(\lambda_{max})|}{|Re(\lambda_{min})|}, \tag{3.1.19}$$

which is a measure of stiffness of the system, according to Lambert's [17] first statement :

"A linear constant coefficient system is stiff if all of its eigenvalues have negative real part and the stiffness ratio is large.".

There is no exact value of the stiffness ratio r that would distinguish the non-stiff problems from the stiff-problems. However, for ratios around 1000, problems are starting to become stiff and implicit methods are likely to be more efficient than explicit methods. So, the effect of stiffness is more pronounced, the larger the quantities become.

An aspect that has to be mentioned, is the fact that there can be eigenvalues having zero their smallest modulus of the real part. The contribution of that eigenvalue to the exact solution is then constant. Lambert mentions that in this case if the moduli of the real parts of the remaining eigenvalues are not particularly large, the system is considered non-stiff.

Furthermore, we will consider the non-linear system of ODE that we used to calculate droplet shapes

$$\begin{cases} r' = u \\ u' = r + 2\frac{u^2}{r} - \frac{\kappa(\vartheta)}{r}(r^2 + u^2)^{3/2} \end{cases},$$

where ϑ is from 0 to 2π, with the initial conditions $r(0) = r_0$ and $u(0) = 0$.

The first step is the linearization of the system, by using Taylor series, which in 1D is defined for a function of $f(x)$ as:

$$f(x) = \sum_{n=0}^{\infty} \frac{f^n(a)}{n!}(x-a)^n,$$

and for a function $f(x,y)$ in 2D as:

$$f(x,y) \approx f(a,b) + (x-a)f_x(a,b) + (y-b)f_y(a,b) + \mathcal{O}(h^2),$$

where f is evaluated at points a and b, which are the initial conditions. The latter is the form that we use here.

After linearization the system becomes

$$\begin{bmatrix} r' \\ u' \end{bmatrix} = \begin{bmatrix} 0 & 1 \\ 1 - \frac{2u_1^2}{r_1^2} - \kappa\gamma & \frac{4u_1}{r_1} - \kappa\delta \end{bmatrix} \begin{bmatrix} r \\ u \end{bmatrix} + \begin{bmatrix} 0 \\ \varepsilon \end{bmatrix}, \tag{3.1.20}$$

where κ is a curvature depending on ϑ and

$$\gamma = -\frac{1}{r_1^2}(r_1^2 + u_1^2)^{3/2} + 3(r_1^2 + u_1^2)^{1/2},$$

$$\delta = \frac{3u_1}{r_1}(r_1^2 + u_1^2)^{1/2},$$

$$\varepsilon = \frac{1}{r_1}(r_1^2 + u_1^2)^{3/2} + \kappa r_1\gamma + \kappa u_1\delta,$$

with r_1 and u_1, the initial conditions, which are given.

We can rewrite system (3.1.20) as

$$\begin{bmatrix} r' \\ u' \end{bmatrix} = A \begin{bmatrix} r \\ u \end{bmatrix} + b(\vartheta). \tag{3.1.21}$$

Now, we can use the eigenvalue of the Jacobi matrix A to test the stiffness of the system (3.1.21), for different curvature functions $\kappa(\vartheta)$ and different initial conditions $r(0)$ and $u(0)$.

First case, assume the curvature to be constant ($\kappa = 1$) and the initial conditions $r_0 = 0.5$ and $u_0 = 0$. The shape obtained is represented in Figure 3.1.15.

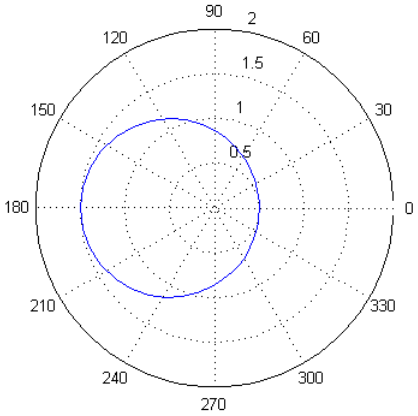

Figure 3.1.15: Shape, for $\kappa = 1$, initial values $r(0) = 0$ and $u(0) = 0$

In order to find the stiffness of system (3.1.21), we compute the eigenvalues for every ϑ, with the same initial conditions. Figure 3.1.16, is the graphical representation of the distribution of the eigenvalues on the real and imaginary axis. It is shown that there are eigenvalues that have negative or positive real part, but at the same time there are eigenvalues that have only imaginary part with zero real part. The latter kind of eigenvalues will not contribute to the stiffness of the system. As Lambert says in the first statement, we have to focus on the eigenvalues with big negative real part; this is not the case in our situation. From these data we can say that the system is non-stiff.

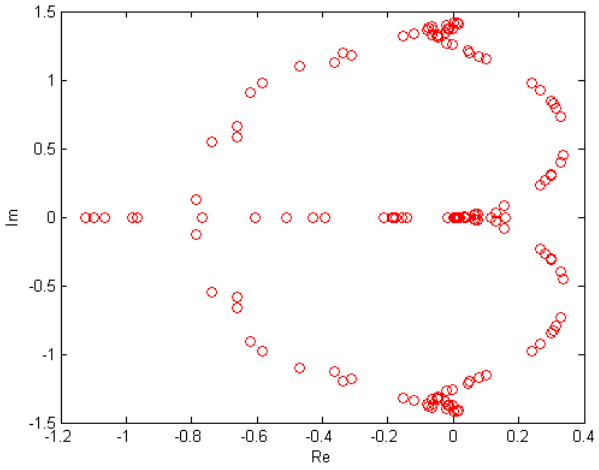

Figure 3.1.16: Values of the eigenvalues for every angle ϑ

For the second part of the statement (large ratio implies stiffness), we will compute the ratio of the eigenvalues (3.1.19). In Figure 3.1.17 the values of the ratio for all ϑ angles is shown. Since for singular ratios a non-stiff system occurs, we represent these ratios with null in the aforementioned graph. As we expected the system is non-stiff, for the assumed initial values, because the biggest ratio ($r \approx 17$) is too small to talk about a stiff system.

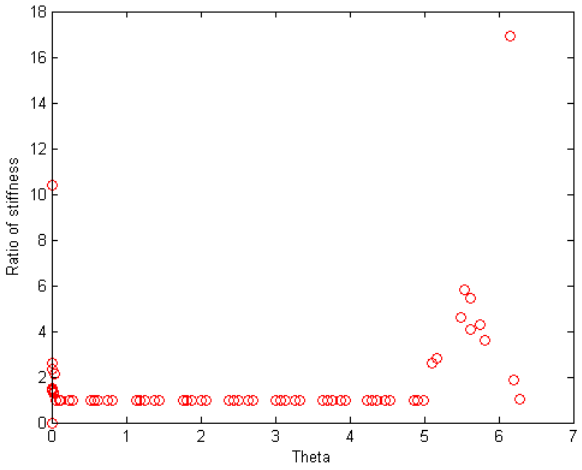

Figure 3.1.17: Ratio of stiffness for every angle ϑ

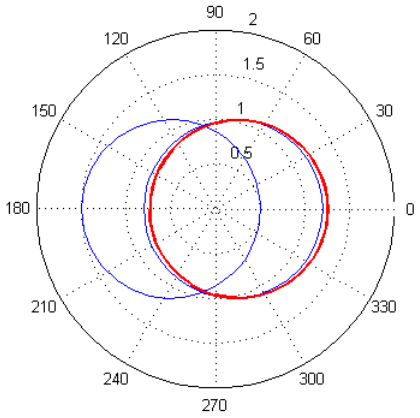

Figure 3.1.18: Graphical representation of the shooting process

In order to see if there are some changes during the shooting process (Figure 3.1.18),

we computed the eigenvalues (Figure 3.1.19) and the ratio for the hole process (Figure 3.1.20), because the values of $r(0)$ and $u(0)$ will change with every "shoot" of the method. Note that the process have a tolerance of $tol = 1e-5$.

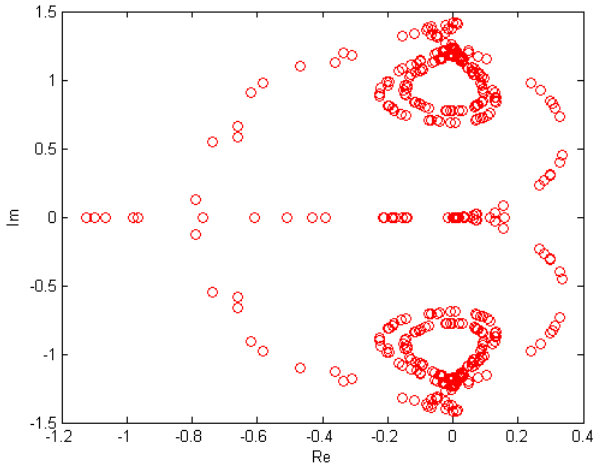

Figure 3.1.19: Values of the eigenvalues for every angle ϑ

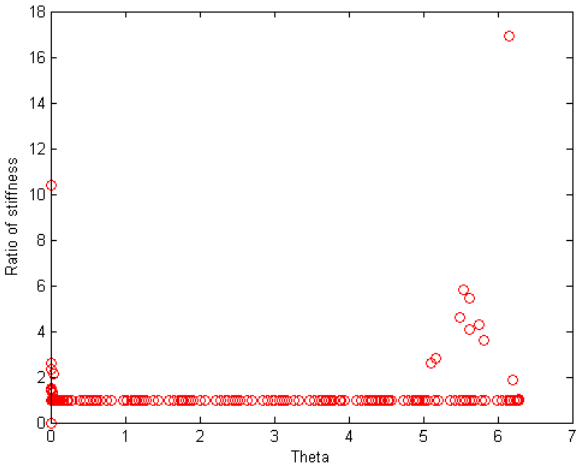

Figure 3.1.20: Ratio of stiffness for every angle ϑ

We can see that the values do not change very much, so we can talk about non-stiffness during the whole shooting process.

For the same curvature, if we change the initial value with $r(0) = 2$, the problem will

be totally different (Figure 3.1.21). The final system computed by the shooting method is stiff, because the ratio is $r > 1000$ (see Figure 3.1.22, 3.1.23).

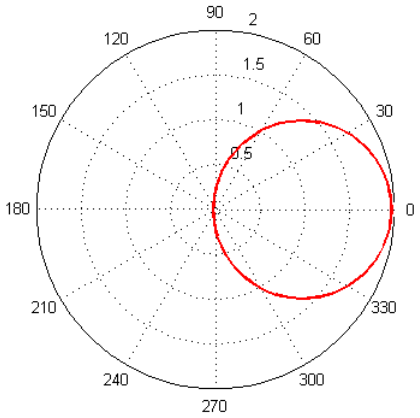

Figure 3.1.21: Graphical representation of the last “shoot" of the shooting process

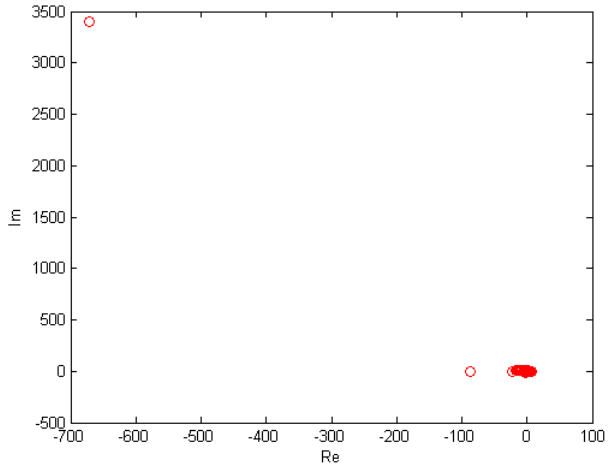

Figure 3.1.22: Values of the eigenvalues for every angle ϑ

The last two cases presented, demonstrate that initial values influence the stiffness of the problem. This happens because the Jacobian matrix and the eigenvalues are different.

Comparing the two cases with the same curvature, it is clear that the initial values influence the stiffness of the problem.

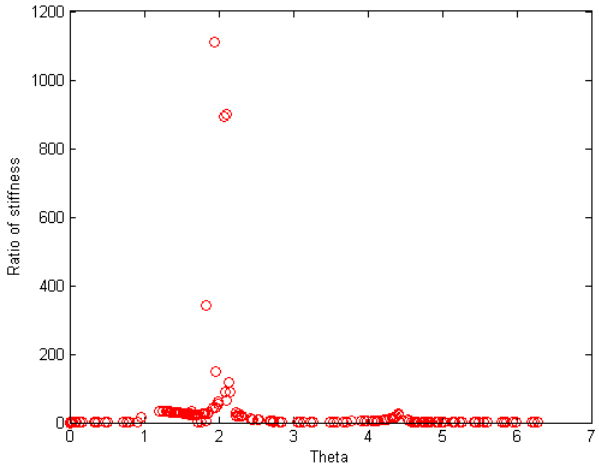

Figure 3.1.23: Ratio of stiffness for every angle ϑ

The second case for testing the stiffness, is when the curvature is an ellipse and κ will be computed by the formula

$$\kappa(\vartheta) = \frac{r^2 + 2(r')^2 - rr''}{(r^2 + (r')^2)^{3/2}}, \tag{3.1.22}$$

where r will be

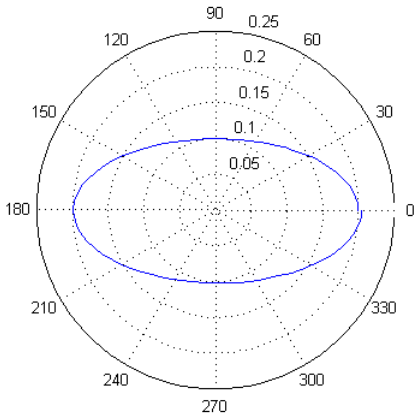

Figure 3.1.24: Graphical representation of the first “shoot" of the shooting process

$$r(\vartheta) = \frac{ab}{\sqrt{(b\cos(\vartheta))^2 + (a\sin(\vartheta))^2}}.$$

The initial values this time are $r(0) = 0.5$ and $u(0) = 0$, and the constants in the radius formula are $a = 0.2$ and $b = 0.1$. The shape obtained is represented in Figure 3.1.24.

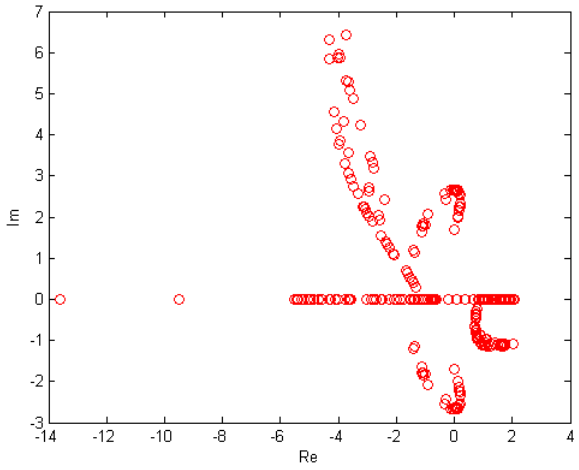

Figure 3.1.25: Values of the eigenvalues for every angle ϑ

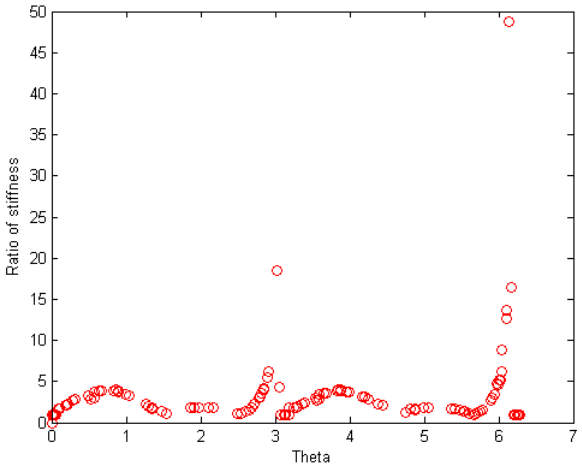

Figure 3.1.26: Ratio of stiffness for every angle ϑ

Data represented in Figure 3.1.25 and 3.1.26, satisfy both parts of the Lambert statement. There are no eigenvalues with large negative parts, and the ratio is small (largest

$r \approx 49$), so the system is non-stiff.

Further we computed the stiffness during the entire process of shooting (Figure 3.1.27), to see if the system remains non-stiff during the process.

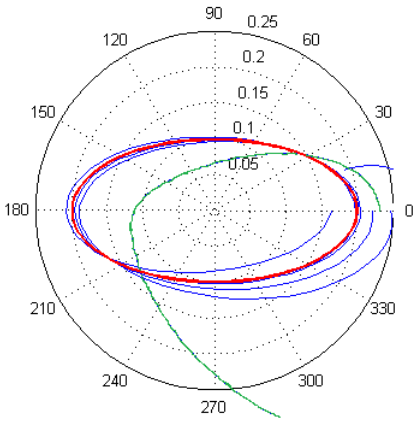

Figure 3.1.27: Graphical representation of the shooting process

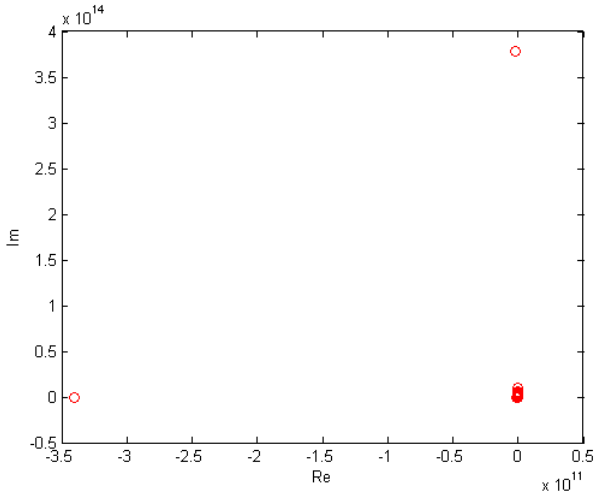

Figure 3.1.28: Values of the eigenvalues for every angle ϑ

Information obtained through Figure 3.1.28 and 3.1.29, lets us speak about stiffness. It is clear that there are eigenvalues with large negative real parts, and ratio is going up

to 3×10^9, which is a very big ratio. The stiffness of the shooting method, in this case comes from the attempt in computing the green line in Figure 3.1.27.

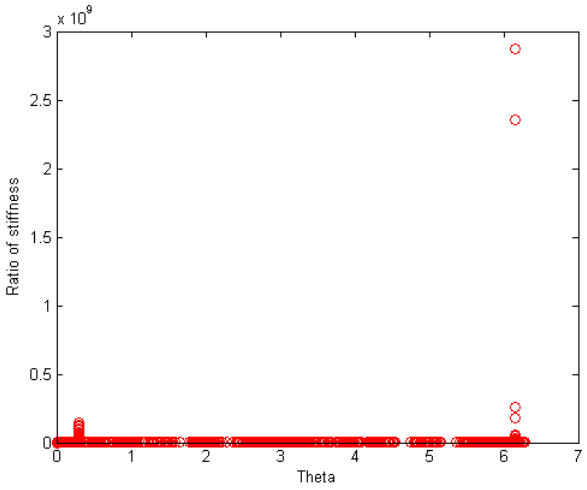

Figure 3.1.29: Ratio of stiffness for every angle ϑ

We analyzed separately the stiffness of the system that computed the final solution, not the whole shooting process (Figure 3.1.30).

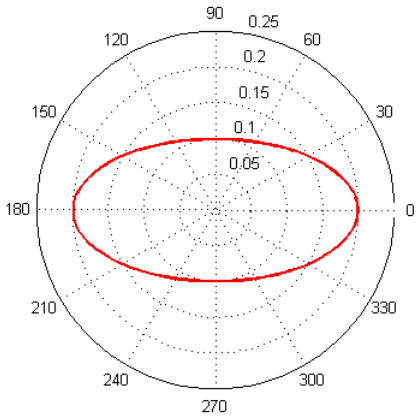

Figure 3.1.30: Graphical representation of the solution of the shooting process

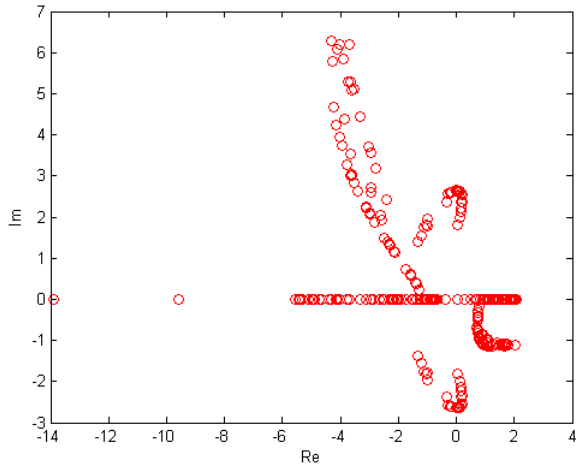

Figure 3.1.31: Values of the eigenvalues for every angle ϑ

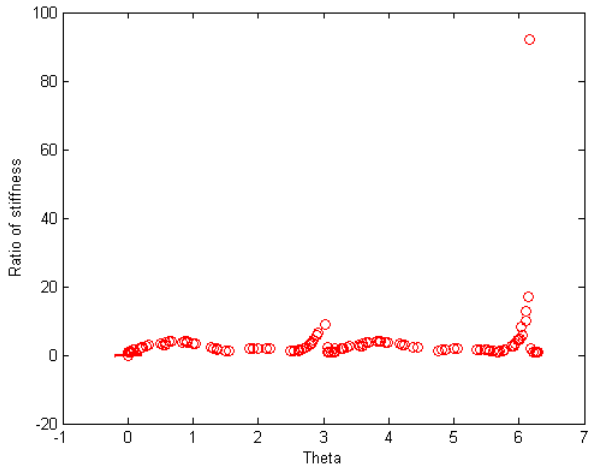

Figure 3.1.32: Ratio of stiffness for every angle ϑ

The representation of the eigenvalues for the shape that we are interested in, shows that there are no large eigenvalues with negative real parts (Figure 3.1.31), and also the ratio ($r \approx 95$, see Figure 3.1.32) is small enough to say that it is a non-stiff system.

The third case that we will test, is for a curvature of a pear, where κ is the formulation from (3.1.22), with the radius of

$$r(\vartheta) = 1 + a\cos(\vartheta) + b\cos(3\vartheta).$$

The initial conditions will be $r(0) = 1.3$ and $u(0) = 0$. The constants from the radius formula will be $a = b = 0.1$ (see representation in Figure 3.1.33).

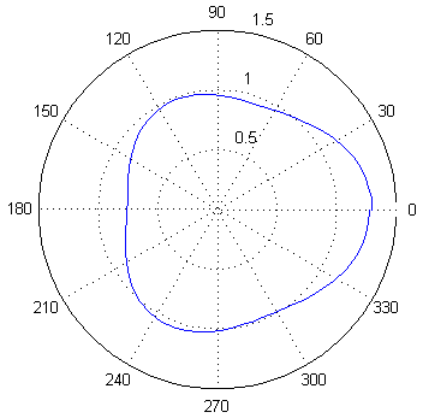

Figure 3.1.33: Graphical representation of the first “shoot" of the shooting process

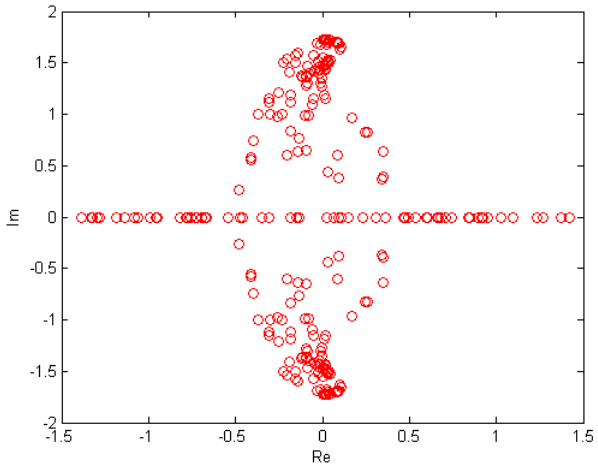

Figure 3.1.34: Values of the eigenvalues for every angle ϑ

The stiffness of the system is very low, because we have eigenvalues with very small negative real numbers (Figure 3.1.34), and also the ratio is very small ($r \approx 44$, see Figure 3.1.35). In this case the problem is considered non-stiff for the whole process of

shooting, because the negative real parts of the eigenvalues continue to be small, and the ratio goes only until $r \approx 145$.

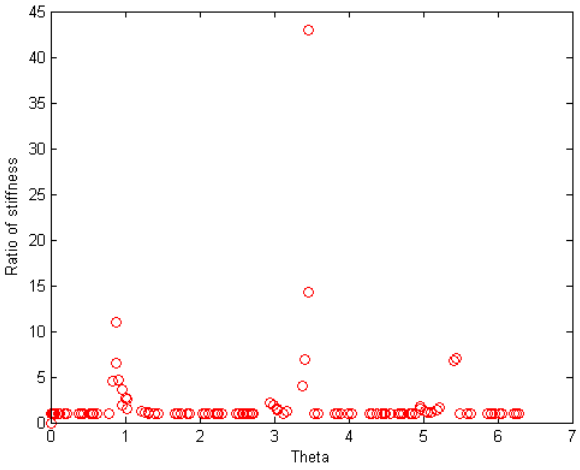

Figure 3.1.35: Ratio of stiffness for every angle ϑ

The computation of the solution (Figure 3.1.36) of the shooting method is non-stiff. This can be seen in the next figures 3.1.37, 3.1.38.

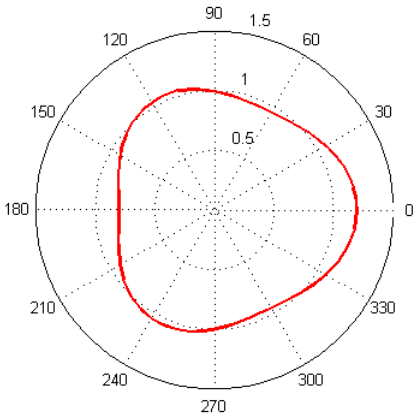

Figure 3.1.36: Graphical representation of the solution of the shooting process

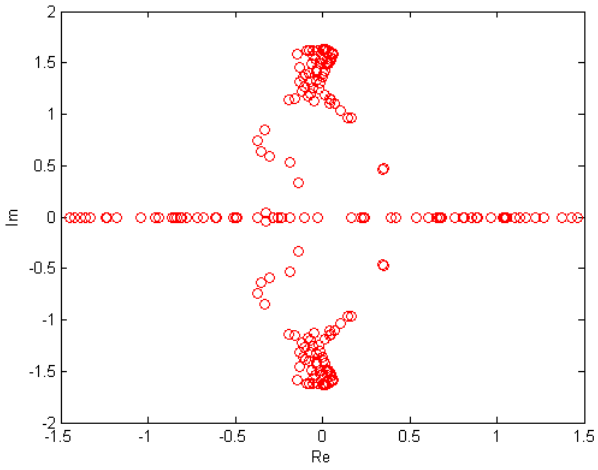

Figure 3.1.37: Values of the eigenvalues for every angle ϑ

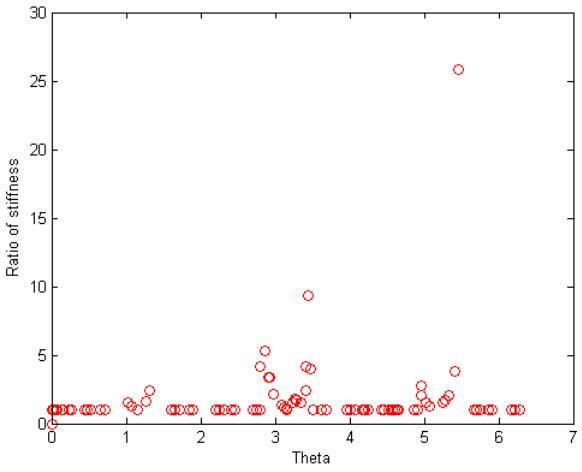

Figure 3.1.38: Ratio of stiffness for every angle ϑ

Let's assume that the initial condition remains the same $r(0) = 1.3$ and $u(0) = 0$, but we change the constants of the radius $a = b = 0.2$, in order to obtain a shape that looks more like a pear, Figure 3.1.39.

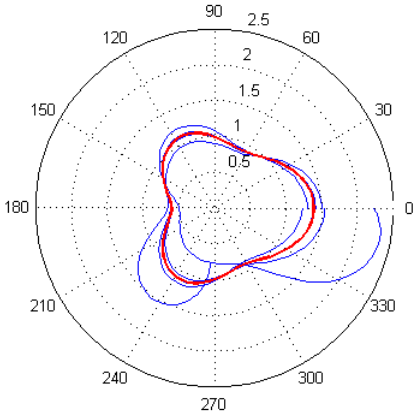

Figure 3.1.39: Graphical representation of the shooting process

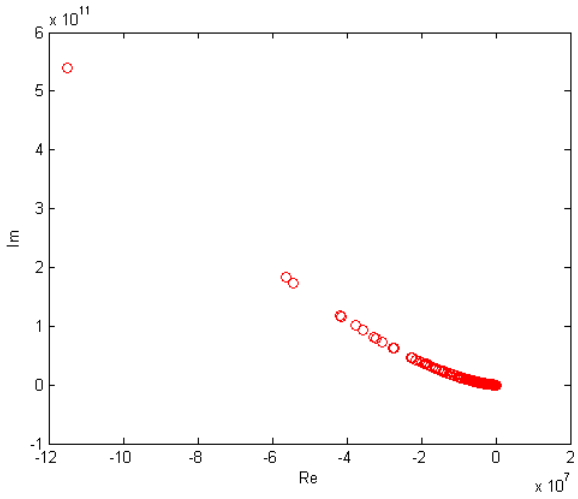

Figure 3.1.40: Values of the eigenvalues for every angle ϑ

Figure 3.1.40 and 3.1.41 represents data for all the “shoots" needed, until we found the solution of the process. It is clear that there are moments when the system is stiff (at angle $250\,^{\circ}\text{C} < \vartheta < 270\,^{\circ}\text{C}$), having eigenvalues with very big negative numbers, which lead to very big ratios. What we can notice is that this is happening most of the time in the same region of ϑ. This is not the case for the system that has to be solved for the right solution of the shooting method (Figure 3.1.42). In this case the values of

the eigenvalues are not so big (Figure 3.1.43), and the ratio is $r < 300$, Figure **3.1.44,** which means that the system is considered non-stiff.

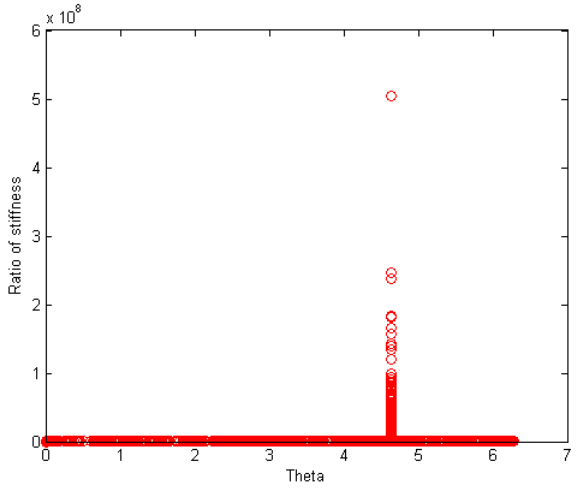

Figure 3.1.41: Ratio of stiffness for every angle ϑ

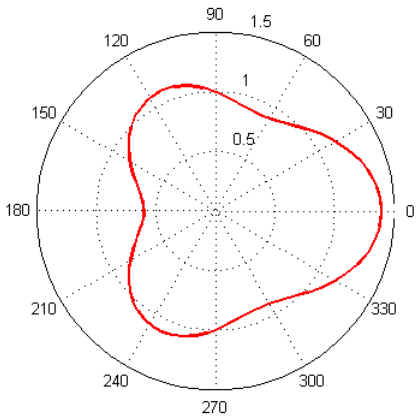

Figure 3.1.42: Graphical representation of the solution of the shooting process

The measurement of the stiffness of the ODE depends on the eigenvalues of the matrix, which is the constant Jacobian matrix. This matrix depends numerically on the initial values and physically on the curvature taken in consideration. The case of the pear, shows that a small change of the curvature κ, will become a small change in the

computation of the Jacobian matrix. In the case of curvature $\kappa = 1$, we saw that changes of the initial values can change the stiffness of the system.

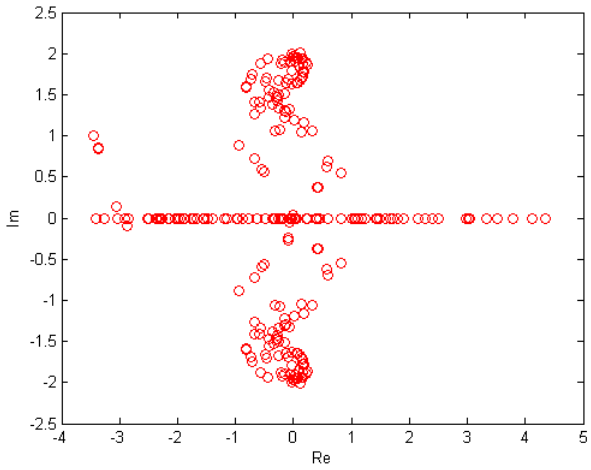

Figure 3.1.43: Values of the eigenvalues for every angle ϑ

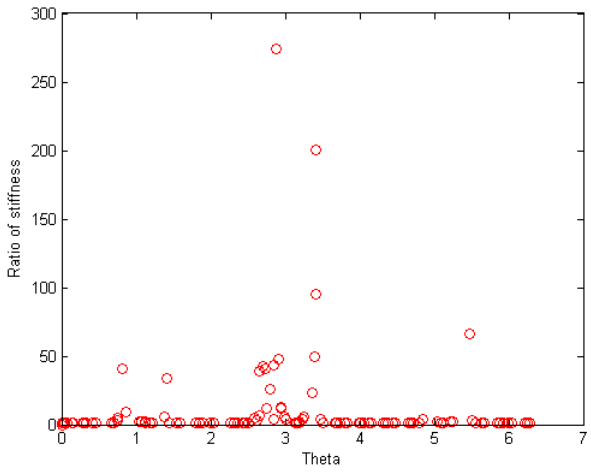

Figure 3.1.44: Ratio of stiffness for every angle ϑ

Stiffness is an efficiency issue. If we were not concerned about how much time a computation takes, we would not care about stiffness. Non-stiff methods can solve stiff problems; they just take a long time to do it.

3.2 Optimization

Another approach to the root finding algorithm, to compute a droplet shape, is the minimization technique. This technique is a mathematical optimization, which minimizes a real valued function by choosing repeatedly input values from some set of data and computing the values of the function.

What we want to do is to find a bubble with the curvature equal to a given curvature, which is considered an input. In order to do that, we start with a circular bubble, and we minimize the distance between the curvature of this bubble and the given curvature, with

$$\min_{r_1,r_2,\ldots} \sum_i \|\kappa(r_1, r_2, \ldots; \vartheta_i) - \kappa_0(\vartheta_i)\|^2 , \tag{3.2.1}$$

where κ_0 is the given curvature and $r_1, r_2, \ldots$ are radii at different angles ϑ.

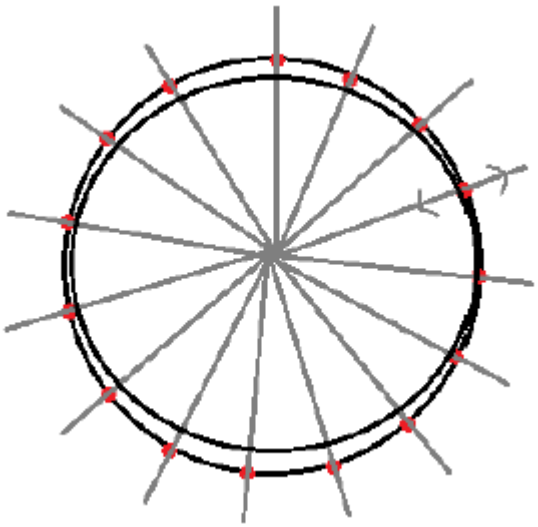

Figure 3.2.1: Graphical representation of the minimization technique

This technique, is represented graphical in Figure 3.2.1, where the outside shape represents the curvature of the bubble that we want to find, and the inside shape represents a given curvature. What we want to do is to take in consideration a lot of points on the curvature of our bubble, for different angles ϑ, and to move those points on the gray lines, until the distance between those two shapes is minimized.

Before finding a droplet shape, some tests are made with the method, using a given curvature for the shape of an ellipse and a pear. Then the curvature of the shape that

we are looking for is minimized considering the given curvature. In order for the method to work, the resulted shape should be as the input one.

3.2.1 Curvature from sample points

In order to compute the curvature we will use two different approaches. The first one is to compute the curvature by fitting circles through successive points. The second approach uses finite differences in the polar plane to compute the curvature.

3.2.1.1 Circle fitting

The curvature is a quantity that is usually more easily understood as one over the radius of curvature. The radius of curvature (C) is the radius (r) of the osculating circle in a point (A). A natural approach to determine the curvature in 2D is then to locally fit a circle.

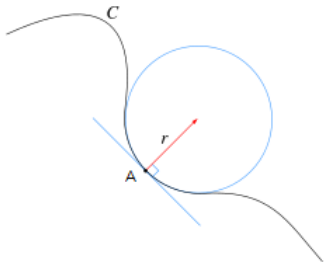

Figure 3.2.2: An osculating circle

The minimum number of successive points that is needed to compute the curvature is of course three, but the benefit of using a fitting method is that we can easily accommodate more points, by relying on a least squares fit. In order to attach the computed curvature to a point, we will look at the same number of neighbors on the left and right of a point, so the number should be of the form $2w + 1$, where $w \geq 1$.

We will use the function of Izhak Bucher (25 October 1991) [5] for circle fit. He starts from the implicit equation for a circle with the center at (x_c, y_c) and a radius r:

$$(x - x_c)^2 + (y - y_c)^2 = r^2.$$

Expanding this equation, we can introduce an alternative set of parameters (a, b, c):

$$x^2 + y^2 + ax + by + c = 0,$$

where $a = -2x_c$, $b = -2y_c$, and $c = x_c^2 + y_c^2 - r^2$.

Taking three successive points (x_{i-1}, y_{i-1}), (x_i, y_i) and (x_{i+1}, y_{i+1}), we see that all the squares not withstanding we find a linear system in terms of (a, b, c):

$$\begin{array}{rcrcrcl} x_{i-1}^2 + y_{i-1}^2 & + & ax_{i-1} & + & by_{i-1} & + & c = 0, \\ x_i^2 + y_i^2 & + & ax_i & + & by_i & + & c = 0, \\ x_{i+1}^2 + y_{i+1}^2 & + & ax_{i+1} & + & by_{i+1} & + & c = 0. \end{array}$$

In matrix notation, this becomes:

$$\begin{pmatrix} x_1 & y_1 & 1 \\ x_2 & y_2 & 1 \\ x_3 & y_3 & 1 \end{pmatrix} \begin{pmatrix} a \\ b \\ c \end{pmatrix} = \begin{pmatrix} -(x_1^2 + y_1^2) \\ -(x_2^2 + y_2^2) \\ -(x_3^2 + y_3^2) \end{pmatrix}, \tag{3.2.2}$$

The solutions of system (3.2.2), give us the radius of the circle that we fit for a specific point, using formula

$$R = \sqrt{(a^2 + b^2)/4 - c}.$$

Knowing the radius, curvature can be found with (3.1.1).

An important drawback of this method is that we do not get the sign of the curvature. This has to be determined otherwise: the direction of the vector pointing from the point to the center of the circle needs to be compared with the local curve normal.

There is nothing limiting using more than three points. Using a window width[1] of w we will find a $(2w + 1) \times 3$ matrix, which can be solved by an appropriate least squares method, such as QR or SVD. Common numerical wisdom holds that SVD is more robust than QR, and in numerical experiments below we indeed found that for normally distributed noise added to coordinates of samples of a circle (see below) SVD consistently predicted the center and radius more accurately than QR.

A graphical representation of how the method works is Figure 3.2.3, where we assumed a circle with radius $r = 1$. We considered 40 points to which we added 20 noise. The radius of the circle obtained, fitting those points, has a radius $r = 1.0190$. The result is very close to the initial one. Increasing the number of points, the result is much accurate.

[1] Window width indicates the amount of neighbours points taken in consideration for each point that we compute the curvature.

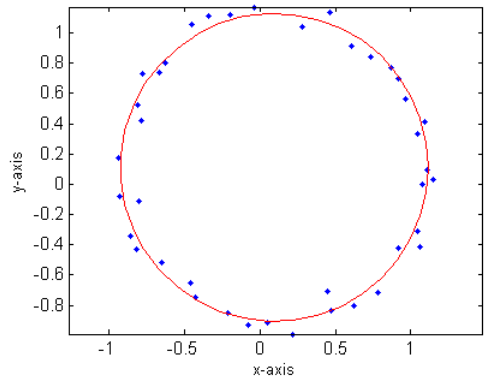

Figure 3.2.3: Circle fit for 40 points

3.2.1.2 Central differences

The second approach is to compute the curvature by using derivatives, considering formula (3.1.2), used for the root finding method to find the curvature. In that equation both the first and second order derivatives of r appear. Again we will use three points to estimate the curvature. Assuming a curve defined in polar coordinates as $r(\vartheta)$ and that the samples have been taken at equidistant ordinates $\vartheta_i = i\Delta\vartheta$, the standard scheme for the second order is

$$r''(\vartheta_i) = \frac{r_{i+1} - 2r_i + r_{i-1}}{h^2} + O(h^2).$$

Since we are using both r_{i+1} and r_{i-1} already, we also use a central difference scheme for the first derivative, which of course has the benefit of being accurate to a higher degree:

$$r'(\vartheta_i) = \frac{r_{i+1} - r_{i-1}}{2h} + O(h^2).$$

These approximations can be plugged into (3.1.2) directly. Like the previous method, this approach could be extended to include more points than just the direct neighbours. The aim is then not so much to increase the order, as to denoise the data. One approach is to construct $O(h^2)$ - schemes that use more neighbors, but it is probably better to denoise the data in a separate step by seeing r_i as a noisy signal.

3.2.2 Smooth and noisy data

An aspect that we have to take in consideration is the fact that data which we receive to compute is not always smooth. Sometimes, almost all the time we receive noisy data from measurements.

For example, noisy data for a circle with radius of $r = 1$ and noise of 2% or 20%, will look like in Figure 3.2.4. Observe that the second picture has 10 times more noise.

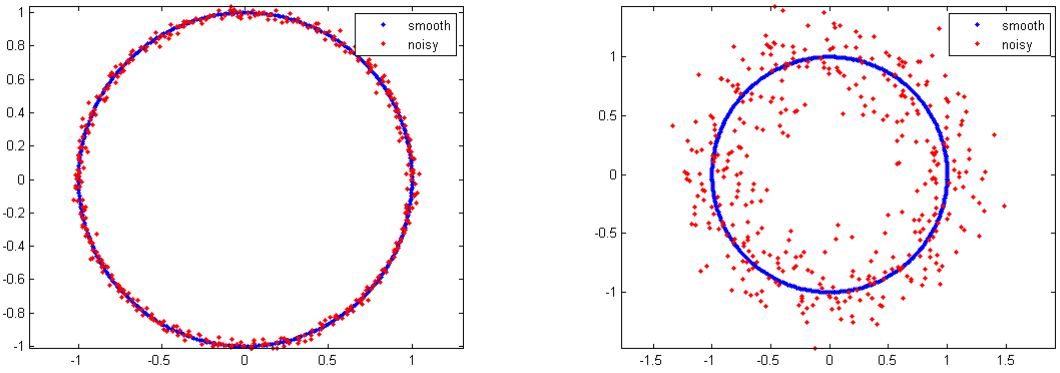

a) 2% noise

b) 20% noise

Figure 3.2.4: Circle with radius $r = 1$ and noise

If we have noisy data, like in Figure 3.2.5a, we can approximate the radius of the circle that can be created with that data, by using Izhak Bucher algorithm of circle fit [1], described before. The function will return the radius and the x, y coordinates of the center of the circle for every theta. To test the algorithm, we take a circle with radius of $r = 1$, to which we apply 20% noise, and then we compute the circle fit algorithm. The result can be seen in Figure 3.2.5.

The outcome is very close to the original one.

Furthermore both methods which compute the curvature are tested to see differences in accuracy.

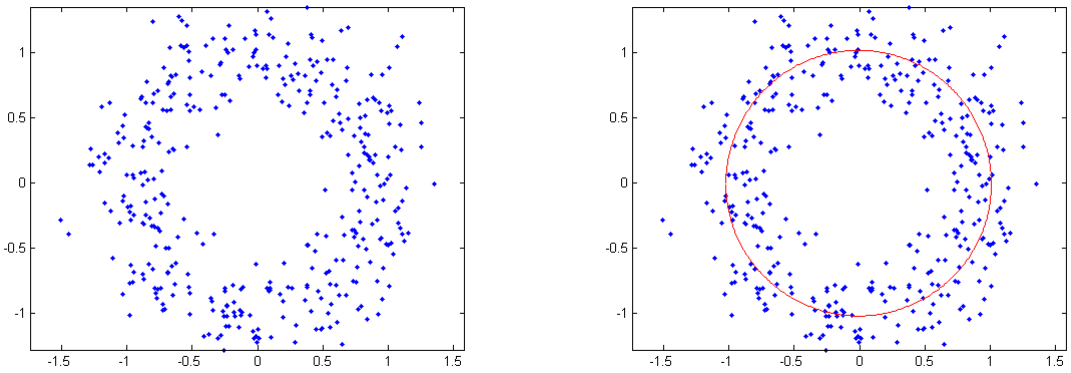

a) 20% noise added to a circle with radius $r = 1$ b) approximated shape, circle with a radius $r = 1.0179$

Figure 3.2.5: Circle with radius of $r = 1$ and noisy data

For smooth data, tests are made for the first method with three, five and seven points and one for the second method. A circle of radius $r = 0.2$ is considered. In Figure 3.2.6b, the solution of the second method is the most interesting. This method is very accurate and that is why it does not appear in Figure 3.2.6a, where the error is plotted. Method one is more accurate when we use a bigger amount of points to compute the curvature, Figure 3.2.6a. This means that we use more neighbors for each point. For smooth data is better to use the second method, because is the most accurate.

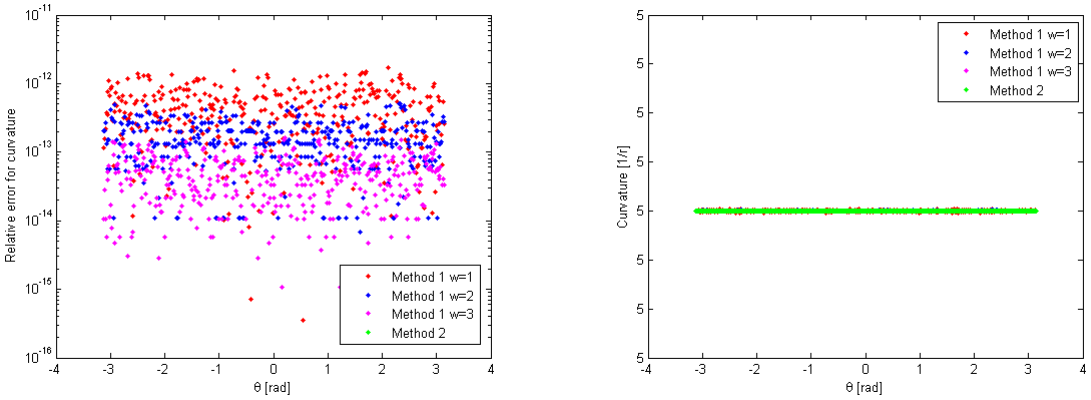

a) Relative error for the curvature b) Curvature, computed with different methods

Figure 3.2.6: Computing the curvature for smooth data, where the number of points for method two are computed by formula $Nr = w * 2 + 1$. Note that "method 1" is the circle fit method and "method 2" is the central differences method.

For tests with noisy data, we used a circle with radius $r = 0.2$, for which we added 1% noise. What this means can be seen in Figure 3.2.7, where the difference between noisy and smooth data is visible.

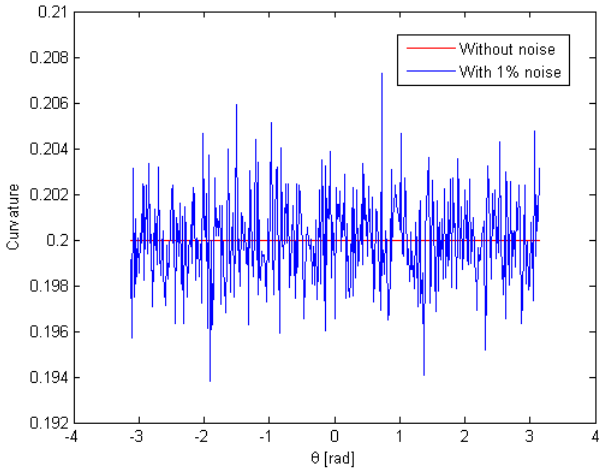

Figure 3.2.7: Radius with 1% noise

For noisy data, in Figure3.2.8a, can be seen that the second method does not give good results as before. There are two cases of method one that cannot be seen. This happens because the solutions of those two are very close to the exact solution. Figure 3.2.8b illustrates how close are the results of these two cases, to the exact solution.

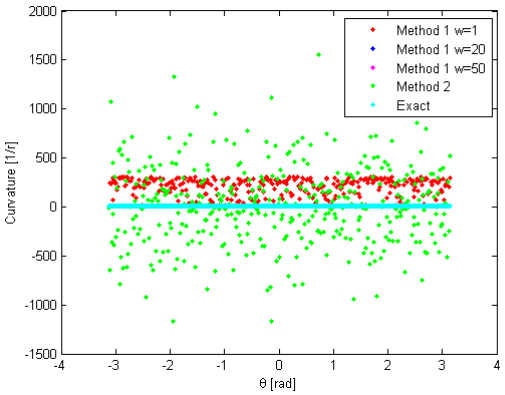

a) Curvature, computed with different methods

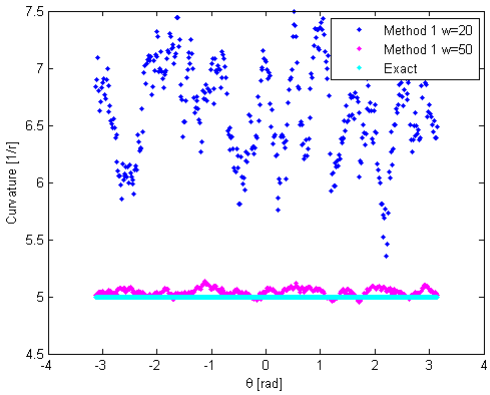

b) Solutions that are closer to the exact one

Figure 3.2.8: Computing the curvature for noisy data, where the number of points for method two are computed by formula $Nr = w * 2 + 1$. Note that "method 1" is the circle fit method and "method 2" is the central differences method.

The relative error for the curvature is computed to check which method is more accurate

$$error = \frac{|curvature_{computed} - curvature_{exact}|}{curvature_{exact}},$$

for all four cases taken in consideration before. From Figure 3.2.9 it is clear that when the initial data have noise, method one is more accurate, but only when we take a lot of points. For a few points the results are pretty close to the results of the second method.

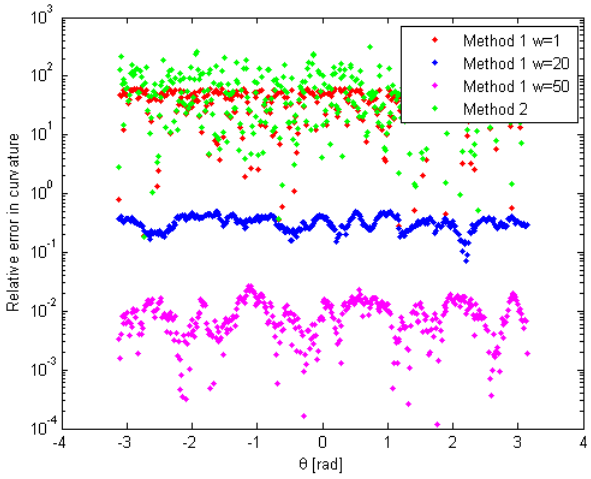

Figure 3.2.9: Relative error for curvature with noisy initial data. Note that "method 1" is the circle fit method and "method 2" is the central differences method.

All in all, it is proved that the first method works better when we have to deal with noisy data and the number of points plays an important role. An increase in the number of points enhances the accuracy of the first method. When the initial data are smooth, the second method gives better results.

3.2.3 Results

One way to optimize a problem is stated in terms of minimization. In our case we will minimize the curvature, in order to find the best solution. Some tests are made to see how good the method works.

3.2.3.1 Curvature of an ellipse

For the first case we want to obtain the ellipse given by (3.1.8), where $a = 0.2$ and $b = 0.1$, and is depicted in Figure 3.2.10. This ellipse's curvature is plotted in Figure 3.2.11.

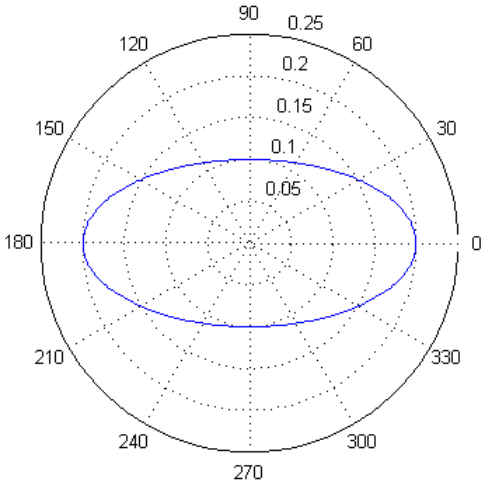

Figure 3.2.10: Ellipse shape for radius (3.1.8), where a and b are the half of the major and minor radii.

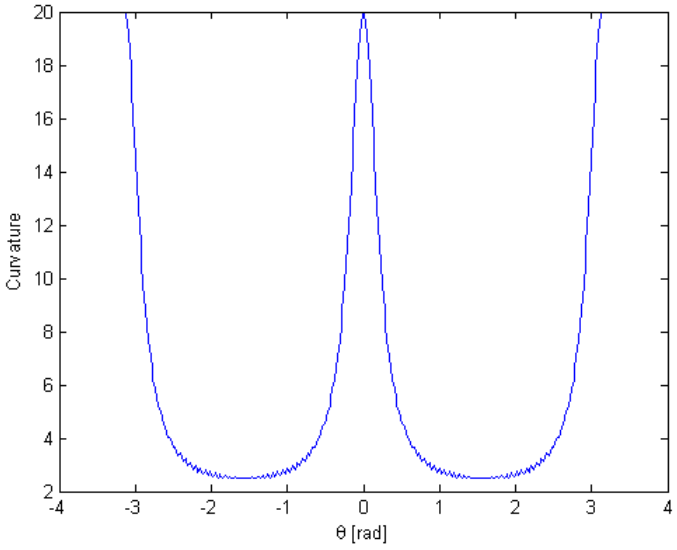

Figure 3.2.11: Curvature of the ellipse from Figure 3.2.10

After computing the minimization function (3.2.1), for a circle of radius $r = 0.2$, the obtained shape is almost the same as in Figure 3.2.10. That is because the relative error of the radius between those two is really small, around 10^{-13}.

So, the minimization function works very well considering the curvature of an ellipse.

3.2.3.2 Curvature of a pear

Further we would like to obtain the curve of a pear, give by formula (3.1.10). Assuming the initial shape to be a circle of radius $r = 1$, after minimization of the curvature with (3.2.1), the circle transforms into a pear shape, like the desired one (the red line in Figure 3.2.12 becomes the blue one).

The relative error between the radii of the solution and the desired solution is again very small, around 10^{-12}. Note that the error peaks around 180 degrees (Figure 3.2.13), where the curvature changes sign.

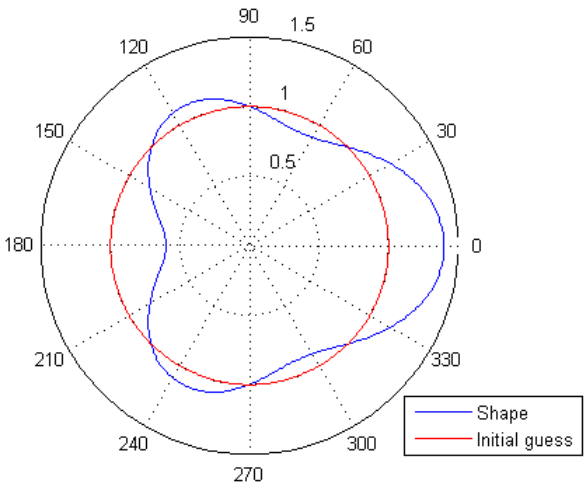

Figure 3.2.12: Pear shape

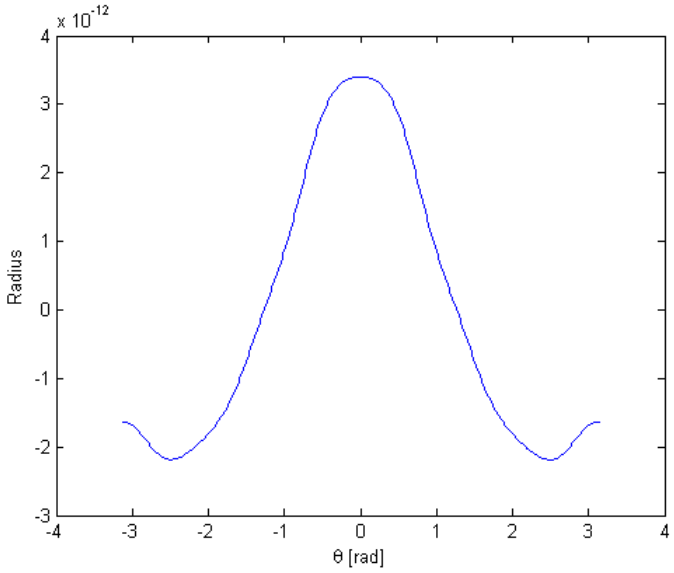

Figure 3.2.13: Relative error for pear shape

3.2.4 Droplet shapes from computed pressure

The next step is to find the shape computing the curvature in terms of pressure, with data obtained from COMSOL simulations, Figure 2.2.13 and 2.2.14. Curvature in terms of pressure can be defined as

$$\kappa = \frac{p_i + p_d}{\gamma}, \tag{3.2.3}$$

where k is the curvature, p_i the inside pressure and p_d a pressure difference between the COMSOL pressure and its average.

An important aspect to analyze is how we can compute the area of the bubble. To compute the bubble's area we considered many points on the bubble for which we know their radius. We took two approaches to compute the bubble area.

First one by using Heron's formula. For that we computed the length of the three sides of a pie between two successive points on the circle and the origin.

With Heron's formula, which is used in geometry, we computed the area of a triangle, with the lengths of the sides a, b and c

$$A = \sqrt{s(s-a)(s-b)(s-c)},$$

where s is for the semi-perimeter of the triangle

$$s = \frac{a+b+c}{2}.$$

The length of the side a is the distance between the first point and the origin, which is simply the radius. For the b side, the distance between the second point and the origin is considered; it is simply the radius of the next point. Note that we take the points around the circle counterclockwise. The third side, which is c, will be computed by the formula of the distance between two successive points

$$d_{AB} = \sqrt{(x_B - x_A)^2 + (y_B - y_A)^2}.$$

The same is for all triangles, which will give the bubble area by summing them.

The second method to calculate the bubble area is by using Green's theorem, which computes the area by a line integral. So, the area can be calculated by the contour integral

$$A = \frac{1}{2}\oint(-ydx + xdy). \tag{3.2.4}$$

Here x and y are the mid points of each linepiece between successive points.

The discretized form of (3.2.4) is

$$A = \frac{1}{2}\sum_i(-\bar{y}_i\Delta x_i + \bar{x}_i\Delta y_i), \tag{3.2.5}$$

with $\bar{x}_i = \frac{1}{2}(x_{i+1} + x_i)$, $\Delta x_i = x_{i+1} - x_i$ and $\bar{y}_i = \frac{1}{2}(y_{i+1} + y_i)$, $\Delta y_i = y_{i+1} - y_i$.

Note that for both ways to calculate the bubble area the values of ϑ have to be ascending.

We checked these methods by considering the bubble being a circle, and compared it to the area of a circle ($A = \pi R^2$). The methods are quite accurate, because the error is really small.

The bubble shape is not always a simple shape like a circle; there can be more complicated shapes. For that we will check if the methods used to find the bubble area also work for a "C" shape, shown in Figure 3.2.14. The area of this shape is $A = 0.75(\pi R_o^2 - \pi R_i^2)$, where R_o is radius of the exterior circle and R_i is the radius of the interior circle . The relative error between the method that uses Heron's formula is

$err = 0.666$ as for the second method, which uses Green's formula, the error is much smaller, $err = 3.7758e - 004$. In this case we can say that for a complex shape, the method using Green's theorem is much more accurate.

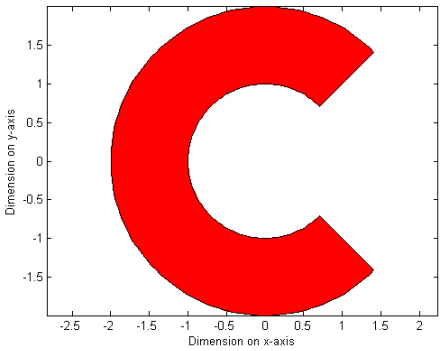

Figure 3.2.14: "C" shape

We compute the droplet shape with data from all four cases simulated with COMSOL, in 2.2.13 and 2.2.14.

3.2.4.1 Case 1

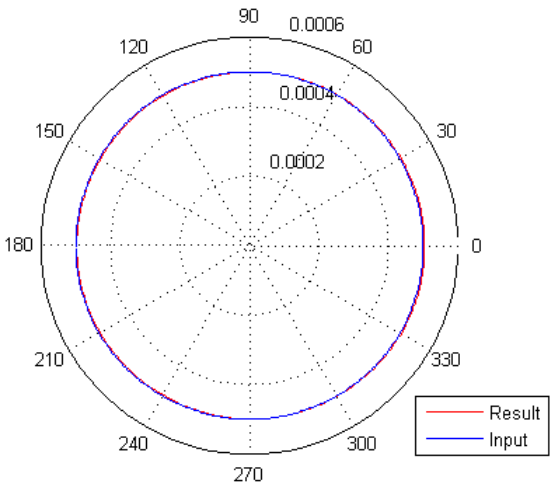

Figure 3.2.15: Bubble shape

For a droplet with the radius of r =0.5 mm and the velocity of v =1 m/s, the shape of the droplet will become as in Figure 3.2.15.

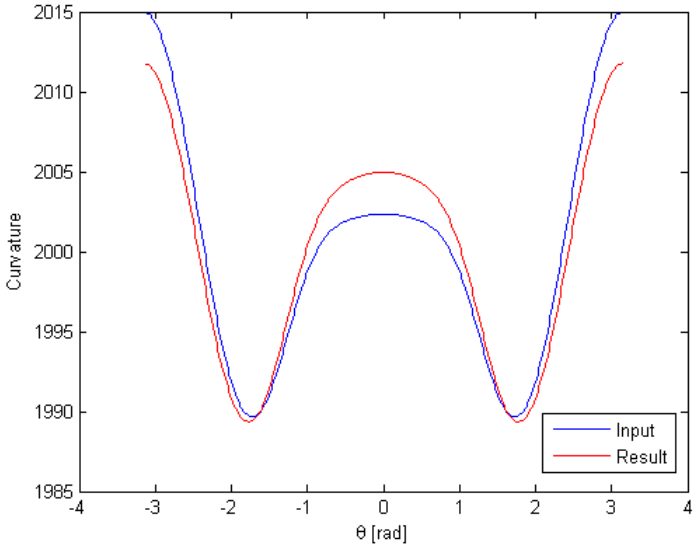

Figure 3.2.16: Curvature of the bubble in Figure 3.2.15

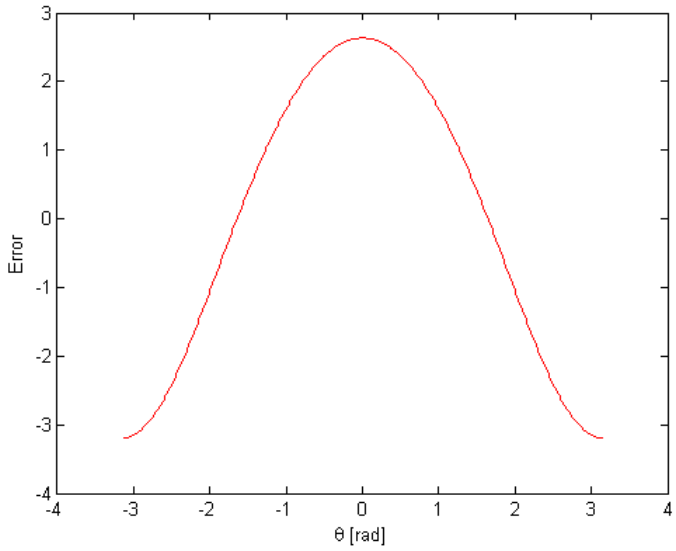

Figure 3.2.17: Error between curvatures in Figure 3.2.16

Note that the shape was not affected too much. This means that for very small droplets

with small velocity, the shape remains circular. The curvature was computed with the central differences method. The accuracy of the method is not bad, due to the fact that the curvature is similar to the one used as an input (Figure 3.2.16). Only a small error appears between them (Figure 3.2.17).

3.2.4.2 Case 2

Considering the same droplet with r =0.5 mm but higher velocity v =10 m/s, the shape of the droplet is deformed from the circular shape as shown in Figure 3.2.15.

This means that the higher velocity influences the pressure acting over the droplet and leads to a deformed shape.

The curvature finding method (central differences method) works better in this case, because the curvature is almost the same as the initial one (Figure 3.2.16, the curvatures are overlapping), however with a very small error (Figure 3.2.17). Note that the area decreased by 20%.

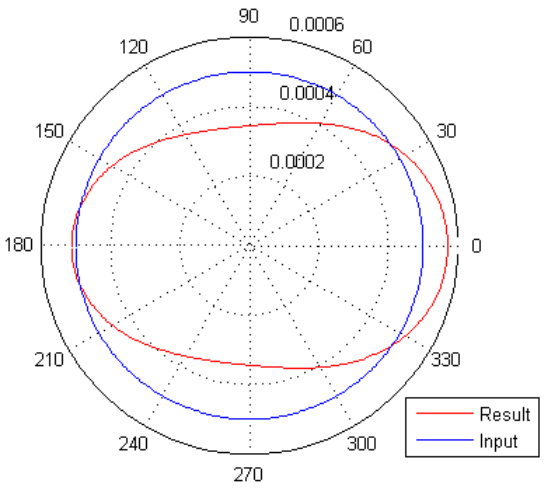

Figure 3.2.18: Bubble shape

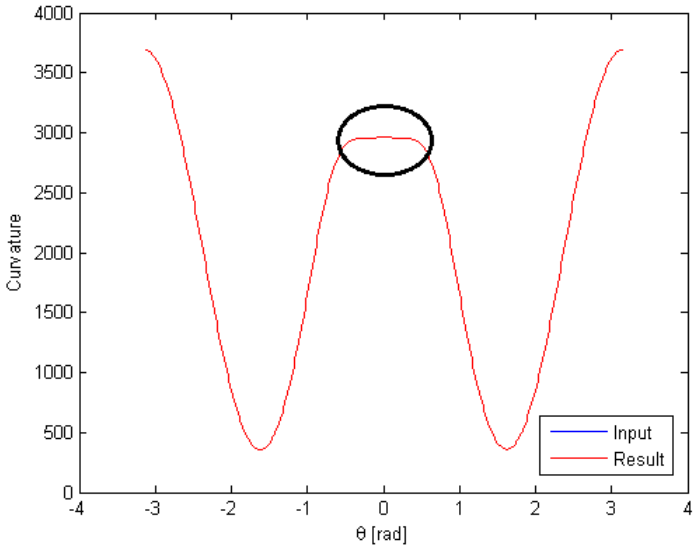

Figure 3.2.19: Curvature of the bubble in Figure 3.2.18

In Figure 3.2.16, there is a flat area marked with a black ellipse. This flat part, can be explained by looking to Figure (2.2.14) 2c, where around $\theta = 0$ the pressure distribution is constant, so the surface tension minimize the surface area by making it as circular as possible.

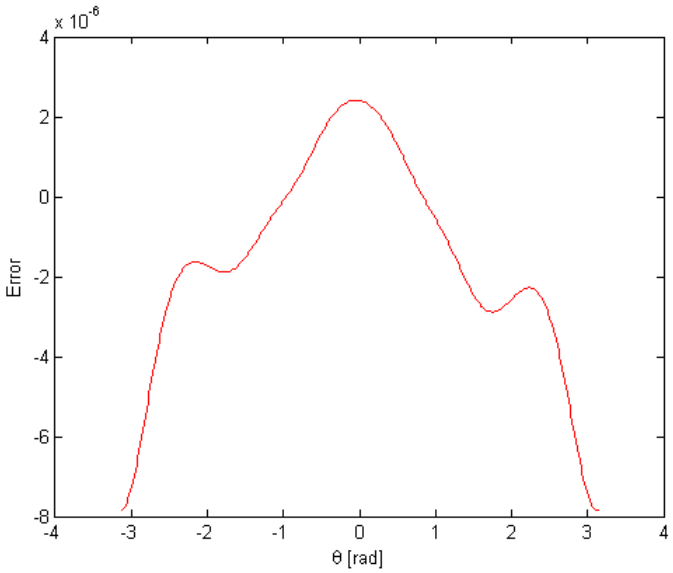

Figure 3.2.20: Error between curvatures in Figure3.2.19

3.2.4.3 Case 3

Assume now that the droplet has a radius of r =2 mm and a velocity of v =1 m/s.

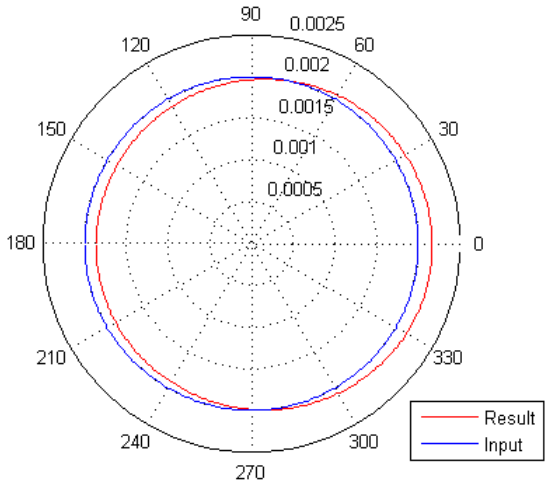

Figure 3.2.21: Bubble shape

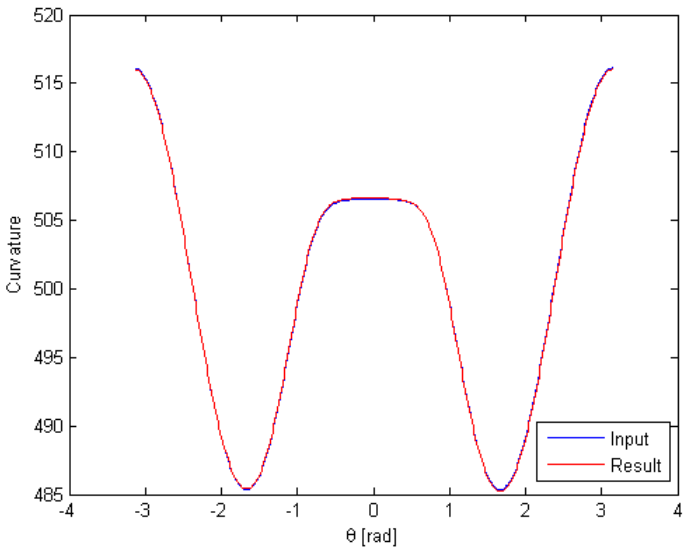

Figure 3.2.22: Curvature of the bubble in Figure 3.2.21

The shape of the droplet will became as in Figure 3.2.21, without significant deformations. The method used for computing the curvature is the central differences, and as Figure 3.2.23 shows, the error is small, so the result is quite accurate.

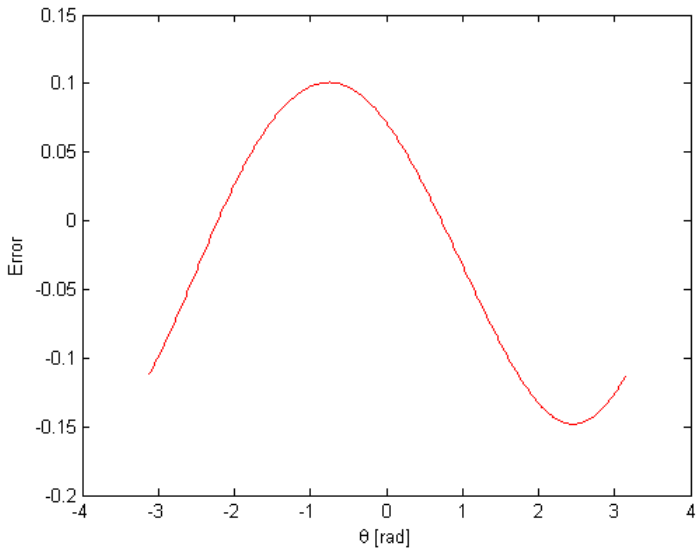

Figure 3.2.23: Error between curvatures in Figure3.2.22

3.2.4.4 Case 4

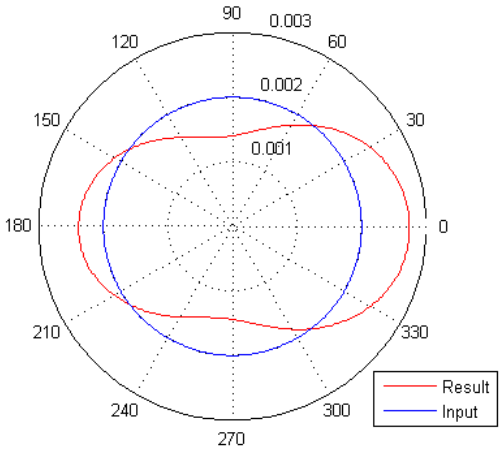

Figure 3.2.24: Bubble shape

For a droplet with a radius of r =2 mm and a velocity of v =10 m/s, the shape of the droplet will deform from circular to a more flatter one, as shown in Figure 3.2.24.

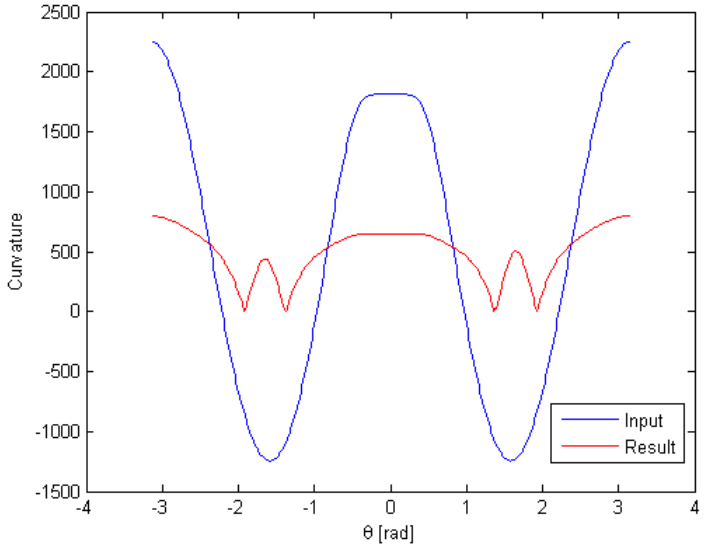

Figure 3.2.25: Curvature of the bubble in Figure

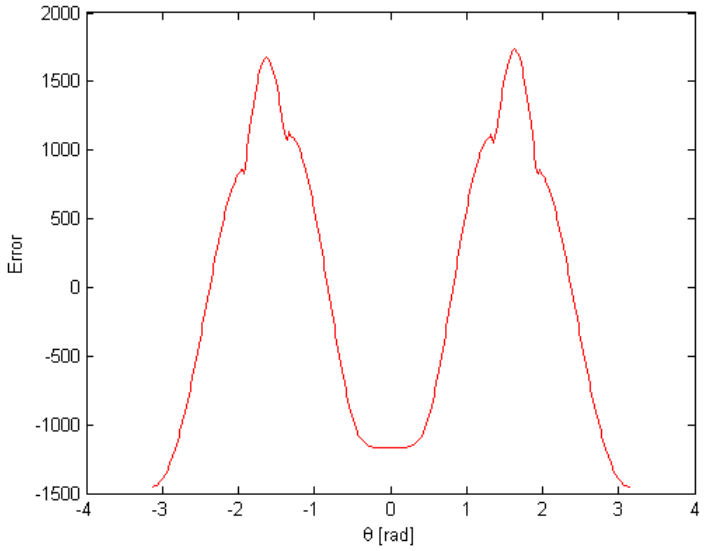

Figure 3.2.26: Error between curvatures in Figure 3.2.25

The representation of the curvature in Figure 3.2.25, shows the difference between the

initial curvature (3.2.3) and the computed one. In Figure 3.2.26 it can be seen that the error is very big, so first method, circle fit using three points did not gave accurate results.

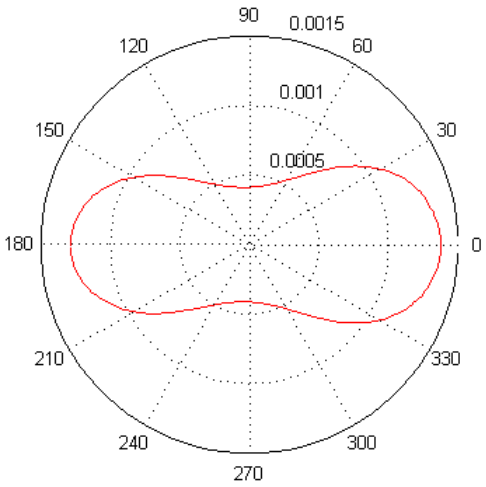

Figure 3.2.27: Bubble shape

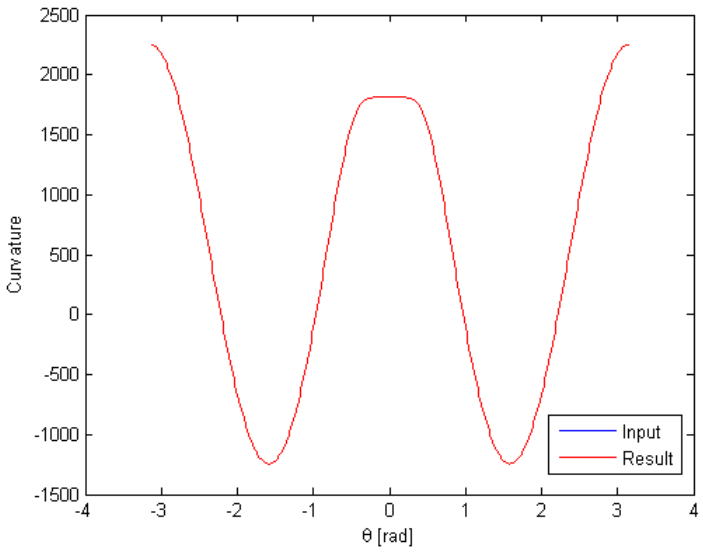

Figure 3.2.28: Curvature of the bubble in Figure

In order to obtain a more accurate solution, we used the second method, to compute the curvature, with derivatives. In this case, the result of the curvature is more accurate as we can see in Figure 3.2.29 that the shape is more appropriate to the real one. Note that the area of the deformed droplet decreased by 24% compared to the initial.

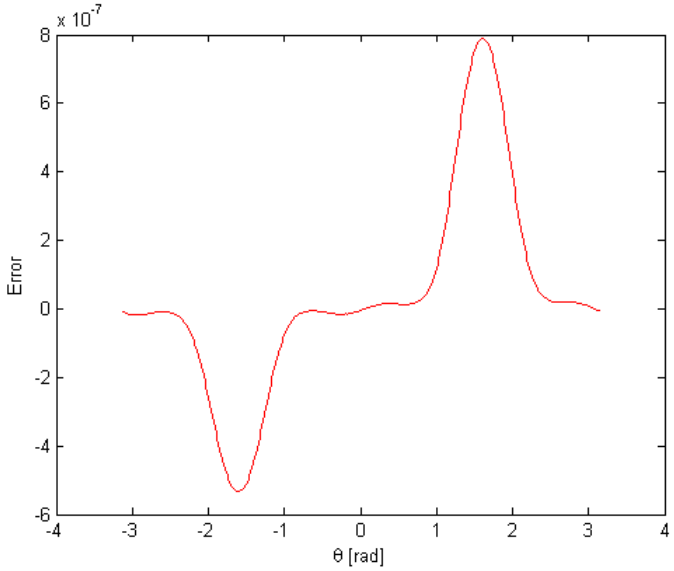

Figure 3.2.29: Error between curvatures in Figure 3.2.28

Comparing the second case with the third case, we conclude that the velocity affects the shape of the bubble, increasing the deformation with the magnitude of the velocity.

3.2.5 Raising bubble shape

Before we have seen how the method behaves for computing the curvature in terms of pressure, obtained from COMSOL simulations. Further, we computed the curvature by using central differences, with radii taken from a simulation in COMSOL.

For the simulation we assume a case of a two-phase laminar flow. This means that for a “smooth" flow in parallel layers, we have a liquid (honey) and a gas (air), which are immiscible. In this case the fluid is incompressible, thus the density is constant. We consider a bubble of air, with the following properties: density $\rho_a = 1\,\mathrm{kg/m^3}$ and viscosity of $\mu_a = 1.81 \times 10^{-5}\mathrm{Pa\,s}$, placed in a container with honey, of density $\rho_h = 1420\,\mathrm{kg/m^3}$ and viscosity of $\mu_h = 2\mathrm{Pa\,s}$. We chose honey instead of water, because it has a higher viscosity.

From literature [4], we know that smaller droplets have a spherical shape. The bigger they get the more their shape deviates from the sphere. As we want to obtain a

deformed shape, we have to choose carefully the radius of the droplet. For that we will use the Eötvös number, a dimensionless number

$$Eo = \frac{\Delta\rho g L^2}{\gamma},$$

where $\Delta\rho$ is the difference in density of two phases (kg/m^3), $g = 9.81$m/s^2 is gravity, L is the characteristic length, in this case the diameter of the bubble (m), and γ is the surface tension (N/m). For a low Eo (less than one), surface tension dominates, as for a high Eo the system is relatively unaffected by surface tension effects.

The internal pressure of the droplet is considered to be

$$p_i = \frac{\gamma}{R}.$$

As for the background pressure level, it is described in Figure 3.2.30.

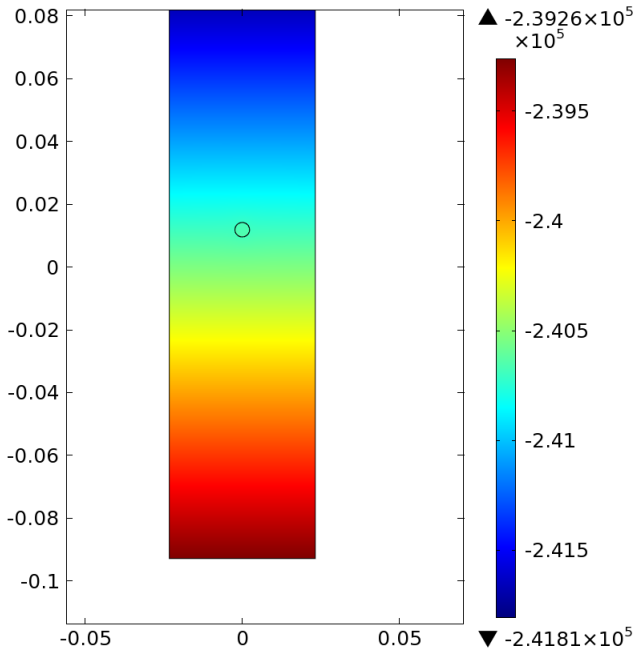

Figure 3.2.30: Pressure in container

Due to the fact that we simulate a raising bubble, we considered also a volume force vertically

$$F = -\rho g,$$

where ρ is density and g is the gravitational field.

Having all necessary parameters, we can simulate a raising bubble. For a small Eötvös number $Eo = 1$ the result was the expected one; a spherical bubble, with the shape relatively unaffected. It is clear that surface tension dominates, and keeps the shape as spherical as possible.

Increasing the Eötvös number to $Eo = 10$, the effects of surface tension decreased, and the shape deformed in time, as it is visible in Figure 3.2.31 a.

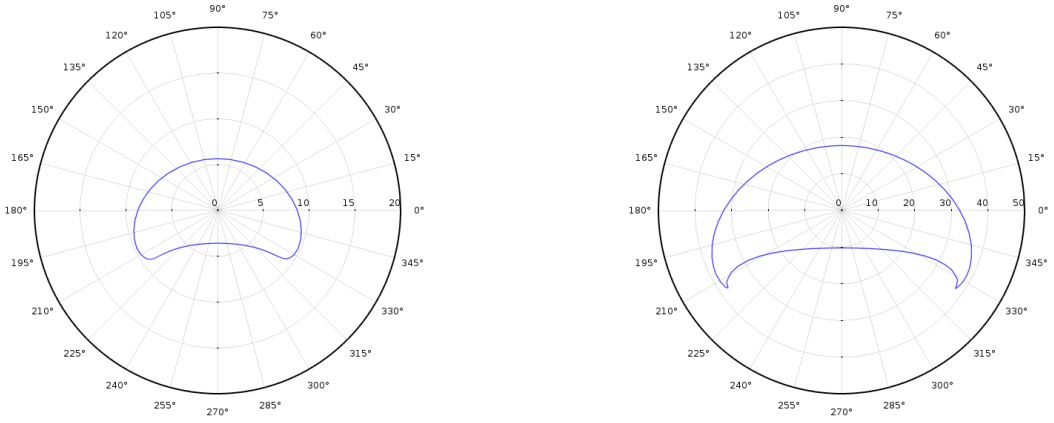

(a) $Eo = 10$ (b) $Eo = 100$

Figure 3.2.31: Bubble shape

For a much higher Eötvös number $Eo = 100$, the shape is similar to the previous one, but it became much sharper then before. In Figure 3.2.31 b, this happens because surface tension is lower and the attraction forces are not so strong. Hence forces do not minimize the bubble's surface area as much as before.

Considering the shape of a bubble (Figure 3.2.32) obtained at a random time in the rising process for $Eo = 10$, we introduced the radius function of that shape into our minimization method.

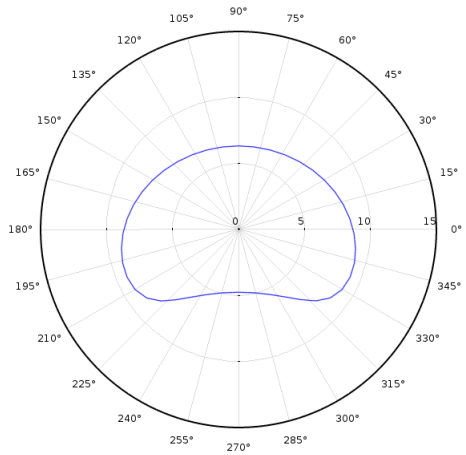

Figure 3.2.32: Bubble shape

Starting with an input spherical bubble of radius $r = 8$, we obtained again the bubble shape computed from COMSOL (Figure 3.2.33). It is the same as in Figure 3.2.32, because the error between the solution curvature and the initial one is very small as shown in Figure 3.2.35. Therefore, the minimization method performs well at computing the shape of a droplet given an arbitrary input for the radius.

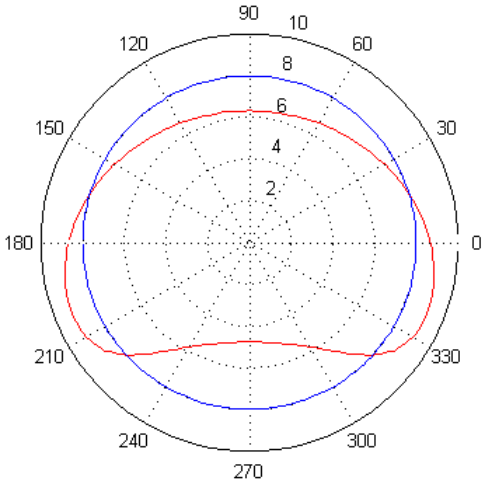

Figure 3.2.33: Bubble shape with minimizaiton method

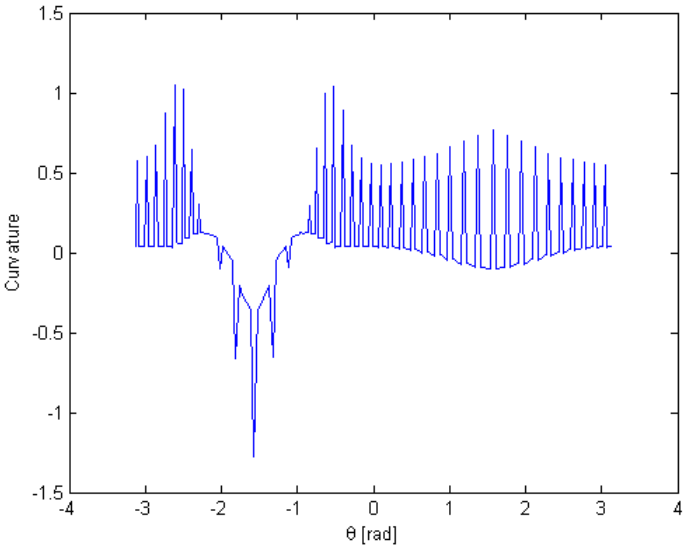

Figure 3.2.34: Curvature of 3.2.33

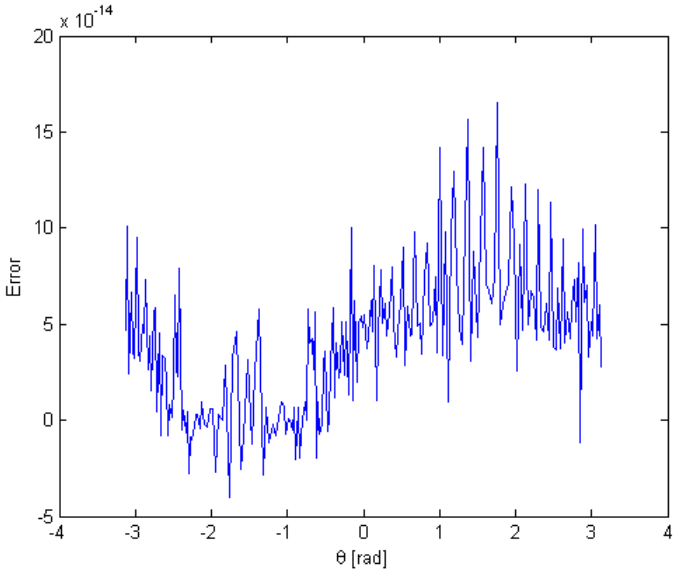

Figure 3.2.35: Error of the curvatures

4 Smoothed Particle Hydrodynamics

Within CASA[1] a broad interest in particle methods has developed over the past years, with applications ranging from crowd management [7] to hypervelocity impacts [34, 35]. Our effort to include surface tension into SPH will pinpoint on the later research.

The debris, Figure 4.0.1, shooting out after an impact has many phases: solid, liquid, gas, plasma. It has been shown that demolition of the direct impact zone and the shape of the plume are predicted very accurately, but secondary impacts can be mispredicted as the shape of the debris is lost in the cloud. Inclusion of surface tension effect will later hopefully bring improvements to this.

We start this chapter with a general introduction to SPH, explaining the method and its character. In the second section we have a broad look at flows and how to come to a simple formulation. In the third section we explore three different approaches to treat surface tension. We then discuss the actual implementation and end with showing results.

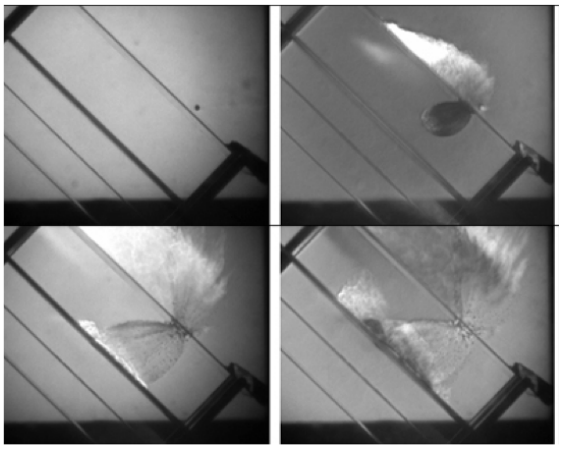

Figure 4.0.1: Hypervelocity impact [European Space Agency]

[1]Centre for Analysis, Scientific computing and Applications (CASA) combines all activities related to analysis at the Department of Mathematics and Computer Science of Eindhoven University of Technology (TU/e). Its major research objective is to develop new and improve existing mathematical (both analytical and numerical) methods for a wide range of applications in science and engineering.

4.1 General formulation

Smoothed Particle Hydrodynamics (SPH) is a meshfree, Lagrangian, particle method, invented independently by Gingold and Monaghan (1977) and Lucy (1977) for astrophysical problems. After that it was extended to other fields, as fluid and solid mechanics. It was developed because an easy method to work with was needed and at the same time to give good accuracy. A fluid is considered to be a hard phenomenon to simulate in a realistic way and SPH has proven to perform well at doing that [22, 26].

The SPH method replaces the continuous media with a set of particles. This can be interpreted in two ways. In a physicist's way, SPH particles are material particles and one can work with them like any other particle system. In a mathematical formulation, particles are interpolation points and fluid properties can be calculated from them.

Properties of the SPH method are: stability, accuracy and adaptivity. Complying with all three makes the method a good tool for engineering applications. The adaptability of the SPH approximation helps when we have to deal with particle distributions in an arbitrary way, because the SPH formulation is not affected. The SPH particles carry material properties with them, which means that SPH is a good combination between Lagrangian and particle method and they interact with each other within the range given by a smoothing function.

Usually the governing equations are partial differential equations (PDEs) and using the SPH method of discretization helps a lot, because PDEs are becoming ordinary differential equations (ODEs) with respect to time, and it is much easier to deal with them, with less computational costs. Numerical results can be found for different fields, like density, pressure, velocity.

To obtain an SPH formulation there are two steps, two approximations to be made: the kernel approximation and the particle approximation.

The first step consists in representing a function and its derivatives in continuous form as integral representation. An integral representation or a kernel approximation of a function $f(x)$ used in SPH should look like

$$< f(x) >= \int_{\Omega} f(x')\delta(x - x')dx', \tag{4.1.1}$$

where f is a function of the position vector x, and $\delta(x - x')$ is the Dirac distribution, defined as

$$\delta(x - x') = \begin{cases} 1 & x = x' \\ 0 & x \neq x' \end{cases}.$$

In (4.1.1), Ω is the support (fluid domain) of the point x - the domain of integration. Using Dirac's distribution the integral representation is exact, but only for $f(x)$ which

is defined and continuous in Ω. The elementary volume surrounding the point at x' located in the neighborhood of the point at x, is notated with dx'.

If the Dirac distribution $\delta(x - x')$ is replaced by a smoothing function $W(x - x', h)$, the integral representation of $f(x)$ is given by

$$< f(x) >:= \int_{\Omega} f(x')W(x - x', h)dx', \tag{4.1.2}$$

where W is the smoothing kernel or kernel function. In the smoothing kernel, h is called the smoothing length, defining the radius of influence of the smoothing function W. If the smoothing function W is not the Dirac function, the integral representation can only be an approximation. This is why it is called the kernel approximation.

The kernel approximation of the spatial derivative $\nabla \cdot f(x)$ is obtained by the formula

$$< \nabla \cdot f(x) > \approx \int_{\Omega} [\nabla \cdot f(x')]W(x - x', h)dx',$$

which gives

$$< \nabla \cdot f(x) > \approx - \int_{\Omega} f(x') \cdot \nabla W(x - x', h)dx'. \tag{4.1.3}$$

The kernel function W determines the accuracy of function approximation, while the kernel gradient determines the approximation accuracy of the first and second derivatives. In order to obtain good accuracy, the kernel and the gradient have to be chosen properly. As Monaghan said [26], it is always good to assume that the kernel is a Gaussian, if you want to find a physical interpretation of an SPH equation. Monaghan called this *the first golden rule of SPH*.

The Gaussian kernel function is adequately smooth even for higher order derivatives and provides stable and accurate results even for random particles distributions. The Gaussian function is defined by

$$W(R, h) \quad = \quad \alpha e^{-R^2},$$

where R is the relative distance between two particles, located at points x and x', defined as $R = \frac{r}{h} = \frac{|x-x'|}{h}$, where r is the distance between the location of the two particles. In order to formulate the 1D, 2D and 3D of the Gaussian kernel, α should be replaced by $\frac{1}{h\sqrt{\pi}}$, $\frac{1}{\pi h^2}$ and $\frac{1}{\sqrt[3]{\pi}h^3}$.

The angle brackets $<>$ are used in (4.1.1) and (4.1.2) denote the *kernel approximation*.

The W smoothing function should satisfy a set of *conditions*:

(i) The first one is the *normalization* condition of the kernel that states

$$\int_{\Omega} W\left(x - x', h\right) dx' \quad = \quad 1.$$

This condition is called also the unity condition, since the integration of the smoothing function produces the unity. This property assures that a constant function is reproduced exactly.

(ii) The second condition is the *positivity* condition

$$W(x - x', h) \quad \geq \quad 0,$$

for any point at x' within the support domain of the particle at point x. This property assures that the smoothing function is non-negative in the support domain. If it is not satisfied, it is possible to get non-physical quantities, like negative density or negative energy.

(iii) The third condition is the *compact support* condition

$$W(x - x', h) \quad = \quad 0 \quad when \quad | \, x - x' \, | > kh,$$

where kh is the radius of kernel support. Using this condition, integration over the entire problem domain is localized as integration over the support domain of the smoothing function. Thus, the integration domain Ω can be, and usually is the same as the support domain. In other words, the particle b has no effect on particle a if it is beyond a certain distance.

(iv) The fourth condition is the *symmetry* property. This condition assures that different particles, located at the same distance but different position, should have equal effect on a specific particle.

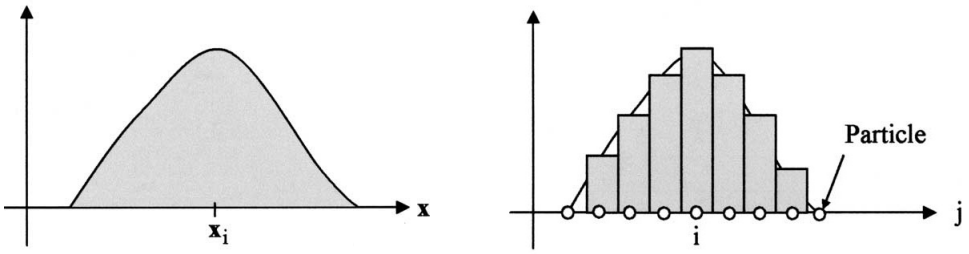

Figure 4.1.1: The discretization process of the continuous form (particle representation) [13]

The SPH kernel approximation can be converted into discretized forms of summation over all the particles in the support domain. This process of summation over the particles is commonly known as particle approximation in the SPH literature and it is the second step in the SPH method (see Figure 4.1.1). Another 2D visualization of the

distribution of particles over the Ω support domain with a surface S is represented in Figure 4.1.2. There W is a smoothing function that is used to approximate the field variables at particle i using averaged summations over particles j within the support domain with radius of kh.

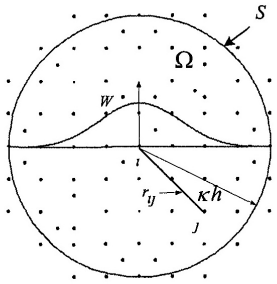

Figure 4.1.2: Particle approximation. Particles are being within the support domain of the smoothing function W for particle i.

The continuous SPH integral representation for $f(x)$ can be written in the following form of discretized particle approximation

$$< f(x) >= \sum_{j=1}^{N} f(x_j) W(x - x_j, h) dV_j, \tag{4.1.4}$$

where N is the number of particles within the support domain of particle j. We replaced the elementary volume dx' at the location j with the finite volume of the particle dV_j that is related to the mass of the particles $m_j = dV_j \rho_j$, where ρ_j is the density of particle j, and j can take values from 1 to N. Therefore, substituting dV_j in the equation (4.1.4), a new formulation of the particle approximation can be written as

$$< f(x) >= \sum_{j=1}^{N} \frac{m_j}{\rho_j} f(x_j) W(x - x_j, h).$$

A very important observation has to be made here. In the particle approximation step two new magnitudes appear, mass and density. This is important for our purpose, because density is a variable in problems of fluid dynamics.

The particle approximation for a function at particle i, has the form

$$< f(x_i) >= \sum_{j=1}^{N} \frac{m_j}{\rho_j} f(x_j) W_{ij},$$

where $W_{ij} = W(x_i - x_j, h)$. The equation states that the value of a function at a particle i, is approximated using the values of all particles in the support domain of that particle i, weighted by the smoothing function.

The particle approximation of a derivative for a particle i has the following form

$$< \nabla \cdot f(x_i) >= -\sum_{j=1}^{N} \frac{m_j}{\rho_j} f(x_j) \cdot \nabla W_{ij}, \tag{4.1.5}$$

which is the discretized form of equation (4.1.3), a summation over a set of particles.

Using those two steps one can derive SPH formulations for partial differential equations. Some equations for divergence of $f(x)$ at particle i are described in the paper of Liu&Liu[23]:

$$< \nabla \cdot f(x_i) >= \frac{1}{\rho_i} \left[\sum_{j=1}^{N} m_j \left[f(x_j) - f(x_i) \right] \cdot \nabla_i W_{ij} \right] \tag{4.1.6}$$

and

$$< \nabla \cdot f(x_i) >= \rho_i \left[\sum_{j=1}^{N} m_j \left[\left(\frac{f(x_j)}{\rho_j^2} \right) + \left(\frac{f(x_i)}{\rho_i^2} \right) \right] \cdot \nabla_i W_{ij} \right] \tag{4.1.7}$$

There are some rules for operators, that can be used for complex system equations. Considering two arbitrary functions of field variables f_1 and f_2, the following rules can be applied.

The sum, difference and product of two SPH approximations is equal to the sum, difference, product of the individual functions.

$$< f_1 \pm f_2 >=< f_1 > \pm < f_2 >,$$

$$< f_1 f_2 >=< f_1 >< f_2 > .$$

If the function f_1 is a constant, notated by c, the following equality takes place

$$< c f_2 >= c < f_2 > .$$

The SPH approximation operator is a linear one, so the SPH approximation operator is a commutative one, as illustrated

$$< f_1 + f_2 >=< f_2 + f_1 >$$

and

$$< f_1 f_2 >=< f_2 f_1 >$$

4.2 Flows in SPH

An attractive, illustrative application of surface tension computations is, as we have seen in Chapter 2, the modeling of falling raindrops. From a flow point of view, that is quite a complicated application, however: raindrops fall at a high velocity and the wake behind a rain droplet contains very fine vortices that are hard to simulate. For our purposes we want a simpler flow. We start by outlying the Navier-Stokes equations, then show the inviscid Euler equations. Finally, we make a viscous flow by studying a flow between two plates: Hele-Shaw flow, where the diffusion scales with the velocity rather than its second derivative.

4.2.1 Navier-Stokes equations

The Navier-Stokes equations describe the motion of a fluid. The physical quantities that are involved are the velocity u, density ρ and pressure p. These equations of the fluid, are considered to describe continuous substance, not discrete particles.

The governing equations of fluid dynamics are following the three laws of conservation, as Liu presented in [23] :

- *Mass conservation*

$$\frac{D\rho}{Dt} = -\rho \frac{\partial u^\beta}{\partial x^\beta}. \tag{4.2.1}$$

- *Momentum conservation*

$$\frac{Du^\alpha}{Dt} = \frac{1}{\rho}\frac{\partial \sigma^{\alpha\beta}}{\partial x^\beta} + F. \tag{4.2.2}$$

In these equations, the Greek superscripts α, β are introduced to denote the coordinate directions ($2D : \alpha, \beta = 1,2$; $3D : \alpha, \beta = 1,2,3$). Repetition of these indexes indicates summation in the equation. The scalar density is notated with ρ, e represents internal energy, u^α indicates the velocity, $\sigma^{\alpha\beta}$ is the total stress tensor, F is the external forces (eg. gravity, surface tension, viscosity, pressure), t is for time and the spatial coordinates are notated with x^α.

The total stress tensor $\sigma^{\alpha\beta}$ is composed by two elements, one is the isotropic pressure[2] and one is the viscous stress:

$$\sigma^{\alpha\beta} = -p\delta^{\alpha\beta} + \tau^{\alpha\beta},$$

where $\delta^{\alpha\beta}$ is the Kronecker delta and the viscous stress is $\tau^{\alpha\beta} = \mu\varepsilon^{\alpha\beta}$.

The definition of Kronecker's tensor:

$$\delta^{\alpha\beta} = \begin{cases} 1, & if\ \alpha = \beta \\ 0, & if\ \alpha \neq \beta \end{cases} .$$

The connection between the shear stress $\tau^{\alpha\beta}$ and the viscous shear strain rate $\varepsilon^{\alpha\beta}$, where μ is the dynamic viscosity is that they have to be proportional, for a Newtonian fluid.

$$\varepsilon^{\alpha\beta} = \left(\frac{\partial u^{\beta}}{\partial x^{\alpha}} + \frac{\partial u^{\alpha}}{\partial x^{\beta}}\right) - \frac{2}{3}\left(\nabla \cdot u\right)\delta^{\alpha\beta}.$$

The shear strain rate is used for compressible Newtonian fluid. It is composed by two elements , the deformation velocity tensor and dilatation. If the fluid is incompressible the second part is zero.

Further, we consider frictionless flow, so the viscous stress will be zero.

4.2.2 Euler equations

4.2.2.1 General Euler equations

We obtain the Euler equations for fluid, by rewriting the Navier-Stokes equations (4.2.1), (4.2.2) and (**??**), and replacing the total stress tensor, with the isotropic pressure $\sigma^{\alpha\beta} = -p\delta^{\alpha\beta}$. Neglecting the viscous term from Navier-Stokes, we get the Euler equations for frictionless flow.

- *Mass conservation*

$$\frac{D\rho}{Dt} = -\rho\frac{Du^{\alpha}}{Dx^{\alpha}}. \tag{4.2.3}$$

- *Momentum conservation*

$$\frac{Du^{\alpha}}{Dt} = \frac{1}{\rho}\frac{-p}{Dx^{\alpha}}. \tag{4.2.4}$$

[2]isotropic pressure, is the pressure on a fluid at rest; it acts with equal magnitude in all directions

Notations and conventions used for the Navier-Stokes equations hold here as well. Euler's equations are obtained from the equations of motion assuming a frictionless flow. In a frictionless flow there can be no shear stress present, the surface forces are due to pressure.

4.2.2.2 Euler equations approximated with SPH

The governing fluid dynamics equations are recalled and their numerical discretization in the SPH particle approximation is illustrated.

The process of numerical discretization involves the approximation of functions, derivatives and integrals at a particle by using the information taken from all its neighbours, which are the surrounding particles that exert an influence on it.

A general SPH particle approximation of a function f at a particle i , can be written in the discretized form of a summation of the neighbouring particles as

$$< f_i >= \sum_{j=1}^{N} f_j W_{ij} dV_j,$$

where the smoothing function $W_{ij} = W\left(x_i - x_j, h\right)$; here h is the smoothing length, which establish the area of influence of the function W. We think of particles as balls of material having volume $dV_j = m_j/\rho_j$, where m is the mass and ρ is the density.

We will see further that different forms of equations can be used to describe the fluid flows, depending on the specific circumstances.

SPH Mass conservation The density determines the particle distribution and the smoothing length evolution. The mass of the fluid is unchanged regardless of its state of motion.

When considering an incompressible flow, the time rate of change of mass when following a material fluid particle should be zero ($\frac{D\rho}{Dt} = 0$).

In order to approximate the density, we will apply the SPH approximation to the velocity part of equation (4.2.3)

$$\frac{D\rho_i}{Dt} = -\rho_i \sum_{j=1}^{N} u_j^{\alpha} \frac{\partial W_{ij}}{\partial x_i^{\alpha}} dV_j. \tag{4.2.5}$$

The particle approximation of the gradient of unity

$$\nabla 1 = \int 1 \cdot \nabla W(x - x', h) dx'$$

$$= \sum_{j=1}^{N} \frac{\partial W_{ij}}{\partial x_i^{\alpha}} dV_j = 0,$$

can be written also as

$$\rho_i \sum_{j=1}^{N} u_i^\alpha \frac{\partial W_{ij}}{\partial x_i^\alpha} dV_j = \rho_i u_i^\alpha \underbrace{\left(\sum_{j=1}^{N} \frac{\partial W_{ij}}{\partial x_i^\alpha} dV_j \right)}_{0}. \tag{4.2.6}$$

The RHS part is equal to zero.

Next, we will add the RHS part from equation (4.2.5) with the RHS part of the equation (4.2.6), like Liu has done in his work [23], and we will get:

$$\frac{D\rho_i}{Dt} = \rho_i \sum_{j=1}^{N} u_{ij}^\alpha \frac{\partial W_{ij}}{\partial x_i^\alpha} dV_j, \tag{4.2.7}$$

where $u_{ij}^\alpha = (u_i^\alpha - u_j^\alpha)$. This equation is another SPH formulation, but it introduces velocity difference into discrete particle approximation.

Another SPH formulation for mass conservation, also with velocity difference, can be obtained, by applying the following formulation, to place the density inside the gradient operator

$$-\rho \frac{Du^\alpha}{Dx^\alpha} = -\left(\frac{D\left(\rho u^\alpha\right)}{Dx^\alpha} - u^\alpha \cdot \frac{D\rho}{Dx^\alpha} \right).$$

Applying particle approximation, we have

$$-\rho \frac{Du^\alpha}{Dx^\alpha} = -\sum_{j=1}^{N} \rho_j u_j^\alpha \frac{\partial W_{ij}}{\partial x_i^\alpha} dV_j + \sum_{j=1}^{N} \rho_j u_i^\alpha \frac{\partial W_{ij}}{\partial x_i^\alpha} dV_j,$$

$$\frac{D\rho}{Dt} = -\sum_{j=1}^{N} \rho_j \frac{m_j}{\rho_j} u_j^\alpha \frac{\partial W_{ij}}{\partial x_i^\alpha} + \sum_{j=1}^{N} \rho_j \frac{m_j}{\rho_j} u_i^\alpha \frac{\partial W_{ij}}{\partial x_i^\alpha},$$

$$\frac{D\rho}{Dt} = \sum_{j=1}^{N} m_j u_{ij}^\alpha \frac{\partial W_{ij}}{\partial x_i^\alpha}. \tag{4.2.8}$$

What we can observe is that the time rate of the density of a particle is in a relationship with the relative velocities between this particle and all the neighbouring particles in the support domain. The approximation in (4.2.8) is written in vector notation, $u_{ij} = \left(u_i^\alpha - u_j^\alpha\right)$. This relative velocity is beneficial at reducing errors from particle inconsistency[3].

[3]The particle inconsistency is the discrepancy between the spatially discretized equations and the corresponding kernel approximations in continuous form.

SPH Momentum conservation In order to discretize the momentum equation, we will apply the SPH particle approximation to equation (4.2.4) :

$$\frac{Du_i^\alpha}{Dt} = \frac{1}{\rho_i}\sum_{j=1}^{N} -p_j \frac{\partial W_{ij}}{\partial x_i^\alpha} dV_j. \tag{4.2.9}$$

Rewriting the particle approximation of the gradient of unity, we have that

$$\frac{1}{\rho_i}\sum_{j=1}^{N} -p_i \frac{\partial W_{ij}}{\partial x_i^\alpha} dV_j = -\frac{p_i}{\rho_i}\left(\sum_{j=1}^{N} \frac{\partial W_{ij}}{\partial x_i^\alpha} dV_j\right) = 0, \tag{4.2.10}$$

is zero, because the term in brackets is zero.

Considering the equation (4.2.9) and the equation (4.2.10), and adding the RHS part of both of them, leads to

$$\frac{Du_i^\alpha}{Dt} = -\sum_{j=1}^{N} m_j \frac{p_{i+}p_j}{\rho_i \rho_j} \frac{\partial W_{ij}}{\partial x_i^\alpha}. \tag{4.2.11}$$

This equation is important because it reduces errors that could come from particle inconsistency problem.

We can get to another formulation by considering the following

$$\frac{1}{\rho}\frac{-p}{Dx^\alpha} = \frac{D}{Dx^\alpha}\frac{-p}{\rho} + \frac{-p}{\rho^2}\frac{D\rho}{Dx^\alpha}.$$

Applying particle approximation to the gradient, we get:

$$\frac{Du_i^\alpha}{Dt} = \sum_{j=1}^{N} \frac{-p_j}{\rho_j}\frac{\partial W_{ij}}{\partial x_i^\alpha} dV_j - \frac{p_i}{\rho_i^2}\sum_{j=1}^{N} \rho_j \frac{\partial W_{ij}}{\partial x_i^\alpha} dV_j$$

$$= -\left(\sum_{j=1}^{N} \frac{p_i}{\rho_i^2} m_j \frac{\partial W_{ij}}{\partial x_i^\alpha} + \sum_{j=1}^{N} \frac{p_j}{\rho_j^2} m_j \frac{\partial W_{ij}}{\partial x_i^\alpha}\right),$$

$$\frac{Du_i^\alpha}{Dt} = -\sum_{j=1}^{N} \left(\frac{p_i}{\rho_i^2} + \frac{p_j}{\rho_j^2}\right) m_j \frac{\partial W_{ij}}{\partial x_i^\alpha}. \tag{4.2.12}$$

The conservation of momentum implies that the momentum remains constant; this means that momentum is not created or destroyed.

SPH formulation of Euler equations

Conservation of mass
$\frac{D\rho_i}{Dt} = -\rho_i \sum_{j=1}^{N} u_j^{\alpha} \frac{\partial W_{ij}}{\partial x_i^{\alpha}} dV_j$
$\frac{D\rho_i}{Dt} = \rho_i \sum_{j=1}^{N} u_{ij}^{\alpha} \frac{\partial W_{ij}}{\partial x_j^{\alpha}} dV_j$
$\frac{D\rho_i}{Dt} = \sum_{j=1}^{N} m_j u_{ij}^{\alpha} \frac{\partial W_{ij}}{\partial x_i^{\alpha}}$
Conservation of momentum
$\frac{Du_i^{\alpha}}{Dt} = -\sum_{j=1}^{N} m_j \frac{p_{i+}p_j}{\rho_i \rho_j} \frac{\partial W_{ij}}{\partial x_i^{\alpha}}$
$\frac{Du_i^{\alpha}}{Dt} = -\sum_{j=1}^{N} \left(\frac{p_i}{\rho_i^2} + \frac{p_j}{\rho_j^2} \right) m_j \frac{\partial W_{ij}}{\partial x_i^{\alpha}}$

4.2.2.3 2D Euler equations approximated with SPH

Taking in consideration Euler equations for mass, momentum and energy conservation, we can write a 2D SPH scheme for frictionless Euler flow.

From equation (4.2.7), the 2D SPH for the mass conservation leads to

$$\frac{D\rho_i}{Dt} = \rho_i \sum_{j=1}^{N} \left(u_{ij}^1 \frac{\partial W_{ij}}{\partial x_i^1} dV_j + u_{ij}^2 \frac{\partial W_{ij}}{\partial x_i^2} dV_j \right). \tag{4.2.13}$$

From equation (4.2.11), the 2D SPH formulation for momentum conservation gives rise to two equations

$$\frac{Du_i^1}{Dt} = -\sum_{j=1}^{N} m_j \frac{p_{i+}p_j}{\rho_i \rho_j} \frac{\partial W_{ij}}{\partial x_i^1}, \tag{4.2.14}$$

$$\frac{Du_i^2}{Dt} = -\sum_{j=1}^{N} m_j \frac{p_{i+}p_j}{\rho_i \rho_j} \frac{\partial W_{ij}}{\partial x_i^2}, \tag{4.2.15}$$

where the superscripts denote the coordinate direction.

In these equations the smoothing function is $W_{ij} = W\left(x_i - x_j, h\right)$, the velocities in two directions are $u_{ij}^1 = \left(u_i^1 - u_j^1\right)$ and $u_{ij}^2 = \left(u_i^2 - u_j^2\right)$, and the volume of the particle is $dV_j = m_j/\rho_j$.

4.2.3 Hele-Shaw flow

Further, we studied the Hele-Shaw flow, because we were interested in stationary solutions and we needed a flow with diffusion.

The flow defined by Hele-Shaw, is described as Stokes flow between two plates with a small gap between them. The plates are flat and parallel, and the channel between them is very small. A good reason to work with Hele-Shaw flow is that it provide us with an easily accessible model.

Almost any microscopic flow analysis, will start from Navier-Stokes equations. It would be an easier way to work with these equations if we simplify the equations, because it is difficult to compute and work with the second derivative diffusion term $\mu\nabla^2\mathbf{u}$. This term will be replaced by a simpler term $\frac{\mu}{H^2}\mathbf{u}$, resulting to an equation similar to Hele-Shaw equation, which is much easier to work with.

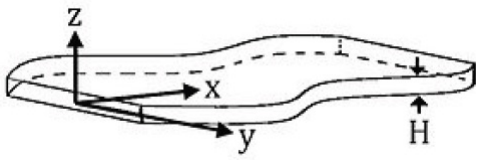

Figure 4.2.1: Hele Shaw scheme [source figure Amir Gat]

We will start with the Navier-Stokes equations, using tensor notation, representing mass and momentum conservation:

$$\frac{\partial \rho}{\partial t} + \frac{\partial}{\partial x_j}\left(\rho u_j\right) = 0, \tag{4.2.16}$$

$$\frac{\partial}{\partial t}\left(\rho u_i\right) + \frac{\partial}{\partial x_j}\left(\rho u_j u_i + p\delta_{ij} - \tau_{ij}\right) = f_i. \tag{4.2.17}$$

The notations used are ρ for density, u_i stand for the three speed components, x_i is used for the 3D spatial coordinates, p is the pressure and t represents the time. The Kronecker delta δ_{ij} is defined such that $\delta_{ij} = 1$ if $i = j$ and $\delta_{ij} = 0$ otherwise. Notated by τ_{ij} is a 3 x 3 stress tensor and by f_i is a body force.

We will consider the Poiseuille flow, pressure-induced flow, between two infinite parallel plates at a distance h. We assume that the medium is incompressible, so equation (4.2.16) becomes

$$\frac{\partial u_j}{\partial x_j} = 0, \tag{4.2.18}$$

which can be also written explicitly as

$$\frac{\partial u}{\partial x} + \frac{\partial v}{\partial y} + \frac{\partial w}{\partial z} = 0,$$

where u, v, w are the velocity components and x, y, z are the spatial coordinates.

For an incompressible flow, ρ does not change and its material derivative vanishes $\frac{D\rho}{Dt} = 0$.

Considering the reduce equation of the continuity equation (eq. 4.2.18), the expression for the strain will be also simplified to:

$$S_{ij} = \frac{1}{2}\left(\frac{\partial u_i}{\partial x_j} + \frac{\partial u_j}{\partial x_i}\right).$$

Making the simplifications also in the momentum equation (eq.4.2.17) and inserting the new formulation for strain, leads to

$$\rho u_j \frac{\partial u_i}{\partial x_j} = -\frac{\partial p}{\partial x_i} + \frac{\partial}{\partial x_j}\left(2\mu \frac{1}{2}\left(\frac{\partial u_i}{\partial x_j} + \frac{\partial u_j}{\partial x_i}\right)\right),$$

$$\rho u_j \frac{\partial u_i}{\partial x_j} = -\frac{\partial p}{\partial x_i} + \mu \frac{\partial^2 u_i}{\partial x_j^2} + \mu \frac{\partial}{\partial x_i}\frac{\partial u_j}{\partial x_j}.$$

In the previous formulation the last term of the RHS vanishes because of the equation (4.2.18), resulting a simpler expression of the momentum conservation

$$\rho u_j \frac{\partial u_i}{\partial x_j} = -\frac{\partial p}{\partial x_i} + \mu \frac{\partial^2 u_i}{\partial x_j^2}. \tag{4.2.19}$$

In this equation the rightmost term is difficult to compute so the idea is to replace it with a simpler term.

Further we will use the notations x for x_1, y for x_2, z for x_3, u for u_1, v for u_2 and w for u_3. The two plates stretch infinitely into the x and y directions, and the gap between them is in the z direction.

Assuming that the horizontal flow direction is into the x-direction, leads to

$$v = 0 \qquad \text{and} \qquad \frac{\partial}{\partial y} = 0.$$

The plates are infinitely large, so we are interested only in the fully developed flow, where the speed profile does not change anymore

$$\frac{\partial u}{\partial x} = \frac{\partial w}{\partial x} = 0.$$

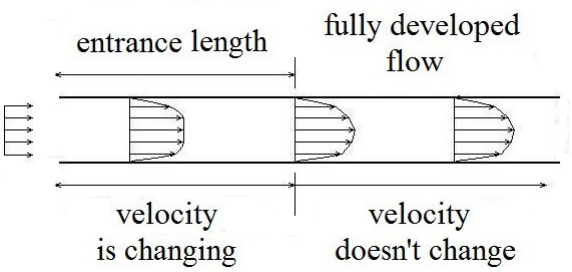

Figure 4.2.2: Fully developed flow

After we made the assumptions regarding the direction of the flow and the fact that the medium is incompressible, the system of equations will become

$$\frac{\partial u}{\partial x} + \frac{\partial w}{\partial z} = 0,$$

$$\rho u \frac{\partial u}{\partial x} + \rho w \frac{\partial u}{\partial z} = -\frac{\partial p}{\partial x} + \mu \left(\frac{\partial^2 u}{\partial x^2} + \frac{\partial^2 u}{\partial z^2} \right),$$

$$\rho u \frac{\partial w}{\partial x} + \rho w \frac{\partial w}{\partial z} = -\frac{\partial p}{\partial z} + \mu \left(\frac{\partial^2 w}{\partial x^2} + \frac{\partial^2 w}{\partial z^2} \right).$$

Taking in consideration that the flow is fully developed, all the derivatives of velocities to x (direction of the flow) will be dropped, because it does not change anymore. In this case the system will become even simpler

$$\frac{\partial w}{\partial z} = 0,$$

$$\rho w \frac{\partial u}{\partial z} = -\frac{\partial p}{\partial x} + \mu \frac{\partial^2 u}{\partial z^2},$$

$$\rho w \frac{\partial w}{\partial z} = -\frac{\partial p}{\partial z} + \mu \frac{\partial^2 w}{\partial z^2}.$$

Next, we will consider two boundary conditions, the no-penetration and no-slip boundary condition. The first one, represents the fact that the fluid will not pass through the plates, and we can write it like

$$w(x, y, 0) = w(x, y, h) = 0,$$

which means that $w = 0$ for all z.

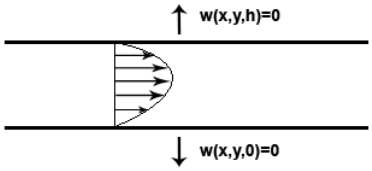

Figure 4.2.3: No-penetration condition

Now we are left with the first momentum equation which relates the horizontal pressure drop to the viscous term and a relation which states that pressure is constant over the height.

$$\frac{\partial p}{\partial x} = \mu \frac{\partial^2 u}{\partial z^2}, \tag{4.2.20}$$

$$\frac{\partial p}{\partial z} = 0.$$

This expression $\frac{\partial p}{\partial z}$ is a function of z only, so we can directly integrate the first expression (eq. 4.2.20) over the height z.

$$\frac{\partial^2 u}{\partial z^2} = \frac{1}{\mu}\frac{\partial p}{\partial x},$$

$$\frac{\partial u}{\partial z} = \frac{1}{\mu}\frac{\partial p}{\partial x} z + C_1,$$

$$u(z) = \frac{1}{2\mu}\frac{\partial p}{\partial x} z^2 + C_1 z + C_2. \tag{4.2.21}$$

The second boundary condition that we will use is the no-slip[4] condition, which is

$$u\left(0\right) = u\left(h\right) = 0.$$

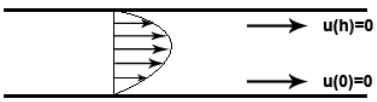

Figure 4.2.4: No-slip boundary condition

Using the first condition $u(0) = 0$, we have that $C_2 = 0$. Using the second condition $u(h) = 0$, we have that $C_1 = -\frac{1}{2\mu}\frac{\partial p}{\partial x} h$. Substituting these in equation (4.2.21), we find

[4]No slip means that at a solid boundary the fluid will have zero velocity relative to the boundary.

$$u(z) = -\frac{1}{2\mu}\frac{\partial p}{\partial x} z\,(h-z)\,. \tag{4.2.22}$$

Thus, Poiseuille flow has a parabolic profile, and it flows in the direction of decreasing pressure.

We will continue with a two dimensional approximation, using the main result from the Poiseuille flow, which is the solution for a specific case. We will use the previous result, the existence of a solution in form of a parabolic profile, to analyze the Navier-Stokes equation, without imposing so many restrictions as we did in the last section.

Without restricting ourself to a single flow direction, we assume a profile φ in z direction, which is the same in both horizontal directions, and laminar[5] flow, i.e. no speed in z direction anywhere:

$$\begin{aligned} u(x,y,z) &= \bar{u}(x,y)\varphi(z), \\ v(x,y,z) &= \bar{v}(x,y)\varphi(z), \\ w(x,y,z) &= 0. \end{aligned}$$

We choose to scale φ such that it is dimensionless

$$\int_0^h \varphi\,(z)\,dz = h,$$

and $\bar{u}$ and $\bar{v}$ stand for the average speeds in x and y directions.

For a parabolic profile (which represents laminar flow), this means

$$\varphi(z) = \frac{6}{h^2} z\,(h-z)\,.$$

We insert these speeds in the incompressible Navier-Stokes, mass equation (4.2.18) and momentum equation (4.2.19), to find

$$\varphi\left(\frac{\partial \bar{u}}{\partial x} + \frac{\partial \bar{v}}{\partial y}\right) = 0,$$

$$\rho\varphi^2\left(\bar{u}\frac{\partial \bar{u}}{\partial x} + \bar{v}\frac{\partial \bar{u}}{\partial y}\right) = -\frac{\partial p}{\partial x} + \mu\left(\varphi\frac{\partial^2 \bar{u}}{\partial x^2} + \varphi\frac{\partial^2 \bar{u}}{\partial y^2} + \varphi''\bar{u}\right),$$

$$\rho\varphi^2\left(\bar{u}\frac{\partial \bar{v}}{\partial x} + \bar{v}\frac{\partial \bar{v}}{\partial y}\right) = -\frac{\partial p}{\partial y} + \mu\left(\varphi\frac{\partial^2 \bar{v}}{\partial x^2} + \varphi\frac{\partial^2 \bar{v}}{\partial y^2} + \varphi''\bar{v}\right),$$

$$\frac{\partial p}{\partial z} = 0.$$

[5] Laminar flow, means that the fluid moves in "layers", in contrast to the chaotic motion of the turbulent flow.

For a laminar flow, we integrate the first three equations over z from 0 to h, and divide these by h. In order to do that we will need these relations: $\varphi'' = -12/h^2$, $\int_0^h dz = h$, $\int_0^h \varphi dz = h$ which is the scale and $\int_0^h \varphi^2 dz = 6h/5$. After integration the system will be reduced to a two-dimensional equation:

$$\frac{\partial \bar{u}}{\partial x} + \frac{\partial \bar{v}}{\partial y} = 0,$$

$$\frac{6}{5}\rho\left(\bar{u}\frac{\partial \bar{u}}{\partial x} + \bar{v}\frac{\partial \bar{u}}{\partial y}\right) = -\frac{\partial p}{\partial x} + \mu\left(\frac{\partial^2 \bar{u}}{\partial x^2} + \frac{\partial^2 \bar{u}}{\partial y^2} - \frac{12}{h^2}\bar{u}\right),$$

$$\frac{6}{5}\rho\left(\bar{u}\frac{\partial \bar{v}}{\partial x} + \bar{v}\frac{\partial \bar{v}}{\partial y}\right) = -\frac{\partial p}{\partial y} + \mu\left(\frac{\partial^2 \bar{v}}{\partial x^2} + \frac{\partial^2 \bar{v}}{\partial y^2} - \frac{12}{h^2}\bar{v}\right).$$

This can be written in a vector form as

$$\nabla \bar{\mathbf{u}} = 0, \tag{4.2.23}$$

$$\frac{6}{5}\rho \bar{\mathbf{u}} \cdot \nabla \bar{\mathbf{u}} = -\nabla p + \mu \nabla^2 \bar{\mathbf{u}} - \frac{12\mu}{h^2}\bar{\mathbf{u}}. \tag{4.2.24}$$

This equation looks like the normal incompressible Navier-Stokes, without the last term. The rightmost term describes the viscous losses to the two plates and the fact that the density increases a bit.

The distance between the two plates is much smaller than the horizontal distances, which makes the term $\frac{12\mu\bar{\mathbf{u}}}{h}$ much larger than the two dimensional viscous term $\mu\nabla^2\bar{\mathbf{u}}$. For this reason we can neglect the second term in the RHS of the equation (4.2.24).

In order to demonstrate that $\frac{12\mu\bar{\mathbf{u}}}{h} \gg \mu\nabla^2\bar{\mathbf{u}}$ we will make a dimensionless analysis, so that we can compare them, to see which one influence more the fluid flow. Let's consider the following dimensionless notations L for the 2D horizontal length scale, h for the layer thickness ($L \gg h$), U for velocity and for pressure we have $p = \frac{\mu U}{L}$. We will set the following: $x = L\widetilde{x}$, $y = L\widetilde{y}$, $z = L\widetilde{z}$, $\bar{u} = U\widetilde{u}$, $\bar{v} = U\widetilde{v}$, $p = \frac{\mu U}{L}\widetilde{p}$ and $\nabla = \frac{1}{L}\widetilde{\nabla}$.

Further the equation (4.2.24) will be written in a non-dimensional form

$$\frac{6}{5}\rho U\widetilde{u}\frac{1}{L}\widetilde{\nabla}\left(U\widetilde{u}\right) = -\frac{1}{L}\widetilde{\nabla}\frac{\mu U}{L}\widetilde{p} + \frac{\mu U}{L^2}\widetilde{\nabla}^2\widetilde{u} - \frac{12\mu}{h^2}U\widetilde{u}.$$

Dividing the equation with $\mu U/h^2$ leads to

$$\frac{6}{5}\frac{\rho U h^2}{L\mu}\frac{L}{L}\left(\widetilde{u}\widetilde{\nabla}\widetilde{u}\right) = -\frac{h^2}{L}\widetilde{\nabla}\widetilde{p} + \frac{h^2}{L^2}\widetilde{\nabla}^2\widetilde{u} - 12\widetilde{u}.$$

Substituting $\varepsilon = h/L$ and Reynold's Number $Re_L = \frac{\rho UL}{\mu}$ in the previous equation, we obtain

$$\frac{6}{5} Re_L \varepsilon^2 \widetilde{u} \widetilde{\nabla} \widetilde{u} = -\varepsilon^2 \widetilde{\nabla} \widetilde{p} + \varepsilon^2 \widetilde{\nabla}^2 \widetilde{u} - 12\widetilde{u},$$

$$\varepsilon^2 \left(\frac{6}{5} Re_L \widetilde{u} \widetilde{\nabla} \widetilde{u} + \widetilde{\nabla} \widetilde{p} \right) = \left(\varepsilon^2 \widetilde{\nabla}^2 - 12 \right) \widetilde{u}. \tag{4.2.25}$$

We look only at slow flows so the Reynold's Number is small which leads to

$$Re_L \widetilde{u} \cdot \widetilde{\nabla} \widetilde{u} + \widetilde{\nabla} \widetilde{p} \approx \widetilde{\nabla} \widetilde{p}.$$

Furthermore if $\varepsilon \ll 1$ we have

$$\left(\varepsilon^2 \widetilde{\nabla}^2 - 12 \right) \approx -12.$$

Considering the last two observations, equation (4.2.25) will become

$$\varepsilon^2 \widetilde{\nabla} \widetilde{p} \approx -12\widetilde{u},$$

this means that $\frac{12\mu \bar{\mathbf{u}}}{h} \gg \mu \nabla^2 \bar{\mathbf{u}}$ is true, so we can drop the viscous term.

The system of the laminar flow will be much simpler now

$$\nabla \bar{\mathbf{u}} = \mathbf{0}, \tag{4.2.26}$$

$$\frac{6}{5} \rho \bar{\mathbf{u}} \cdot \nabla \bar{\mathbf{u}} = -\nabla p - \mu \frac{12}{h^2} \bar{\mathbf{u}}. \tag{4.2.27}$$

We can write the formula for the gradient of the pressure from the equation (4.2.27), which is

$$\nabla p = -\frac{12\mu}{h^2} \bar{\mathbf{u}}.$$

Applying gradient to the previous equation we get another expression

$$\nabla^2 p = -\frac{12\mu}{h^2} \nabla \bar{\mathbf{u}} = 0.$$

Thus, the system for the laminar flow will look like

$$\nabla^2 p = 0, \tag{4.2.28}$$

$$\bar{\mathbf{u}} = -\frac{h^2}{12\mu} \nabla p. \tag{4.2.29}$$

The first equation represents the potential flow and the second equations of the system represents the speed in terms of pressure gradient.

We can fill it directly into the equation of mass conservation, to obtain

$$\nabla \mathbf{u} = \nabla \left(-\frac{h^2}{12\mu} \nabla p \right) = 0,$$

$$\frac{\partial^2 p}{\partial x^2} + \frac{\partial^2 p}{\partial y^2} = 0.$$

This equation is actually the Hele-Shaw governing equation.

4.3 Surface tension in SPH

In this Chapter we looked over different approaches of how to plug in surface tension into flow. The flow that we chose was Hele-Shaw, because it is a simpler flow which has diffusion. First we looked over Van der Waals approach, which turned out to be too complicated and not what we were looking. Then we analyze the Cahn-Hilliard equation, which models a phase separation process. This was an interesting approach but we decided to go with Tartakovsky's approach, to add an attractive force to the system.

4.3.1 Van der Waals equation

The equation of van der Waals is used for fluids composed of particles with positive volume. Between these particles there is an attractive force. This force can be a van der Waals interaction force, which is the sum of the attractive forces between particles, see [23]. This equation is a state equation because it uses the following states variables, and describes the relationship between them: the pressure p, the volume of the container in which is the fluid V, the absolute temperature T and the number of moles n.

Van der Waals equation of state can be used to model the behavior of the fluid. We need the equation of states in order to close the following Euler equation system

$$\frac{D\rho_i}{Dt} = \sum_{j=1}^{N} m_j v_{ij}^{\alpha} \frac{\partial W_{ij}}{\partial x_i^{\alpha}},$$

$$\frac{Dv_i^{\alpha}}{Dt} = -\sum_{j=1}^{N} \left(\frac{p_i}{\rho_i^2} + \frac{p_j}{\rho_j^2} \right) m_j \frac{\partial W_{ij}}{\partial x_i^{\alpha}}.$$

One form of the equation of van der Waals is

$$\left(p + \frac{a}{v^2} \right) (v - b) = kT,$$

where k is the Boltzmann's constant, v is the volume of the container shared between each particle, a measures the strength of the attraction force and b is representing the size of the particle.

From the equation of van der Waals, pressure can be written as

$$p = \frac{kT}{v-b} - \frac{a}{v^2}.$$

We can rewrite the pressure equation in terms of density, $1/v$, as

$$p = \frac{\rho kT}{1-\rho b} - a\rho^2, \tag{4.3.1}$$

where the second term is the cohesive pressure.

Considering as Liu and Liu in [23] the SPH approximation for pressure and from (4.3.1) only the cohesive pressure part we get the following SPH formulation

$$\frac{Dv_i^\alpha}{Dt} = -\sum_{j=1}^{N} m_j \left(\frac{-a\rho_i^2}{\rho_i^2} + \frac{-a\rho_j^2}{\rho_j^2} \right) \frac{\partial W_{ij}}{\partial x_i^\alpha} + 2a \sum_{j=1}^{N} m_j \frac{\partial W_{ij}}{\partial x_i^\alpha}.$$

Now the system will become

$$\frac{D\rho_i}{Dt} = \sum_{j=1}^{N} m_j v_{ij}^\alpha \frac{\partial W_{ij}}{\partial x_i^\alpha},$$

$$\frac{Dv_i^\alpha}{Dt} = -\sum_{j=1}^{N} \left(\frac{p_i}{\rho_i^2} + \frac{p_j}{\rho_j^2} \right) m_j \frac{\partial W_{ij}}{\partial x_i^\alpha} + 2a \sum_{j=1}^{N} m_j \frac{\partial W_{ij}}{\partial x_i^\alpha}.$$

A major drawback of this method is that we have had to change the equation of state to the assumption that we deal with a Van der Waals - fluid. This is not desirable, if we want to model hypervelocity impacts. With all phase transitions the equations of state needed are already complicated enough. Another severe drawback of this method is that the parameter a and b are actually not physical parameters of the underlying material but properties of the SPH particle system. Having to tune two parameters is unwanted.

4.3.2 Cahn-Hilliard equation

The equation of Cahn-Hilliard models the phase separation process. When we say separation we refer to a binary fluid that by separation forms two pure domains.

Following the approach of P. Gao and J.J. Feng in [8], we will consider two Newtonian fluids, to be incompressible ($\nabla \mathbf{u} = 0$) and immiscible to each other. We will neglect inertia and gravity.

A new variable will be a phase-field variable, noted by ϕ, which will indicate the domain, $\phi = 1$ in the first fluid and $\phi = -1$ in the second fluid.

The Cahn-Hilliard equation for advection and diffusion of ϕ described in [8] is

$$\frac{D\phi}{Dt} = \frac{\partial \phi}{\partial t} + \mathbf{u} \cdot \nabla \phi = \nabla \cdot (\gamma \nabla G), \tag{4.3.2}$$

where t is for time, $\mathbf{u}$ is the flow velocity vector, γ is representing the mobility parameter and G is the chemical potential. The G variable is such that

$$G = \lambda \left[-\nabla^2 \phi + \left(\phi^2 - 1 \right) \phi / \epsilon^2 \right],$$

where λ is the mixing energy density and ϵ is used for the capillary width.

It is a challenge to solve (4.3.2) numerically because it is a fourth order equation. For that reason, we will simplify the equation.

Considering the Navier Stokes (NS) equations for the flow of the fluid, and the Cahn Hilliard (CH) model, we will have the following system

$$\nabla \cdot \mathbf{u} = 0, \tag{4.3.3}$$

$$\rho \left(\frac{\partial v}{\partial t} + \mathbf{u} \cdot \nabla \mathbf{u} \right) = -\nabla p + \mu \nabla^2 \mathbf{u} + G \nabla \phi, \tag{4.3.4}$$

$$\frac{D\phi}{Dt} = \nabla \cdot (\gamma \nabla G). \tag{4.3.5}$$

The momentum equation has an extra term $G\nabla\phi$, which is the contribution of the interfacial force, and μ is the viscosity.

The material derivative of equation (4.3.4) can be written as

$$\frac{Du}{Dt} = \frac{1}{\rho} \left(-\nabla p + \mu \nabla^2 \mathbf{u} + G \nabla \phi \right).$$

Replacing the second order term with $\frac{12\mu}{h^2}$, will give rise to the Hele-Shaw equation, as we show in Chapter 3

$$\frac{Du}{Dt} = \frac{1}{\rho} \left(-\nabla p - \frac{12\mu}{h^2} \mathbf{u} + G \nabla \phi \right).$$

Now, the mass conservation equation in a general form is written as

$$\frac{\partial \rho}{\partial t} + \nabla (\rho \mathbf{u}) = 0.$$

Applying the product rule, this leads to

$$\frac{\partial \rho}{\partial t} + \rho \nabla \mathbf{u} + \mathbf{u} \nabla \rho = 0.$$

So, the material derivative of the previous equation is

$$\frac{D\rho}{Dt} = -\rho (\nabla \mathbf{u}).$$

Further, assume that $\gamma = 0$, so we can simplify (4.3.2) as

$$\frac{D\phi}{Dt} = \frac{\partial \phi}{\partial t} + \mathbf{u} \cdot \nabla \phi = 0.$$

After all modifications, the system becomes

$$\frac{D\rho}{Dt} = -\rho (\nabla \mathbf{u}),$$

$$\frac{Du}{Dt} = \frac{1}{\rho} \left(-\nabla p - \frac{12\mu}{h^2} \mathbf{u} + G \nabla \phi \right),$$

$$\frac{D\phi}{Dt} = 0.$$

Further, we will write SPH formulations for the equations of the system. Using equation (4.1.5) from the previous chapter, the SPH discretization of the system is

$$\frac{D\rho_i}{Dt} = \rho \sum_{j=1}^{N} \frac{m_j}{\rho_j} u_j \nabla_i W_{ij}, \tag{4.3.6}$$

$$\frac{Du_i}{Dt} = \frac{1}{\rho_i} \sum_{j=1}^{N} \frac{m_j}{\rho_j} p_j \nabla_i W_{ij} - \frac{12\mu}{h^2} \frac{u_i}{\rho_i} + \frac{G}{\rho_i} \sum_{j=1}^{N} \frac{m_j}{\rho_j} \phi_j \nabla_i W_{ij}, \tag{4.3.7}$$

$$\frac{D\phi}{Dt} = -\sum_{j=1}^{N} \frac{m_j}{\rho_j} \phi_j \nabla W_{ij} = 0.$$

Another SPH formulation for the mass conservation can be written using formula (4.1.6):

$$\frac{D\rho_i}{Dt} = -\rho_i \left[\frac{1}{\rho_i} \left(\sum_j m_j \left(u_j - u_i \right) \nabla_i W_{ij} \right) \right]$$

$$= \sum_{j=1}^{N} m_j \left(u_i - u_j \right) \nabla_i W_{ij} = \sum_{j=1}^{N} m_j u_{ij} \nabla_i W_{ij}.$$

Using the same formula, the SPH momentum equation is

$$\frac{Du_i}{Dt} = \frac{1}{\rho_i} \left[-\frac{1}{\rho_i} \sum_{j=1}^{N} m_j \left(p_j - p_i \right) \nabla_i W_{ij} \right] - \frac{12\mu}{h^2} \frac{u_i}{\rho_i} + \frac{G}{\rho_i} \frac{1}{\rho_i} \left[\sum_{j=1}^{N} m_j \left(\phi_j - \phi_i \right) \nabla_i W_{ij} \right],$$

$$\frac{Du_i}{Dt} = -\frac{1}{\rho_i^2} \sum_{j=1}^{N} m_j \left(p_j - p_i \right) \nabla_i W_{ij} - \frac{12\mu}{h^2} \frac{u_i}{\rho_i} + \frac{G}{\rho_i^2} \sum_{j=1}^{N} m_j \left(\phi_j - \phi_i \right) \nabla_i W_{ij}.$$

We can derive another formulation for the momentum equation using formula (4.1.7) as

$$\frac{Du_i}{Dt} = \frac{1}{\rho_i} \left[-\rho_i \sum_{j=1}^{N} m_j \left(\frac{p_j}{\rho_j^2} + \frac{p_i}{\rho_i^2} \right) \nabla_i W_{ij} \right] - \frac{12\mu}{h^2} \frac{u_i}{\rho_i} + \frac{G}{\rho_i} \rho_i \left[\sum_{j=1}^{N} m_j \left(\frac{\phi_j}{\rho_j^2} + \frac{\phi_i}{\rho_i^2} \right) \nabla_i W_{ij} \right],$$

$$\frac{Du_i}{Dt} = -\sum_{j=1}^{N} m_j \left(\frac{p_j}{\rho_j^2} + \frac{p_i}{\rho_i^2} \right) \nabla_i W_{ij} - \frac{12\mu}{h^2} \frac{u_i}{\rho_i} + G \sum_{j=1}^{N} m_j \left(\frac{\phi_j}{\rho_j^2} + \frac{\phi_i}{\rho_i^2} \right) \nabla_i W_{ij}.$$

The first term from (4.3.7)

$$\frac{1}{\rho_i} \sum_{j=1}^{N} \frac{m_j}{\rho_j} p_j \nabla_i W_{ij}, \tag{4.3.8}$$

can be rewritten as

$$\frac{1}{\rho_i} \sum_{j=1}^{N} \frac{m_j}{\rho_j} p_j \nabla_i W_{ij} = \frac{p_i}{\rho_i} \left(\sum_{j=1}^{N} \frac{m_j}{\rho_j} \nabla_i W_{ij} \right) = 0, \tag{4.3.9}$$

where the term in brackets is zero.

Adding (4.3.8) with (4.3.9) leads to

$$\frac{1}{\rho_i}\sum_{j=1}^{N}\frac{m_j}{\rho_j}p_j\nabla_i W_{ij}+\frac{p_i}{\rho_i}\sum_{j=1}^{N}\frac{m_j}{\rho_j}\nabla_i W_{ij}=\sum_{j=1}^{N}\frac{p_j+p_i}{\rho_j\rho_i}m_j\nabla_i W_{ij}. \tag{4.3.10}$$

If we do the same steps for the third term in (4.3.7) $\frac{1}{\rho_i}\sum_{j=1}^{N}\frac{m_j}{\rho_j}\phi_j\nabla_i W_{ij}$, will lead to

$$\frac{1}{\rho_i}\sum_{j=1}^{N}\frac{m_j}{\rho_j}\phi_j\nabla_i W_{ij}+\frac{\phi_i}{\rho_i}\sum_{j=1}^{N}\frac{m_j}{\rho_j}\nabla_i W_{ij}=\sum_{j=1}^{N}\frac{\phi_j+\phi_i}{\rho_j\rho_i}m_j\nabla_i W_{ij}. \tag{4.3.11}$$

Putting all together (4.3.10) and (4.3.11), another SPH discretization of momentum can be defined by

$$\frac{Dv}{Dt}=-\sum_{j=1}^{N}\frac{p_j+p_i}{\rho_j\rho_i}m_j\nabla_i W_{ij}-\frac{12\mu}{h^2}u+G\sum_{j=1}^{N}\frac{\phi_j+\phi_i}{\rho_j\rho_i}m_j\nabla_i W_{ij}.$$

Note that this looks similar to the Van der Waals approach, where the contribution of the surface tension also shows a summation of terms with $m_j\nabla_i W_{ij}$. This superficial similarity is invalid however: the Cahn-Hilliard equation only puts a force near the interface, as G is only non-zero near the interface. This is also the drawback: the computation of G requires the use of the second derivative of the kernel, which is an unwanted property. If we can reformulate this second derivative, however, the method might be very interesting. Even if it has some parameters, the relation between λ and ε on one side and surface tension γ on the other has been well established.

4.3.3 Particle system potential(Tartakovsky's approach)

In [32], Tatrakovsky introduces an easier approach with resembles the approach chosen by Liu to simulate

$$f_{ij}=\begin{cases}s_{ij}\cos(\frac{1}{2}\pi\|\mathbf{r}\|/h)\frac{\mathbf{r}}{\|\mathbf{r}\|}, & \|\mathbf{r}\|\leq h\\ 0, & \|\mathbf{r}\|>h\end{cases}. \tag{4.3.12}$$

Here s_{ij} is a coefficient that catches the attraction between particles and $\mathbf{r}=\mathbf{r}_j-\mathbf{r}_i$. It is only dependent on the species of particles i and j. For a single fluid free boundary problem, or for a two fluid problem with an interface, it only needs to be non-zero for particles of the same kind. Interestingly, attractive forces can be applied between particles of different species (just as in reality) with which contact angles can be simulated. The number S_{ij} can be determined by tuning benchmark cases.

This force will be added to the momentum equation of Hele-Shaw flow.

The benefit of this approach is most of all its simplicity: rather than operating in the smoothed domain, it is directly applied on the particles themselves. It has only one parameter to tune, e.g. via the pressure in a droplet.

4.4 Implementation

Because of the ease of implementation, the fact that it does not need alterations in the equation of state, and the general applicability we have chosen to implement Tartakovsky's approach of Section 4.3.3 into Iason Zisis' hypervelocity impact simulator. This is a compact SPH implementation written in C++. The compactness makes it ideal to test new ideas.

We implemented as Euler with additional force terms (force for Hele-Shaw and surface tension) on the particles, so equation (4.2.13) remains the same

$$\frac{D\rho_i}{Dt} = \rho_i \sum_{j=1}^{N} \left(u_{ij}^1 \frac{\partial W_{ij}}{\partial x_i^1} dV_j + u_{ij}^2 \frac{\partial W_{ij}}{\partial x_i^2} dV_j \right),$$

and (4.2.14),(4.2.15) written in α coordinate direction, becomes

$$\frac{Du_i^\alpha}{Dt} = -\sum_{j=1}^{N} \{ m_j \frac{p_{i+}p_j}{\rho_i \rho_j} \frac{\partial W_{ij}}{\partial x_i^k} - f_{ij}^{TR} \} - f_i^{HS},$$

where f_{ij}^{TR} is the Tartakovsky's attraction force defined in (4.3.12) and f_i^{HS} is the Hele-Shaw term defined in (4.4.1).

We have tried various variations on Tartakovsky's approach. In it its pure form equation (4.3.12) acts on the particles, and this is the approach we will show in the results below. However, Zisis' SPH formulation has a couple of extensions to the standard SPH formulation, that allows for mass differences between the particles, but more importantly uses a variable smoothing length. This means that the summation over j of equation (4.3.12) is best interpreted as a volume-integral.

Also the Hele-Shaw friction was implemented as a particle force:

$$\mathbf{f}_i^{HS} = -\mu_{HS} \mathbf{u}_i, \tag{4.4.1}$$

where μ_{HS} is some tunable parameter. In the experiments below we have only used this force to overcome very high velocities, for example in the case of a square-shaped bubble turning into a circle. The sharp corners of a square have zero radius and

therefore infinite curvature. Also the pressure jump would become infinity at that point according to the Young-Laplace equation. Fortunately, SPH smoothens things out already. However, since we are more interested in the shape changes of the bubble than in the internal reflections of the pressure waves, this term helps us to dampen things out.

For the equation of state we have used a quasi-incompressible relation [34, 35]:

$$p = \frac{\mathrm{Ca}}{7}\left[\left(\frac{\rho}{\rho_0}\right)^7 - 1\right], \tag{4.4.2}$$

where $Ca = \frac{\rho_0 C_0^2}{K}$, which is the speed of sound over the bulk modulus state medium.

4.5 Results and discussion

To test the implementation of the Tartakovsky's approach, we have selected a few test cases. First of all we will be looking at how surface tension makes a circle from a square start form. Then we look how surface tension affects hypervelocity impacts.

4.5.1 Circling the square

In this section we check if our surface tension works as expected. Without any external force the surface should take a circular form and the pressure should increase. We will look for two cases of initial squares, with different dimension, but the same Tartakovsky attraction coefficient s_{ij}. The attraction force was added to a Hele-Shaw flow.

Small square Assume a square with the length of 0.01 and the width of 0.01. The grid layout has 625 particles (25 x 25) equal distributed. The parameters used are: $s_{ij} = 10$, Ca = 1, $\mu_{HS} = 1$. The simulation is made for 10,000 timesteps of 0.1 ms each.

The results are represented in Figure 4.5.1, where we can observe the effect of surface tension into SPH. As we expected the square shape is deformed, and as the timestep increase the shape is becoming more round. In Figure 4.5.2, can be seen the increase of pressure, as we expected, and the low pressure at the sharp corners of the square.

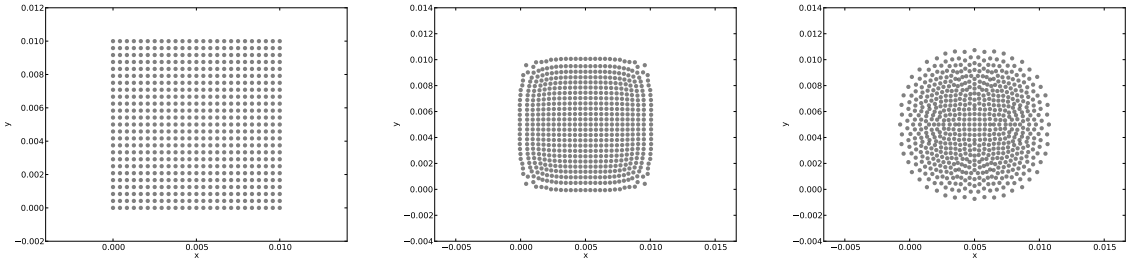

Figure 4.5.1: Small square. Initial configuration, after 1000 timesteps, after 10,000 timesteps.

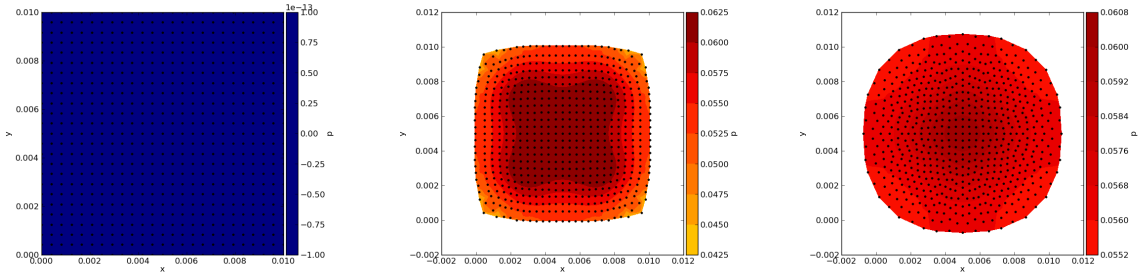

Figure 4.5.2: Pressure at 0 s, 100 ms and 1 s.

Large square, same high friction In this example we considered a much bigger square, with length of 1.0 and width of 1.0, with the same amount of particles in the grid layout as before. We kept also the Tartakovsky parameter $s_{ij} = 10$, Ca = 1 and $\mu_{HS} = 1$, the same. The simulation is made for 10,000 times steps of 0.1 ms each.

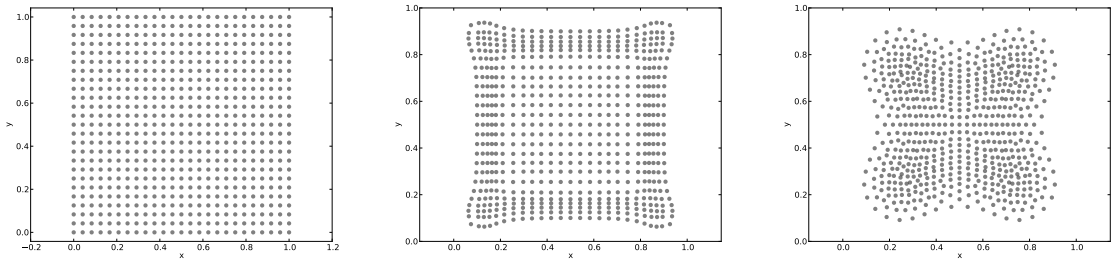

Figure 4.5.3: Large square. Initial configuration, after 1000 timesteps, after 10,000 timesteps.

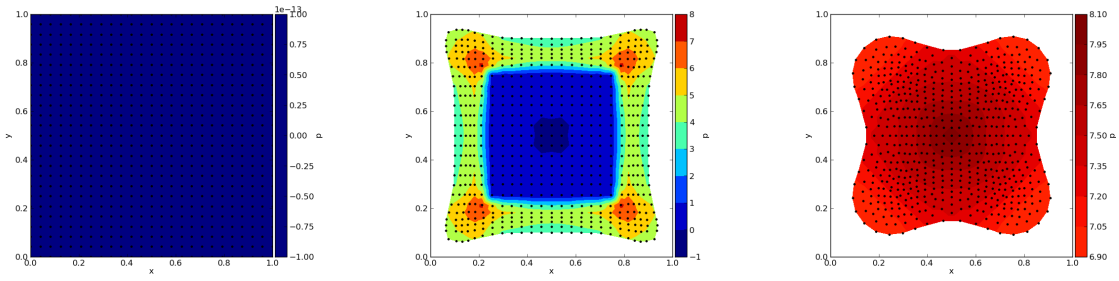

Figure 4.5.4: Pressure at 0 s, 100 ms and 1 s.

The results are illustrated in Figure 4.5.3 and how pressure changed in Figure 4.5.4. As we can see the pressure increases, shape becomes round but at the end changes are so slow, a circle is not even obtained after 100,000 timesteps. This is because of too high friction as we will see next.

Large square, lower friction For the last case, we assumed again a large square with length 1 and width 1. Parameters that we kept are the Tartakovsky $s_{ij} = 10$ and Ca = 1. This time we changed the friction coefficient, by decreasing it to $\mu_{HS} = 0.01$. The simulation is made for 20,000 times steps of 0.1 ms each.

Now the results are the desired ones. The fluid is set in motion by the high pressures (Figure 4.5.6), eventually it dampens out. Pressure increases and the shape becomes round now, Figure 4.5.5.

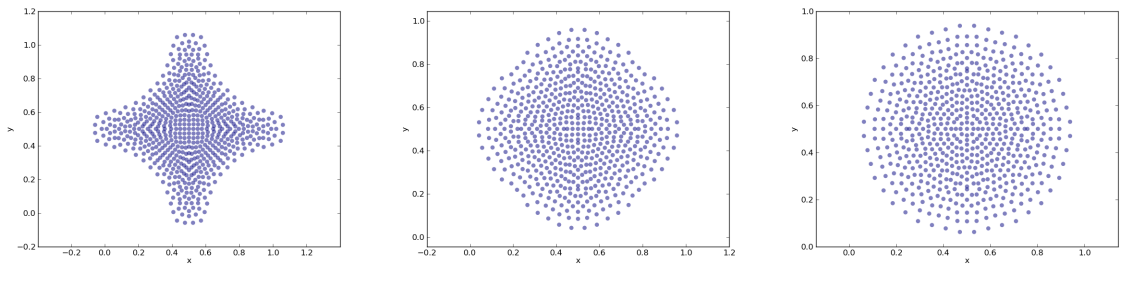

Figure 4.5.5: Large square, low μ_{HS}. After 5000 timesteps, 10,000 and 20,000 timesteps.

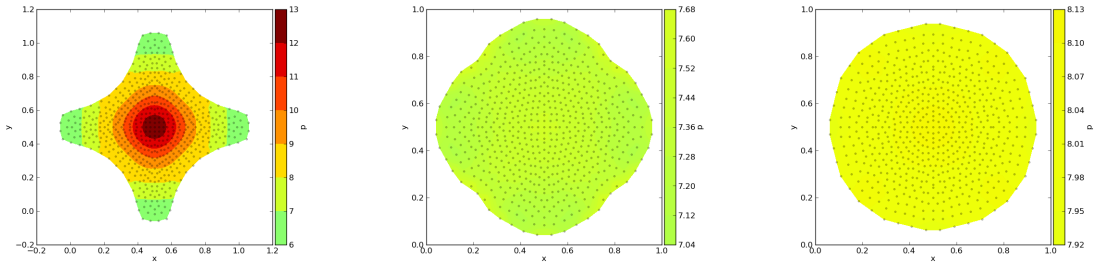

Figure 4.5.6: Pressure at 50 s, 100 ms and 1 s.

Comparing the results of this large square, with low friction, with the results of the small square, we can say that the computations are correct, since the surface tension is approximately constant. We know, by computing the surface tension with formula $\gamma = R\Delta p$, where R is the radius and Δp is the pressure difference. Note that the surface tension is scaled with $h = L/N$, where h is the distance between particles, L is length and N is particles number.

4.5.2 Hypervelocity impacts

Reference: no surface tension Further we will look how surface tension affects hypervelocity impacts. For that, first we have to consider a case without surface tension, for a Hele-Shaw flow.

We consider two rectangles, which consist of 3125 particles for two grid layouts, and we will simulate an impact between those two. The parameters then will be Tartakovsky $s_{ij} = \mathbf{0}$, Ca = 1 and $\mu_{HS} = 0$. For the left rectangle the initial horizontally velocity is $u = 1$. The simulation is made for 10,000 times steps of 0.1 ms each.

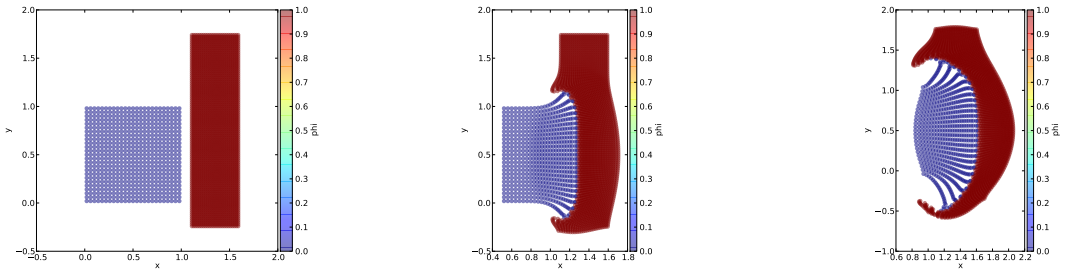

Figure 4.5.7: Hypervelocity impacts, without considering surface tension. (Initial configuration, after 1000 timesteps, after 10,000 timesteps.)

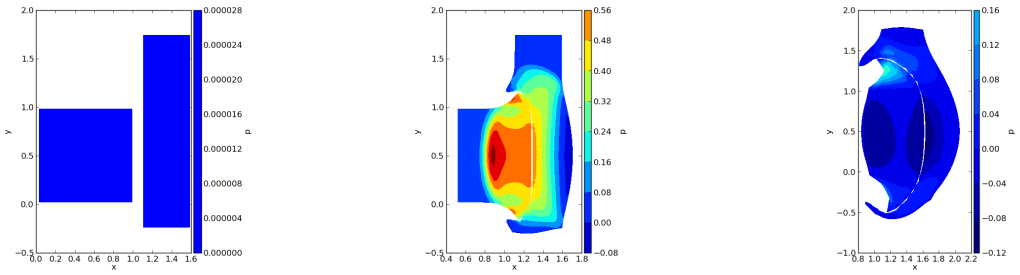

Figure 4.5.8: Pressure at 0 s, 100 ms and 1 s.

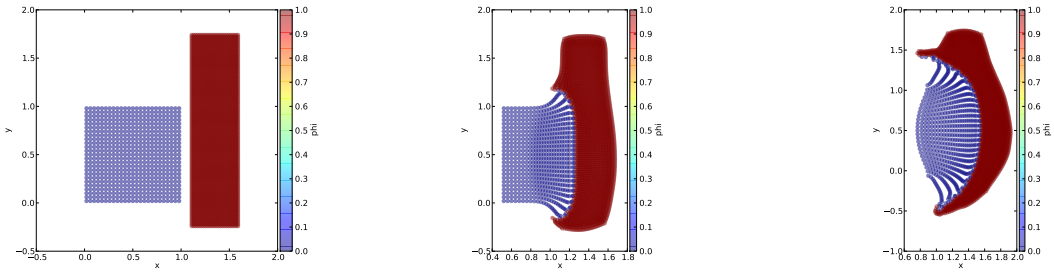

Figure 4.5.9: Hypervelocity impacts, considering surface tension. Initial configuration, after 1000 timesteps, after 10,000 timesteps.

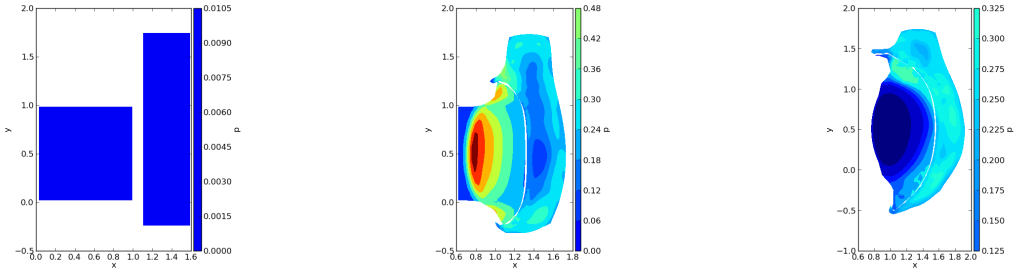

Figure 4.5.10: Pressure at 0 s, 100 ms and 1 s.

Reference: with surface tension The next step is to add surface tension to Hele-Shaw flow. We take as parameters: Tartakovsky $s_{ij} = 0$ for projectile (left rectangle), $s_{ij} = \mathbf{1}$ for the plate at rest (right rectangle), Ca = 1 and the friction coefficient $\mu_{HS} = 0$. We will assume the same amount of particles in those two grid layouts and again the

initial horizontal velocity $u = 1$, for the left rectangle. The simulation is made for 10,000 times steps of 0.1 ms each.

Discussion Looking to the previous two cases, Figure 4.5.7 and Figure 4.5.9, it is clear that surface tension keeps particles together, due to the fact that there are less particles shot back from the plate, above and below the projectile. Another difference is that the interface between the objects is rounder, when surface tension is present.

5 Conclusion

In this thesis we have shown how to find the shape of bubbles and droplets by using different numerical techniques and how to treat free surface flows that involve surface tension.

We found the shape of droplets by using two different methods: the shooting method and an optimization method. The shooting method, solves a (non-linear) ordinary differential system involving the curvature as a function of angle around the shape in order to find the solution. On the other hand, the optimization method minimize the curvature, by computing it repeatedly, in order to find the proper solution. We found the curvature in two ways: one by circle fitting and one by central differences. The circle fit algorithm is more accurate when it is computed for a big number of neighbor points. The central differences algorithm is more accurate for smooth data, while the circle fit algorithm is better to be used for noisy data. Both methods, the shooting and optimization method succeed on all test cases but there are some differences that we can depict : the shooting method is more sensitive to initial guesses. In some cases, this system can become stiff, and create difficulties in solving it with explicit numerical methods, so a proper solver has to be chosen. Another difference of these two methods is the way they conserve area. The area is always preserved with the shooting method, but we cannot always rely on the optimization method to behave the same.

Simulations with both methods, show that the shape of droplets and bubbles are influenced by their dimension. Thus, small droplets have a spherical shape and the larger they get, the deformation is more pronounced. Another factor that influences the shape of droplets and bubbles is their velocity. Increased velocity will also induce a proportional rise in the pressure that acts over the surface. This also alters the shape of the droplet. The shape of droplets that are falling with high velocity are more deformed than those that are falling much slower.

The shape of droplets, has been computed by plugging pressure into curvature. In every case the effects of surface tension are more visible for larger droplets. This can be observed also in several COMSOL simulations, where we computed the shape of a raising bubble. Surface tension effects are predictable by using the Eötvös number. For bubbles computed with a small Eötvös number, indicating that the surface tension dominates, the shape is spherical, while for a bigger Eötvös number, the bubble is deformed to a more flatten shape, because in this case the buoyancy forces dominate over the surface ones.

Aspects of Smoothed Particle Hydrodynamics and flows were treated in this thesis, where surface tension effects are quite complicate to be simulated from the point of

a flow. Here, we explored different flows, as Navier-Stokes flow, which describe the motion of a fluid, then we analyzed Euler's frictionless flow. In the end Hele-Shaw flow was treated as a viscous flow and proved to be a more accessible model. This is similar to the Navier-Stokes flow, but the equations that describe it are simplified, because the second derivative diffusion term is replaced with a simpler term.

We presented three ways to introduce surface tension in SPH: the first uses equation of Van der Waals, second one is based on the equation of Cahn-Hilliard and the last one is a particle system potential treated with Tartakovsky's approach, which was implemented into Iason Zisis' hypervelocity impact simulator. Tests have been done to point how surface tension tends to minimize a shape area. The including of surface tension in hypervelocity impacts, was a success, because the behavior is the expected one. More particles stay together in a more rounded shape than for the case without surface tension.

This thesis proved to be a good study case because our goals were reached. We reproduced the shape of droplets and bubbles by using different numerical methods and we introduced surface tension in hypervelocity impacts.

Bibliography

[1] M.B. Allen III and E.L. Isaacson. *Numerical Analysis for Applied Science*. New York: Wiley-Interscience, 1998. p. 188-189.

[2] R. Ashino, M. Nagase, R. Vaillancourt . Behind and beyond the matlab ode suite. *Computers and Mathematics with Applications*. 40 (2000) 491-512.

[3] K.V. Beard and C. Chuang. A new model for the equilibrium shape of raindrops. *J. Atmos. Sci.* 44, 1509-1524, 1987.

[4] K.V. Beard, V.N. Bringi, M. Thurai. A new understanding of raindrop shape. *Atmospheric Research*. 97(4), 396-415, 2010.

[5] I. Bucher. Circle fit: http://www.mathworks.com/matlabcentral/fileexchange/5557-circle-fit/content/circfit.m.

[6] J. Chen, K. Yang and Y. Yuan. Sph-based visual simulation of fluid. *International Converence on Computer Science & Education*. 2009.

[7] J. Evers, S. Hille and A. Muntean. Solutions to a measured-valued mass evolution problem with flux boundary conditions inspired by crowd dynamics. *arXiv:1210.4118*. October 2012.

[8] P. Gao and J.J. Feng. Spreading and breakup of a compound drop on a partially wetting substrate. *Journal of Fluid Mechanics*. 682, 415-433, 2011.

[9] D.C. Giancoli. *Physics - Principles with Applications*. Pearson Education International, 2005. Sixth edition.

[10] V. Grubelnik and M. Marhl. Drop formation in a falling stream of liquid. *American Association of Physics Teachers*. 73, 415, (2005).

[11] H. Haber. Figure 2: http://scipp.ucsc.edu/ haber/ph5B/bubble.pdf.

[12] Q. Hou. Simulating unsteady conduit flows with smoothed particle hydrodynamics. *Eindhoven University of Technology, PhD Thesis*, 2012.

[13] J.H. Jeong, M.S. Jhon, J.S. Halow and J.van Osdol. Smoothed particle hydrodynamics: Applications to heat conduction. *Computer Physics Communications*. 153, 71-84, 2003.

[14] K. Kendig. *Conics*. The Mathematical Association of America, 2005.

[15] A. Klaf. *Calculus Refresher*. Dover, 1956. ISBN 978-0-486-20370-6, p. 151-168.

[16] M. Kline. *Calculus: An Intuitive and Physical Approach*. Dover, 1998. ISBN 978-0-486-40453-0, p. 457-461.

[17] J.D. Lambert. *Numerical Methods for Ordinary Differential Systems: The Initial Value Problem*. Chichester : Wiley, 1991.

[18] B. Lautrup. *Physics of Continuous Matter: Exotic and everyday Phenomena in the Macroscopic World*. Taylor & Francis Group, 2004. Chapter "Surface Tension".

[19] J.E. Lavery. Shape-preserving, multiscale interpolation by univariate curvature-based cubic l1 splines in cartesian and polar coordinates. *Computer Aided Geometric Design*. 19, 257-273, 2002.

[20] P. Lenard. Uber regen. *Meteor.Z.* 21,248-262, (1904) [for English translation sec: Quart J. Roy. Meteor. Soc., 31, 31, 62-73 (1905)].

[21] B. Lim. Derivation of the shape of raindrops. *School of Applied and Engineering Physics, Cornell University*. Ithaca, NY 14853, 2006.

[22] G.R. Liu and M.B. Liu. Smoothed particle hydrodynamics : A meshfree particle method. *World Scientific*. Singapore, 2003.

[23] M.B. Liu and G.R. Liu. Smoothed particle hydrodynamics (sph): An overview and recent developments. *Arch. Comput. Methods. End.* 17, pp.25-76, 2010.

[24] Meng. Figure: http://www.treknature.com/gallery/photo154910.htm.

[25] J.J. Monaghan. Smoothed particle hydrodynamics. *Institute of Physics Publishing*. Rep.Prog.Phys.68 ,1703-1759, 2005.

[26] J.J. Monaghan. Smoothed particle hydrodynamics. *Annual Review of Astronomy and Astrophysics*, 1992. 30(1),543-574.

[27] O.I.del Rio and A.W. Newmann. Axisymmetric drop shape analysis: Computational methods for the measurement of interfacial properties from the shape and dimensions of pendant and sessile drops.

[28] Y. Saad. *Iterative Methods for Sparse Linear Systems*. London : PWS Publishing, 1996.

[29] J.H. Spurk and N. Aksel. *Fluid Mechanics*. Springer, 2008.

[30] V. Sátek. Stiff systems analysis. *Information Sciences and Technologies Bulletin of the ACM Slovakia*. Vol. 4, No. 3 (2012) 1-11.

[31] J. Stoer and R. Bulirsch. *Introduction to Numerical Analysis*. Berlin : Springer, 1993. p. 502-507.

[32] A. Tartakovsky and P. Meakin. Modeling of surface tension and contact angles with smoothed particle hydrodynamics. *Physical Review*. E 72, 026301, 2005.

[33] N.B. Vargaftik, B.N. Volkov and L.D. Voljak. International tables of the surface tension of water. *Journal of Physical and Chemical Reference Data*. Volume 12, Issue 3, pp.817-820, July 1983.

[34] I. Zisis and B.J. Linden. Shock loading of layered materials with sph. *8th SPHERIC Proceedings*. 4-6 June 2013, Trondheim - Norway.

[35] I. Zisis, B.J.Linden and C.Giannopapa. Towards a smootherd particle hydrodynamics algorithm for shocks through layered materials. *PVP2013-97345*. July 14-18, 2013, Paris, France.